NAVAL POSTGRADUATE SCHOOL
Monterey, California

"Original contains color plates: All DTIC reproductions will be in black and white"

THESIS

TEMPORAL AND SPATIAL DECORRELATION SCALES OF THE YELLOW SEA THERMAL FIELDS

by

Susan K. Wells

September 1994

Thesis Advisor: Peter C. Chu
Co-Advisor: Steve D. Haeger

Approved for public release; distribution is unlimited.

DISCLAIMER NOTICE

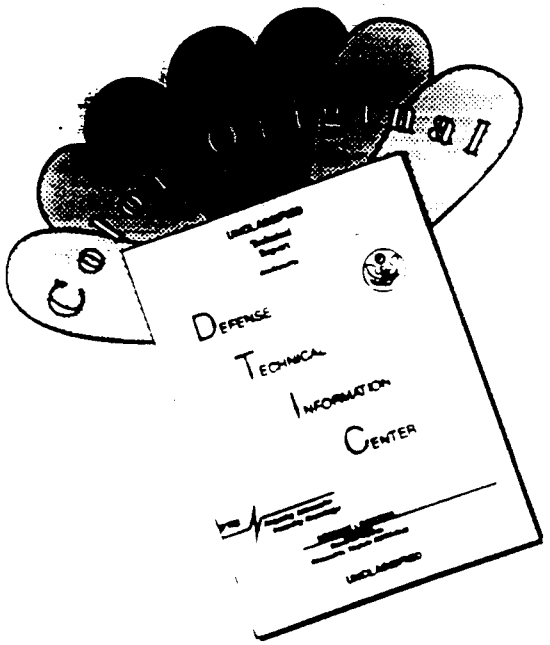

THIS DOCUMENT IS BEST QUALITY AVAILABLE. THE COPY FURNISHED TO DTIC CONTAINED A SIGNIFICANT NUMBER OF COLOR PAGES WHICH DO NOT REPRODUCE LEGIBLY ON BLACK AND WHITE MICROFICHE.

REPORT DOCUMENTATION PAGE

Form Approved OMB No. 0704-0188

1. AGENCY USE ONLY *(Leave blank)*	2. REPORT DATE September 94	3. REPORT TYPE AND DATES COVERED Master's Thesis

4. TITLE AND SUBTITLE TEMPORAL AND SPATIAL DECORRELATION SCALES OF THE YELLOW SEA THERMAL FIELDS (U)

5. FUNDING NUMBERS

6. AUTHOR(S) Wells, Susan, K.

7. PERFORMING ORGANIZATION NAME(S) AND ADDRESS(ES)
Naval Postgraduate School
Monterey CA 93943-5000

8. PERFORMING ORGANIZATION REPORT NUMBER

9. SPONSORING/MONITORING AGENCY NAME(S) AND ADDRESS(ES)
U.S. Naval Oceanographic Office
Stennis Space Center, MS 39522

10. SPONSORING/MONITORING AGENCY REPORT NUMBER

11. SUPPLEMENTARY NOTES The views expressed in this thesis are those of the author and do not reflect the official policy or position of the Department of Defense or the U.S. Government.

12a. DISTRIBUTION/AVAILABILITY STATEMENT
Approved for public release; distribution is unlimited.

12b. DISTRIBUTION CODE

13. ABSTRACT *(maximum 200 words)* Historically, studies on decorrelation scales have been conducted in the deep ocean waters. As the Navy shifts its interest toward the less understood shallow water regions, decorrelation scales need to be computed in order to use formerly deep water models such as the Optimum Thermal Interpolation System (OTIS) for shallow water regions such as the Yellow Sea.

A data set containing over 35,000 temperature profiles from 1929 to 1991 was obtained from the Naval Oceanographic Office's MOODS data set. The winter and summer seasons provide realistic results. Winter has the smallest decorrelation scales of all the seasons, approximately 15 days and 165 km. Summer shows that there are different decorrelation scales between the surface and at depth. The surface has scales of 12.3 days and 251 km while at depth the scales are approximately 16.5 days and 163 km. An observational sampling network design is suggested for future sampling of the region. Spring and fall provide mixed results which may be due to the irregularities in time and space of the data set or to the

Approved for public release; distribution is unlimited.

TEMPORAL AND SPATIAL DECORRELATION SCALES OF THE YELLOW SEA THERMAL FIELD

by

Susan K. Wells
Lieutenant United States Navy
B.S., United States Naval Academy, 1985

Submitted in partial fulfillment
of the requirements for the degree of

MASTER OF SCIENCE IN METEOROLOGY AND PHYSICAL OCEANOGRAPHY

from the

NAVAL POSTGRADUATE SCHOOL
September 1994

Author: _____
Susan K.Wells

Approved by: _____
Peter C. Chu, Thesis Advisor

_____
Steven D. Haeger, Co-Advisor

_____
Robert H. Bourke, Chairman
Department of Oceanography

ABSTRACT

Historically, studies on decorrelation scales have been conducted in the deep ocean waters. As the Navy shifts its interest toward the less understood shallow water regions, decorrelation scales need to be computed in order to use formerly deep water models such as the Optimum Thermal Interpolation System (OTIS) for shallow water regions such as the Yellow Sea.

A data set containing over 35,000 temperature profiles from 1929 to 1991 was obtained from the Naval Oceanographic Office's MOODS data set. The winter

TABLE OF CONTENTS

LIST OF FIGURES

ACKNOWLEDGEMENTS

The author would like to acknowledge the financial support of the Naval Oceanographic Office and the time and efforts of Steve Haeger, Carl Szczechowski, and Dr. Mike Carron. Mr. Haeger provided guidance, programs and help in shaping this study. Mr. Szczechowski provide two programs that this study was based on and answered many questions.

Many thanks to Dr. Peter Chu for his guidance, extreme patience, and unending good nature. He made the work bearable and was always encouraging. Laura Ehret imparted her computer knowledge on a hands on basis. Chuck Fralick and John Steger for programing help and thinking of new graphs.

A special thanks to my parents and two good friends. Bruce Allen for always being there when I needed him and David Herscovici for listening.

I. INTRODUCTION

Various ocean systems such as fronts, eddies and water masses have different temporal and spatial correlation scales (Figure 1.1). These scales feature a system's life span and spatial extent both horizontally and vertically. Horizontal scales are often divided into north-south and east-west length scales and are represented by a variety of parameters. For example, Provost and Le Traon (1993) attempted to describe the Brazil-Malvinas Current confluence confines through temporal and spatial scales using variable altimetric measurements.

Horizontal scales for temperature fields in the deep ocean basins have been extensively studied. Each ocean has its own general scales with variations in specific regions. White et al. (1982) identified spatial correlation scales in the western Pacific of about 600 km in the tropics (south of 17.5°N) and 300 km in the subtropics (north of 17.5°N) while Özsoy et al. (1989) found the spatial scale to be 200-250 km in the Levantine Basin of the Mediterranean Sea. Historically, most of the studies on correlation scales have been conducted in deep ocean waters; few have been conducted on the continental shelf. There are several reasons for this occurrence with the main one being that deep water physics are better understood. Another, yet not an obvious reason, is that in past years the US Navy has put its emphasis on deep water operations. Therefore, most of the Navy's research and modeling assets have been directed toward deep water applications. This poses many challenging problems as the Navy shifts its interests toward the less understood shallow waters regions. Naval models such as the Optimum Thermal Interpolation System (OTIS) that have been designed for deep water usage need to be modified for shallow water use.

Deep ocean temperature profiles tend to follow the pattern of a mixed layer,

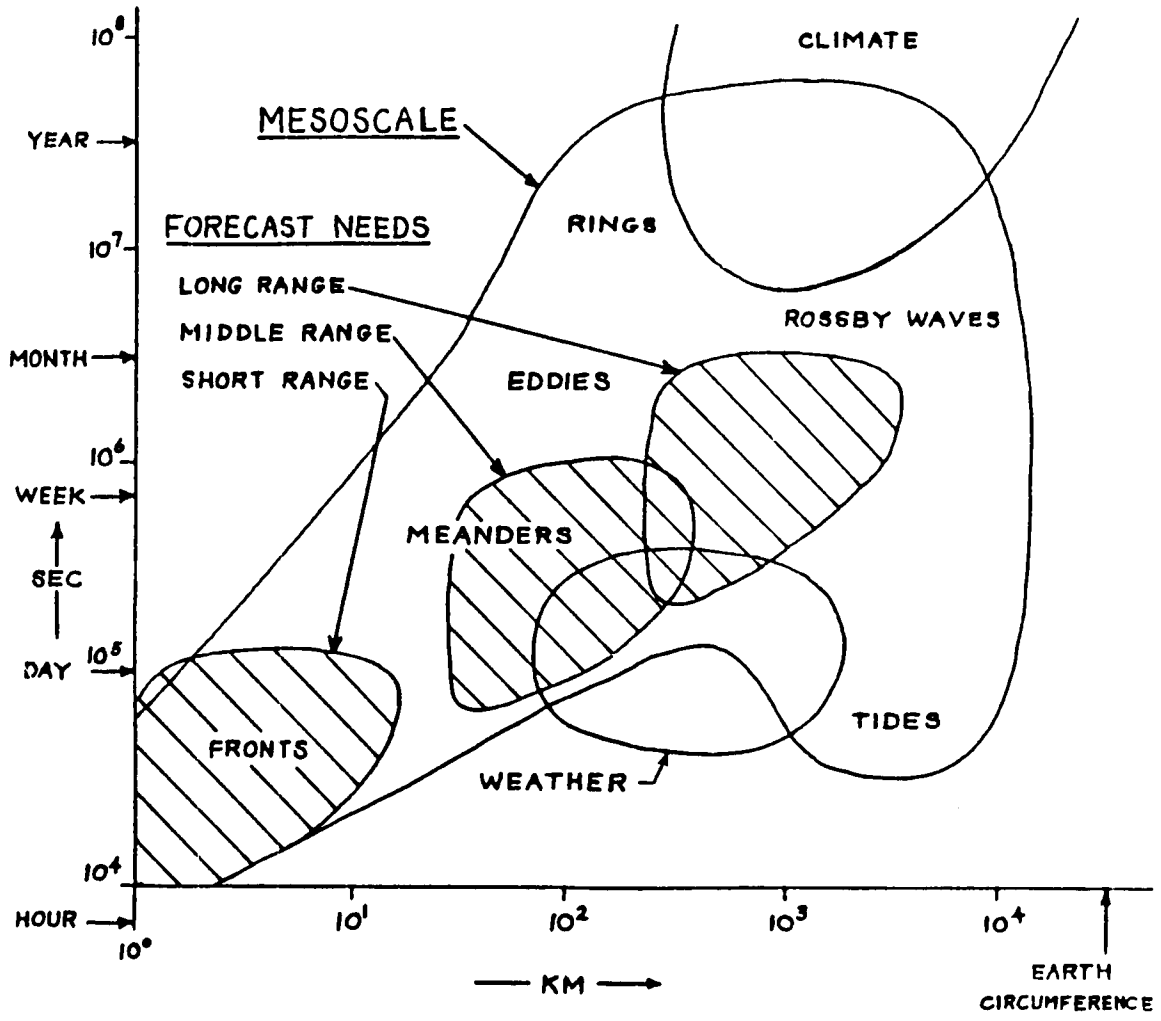

Figure 1.1 Approximate Ranges of Horizontal and Temporal Scales of Selected Ocean Variabilities (from Mooers and Robinson, 1981).

Shallow water does not consistently mimic this pattern. It may range from the classical profile or be completely isothermal. The shallow environment influences the temperature distribution with some parameters like bathymetry, river run-off and tides often omitted in deep water becoming increasingly important in shallow

variations of the autocorrelation function which is fitted by the Gaussian function used in the OTIS model. Finally, the temporal and spatial correlation scales are obtained.

To investigate the vertical variation of the horizontal and temporal scales several schemes have been used in deep water analysis. Sprintall and Meyer (1991) used the sea surface temperate (SST) and the depth of the 20°C isotherm for the Eastern Pacific and White et al. (1982) used 100, 200, and 300 m depths for the Northwestern Pacific. Neither scheme is practical for the Yellow Sea region since the 20°C isotherm is not always present and the water depth is less than 150 m throughout. Since shallow water is strongly influenced by bathymetry, it was decided that the seasonal correlations scales for the temperature fields should be computed for the surface and depths representing 50% and 80% of the water column.

II. REGIONAL CHARACTERISTICS

A. GENERAL

The Yellow Sea is the middle section of a continental sea system (Figure 2.1). To the north is the Bohai Sea and to the south the East China Sea and the Western Pacific beyond. It lies between mainland China and the Korean peninsula and covers an area of approximately 404,000 km^2. There are four major rivers that flow into it. The Yangtse River located to the southwest, the Yellow and Liao Rivers to the north and the Han River to the east.

The Yellow Sea is considered a shallow basin sea. The bottom slopes from 20 m in the north to its southern boundary, the shelf break, at 150 m. The Bohai Sea region ranges in depth of 20 to 50 m. A trough oriented north to northwest and paralleling the Korean coastline occupies the center of the sea. It has a maximum depth of 90 m. Within 50 km of the coastline the average water depth is 20 m. Moving toward the shelf break the depth slowly increases. The shelf break runs in a roughly northeast-southwest orientation and quickly drops from 150 to 500 m in a few kilometers. For the remainder of this study the Yellow Sea will include the Bohai Sea and that portion of the East China Sea that lies on the continental shelf unless specifically stated.

B. METEROLOGY

Nester (1977) compiled an extensive report that is the foundation of this meteorological overview with wind speeds supplemented by the US Navy Regional Climatic Study (Elms, 1989). The Yellow Sea lies within the Asian monsoon circulation pattern and experiences hot, short, humid summers and long, cold, dry winters. Winter is dominated by an intense cold high pressure system called the Siberian high. Its greatest intensity occurs in January, pushing cold, dry air from the

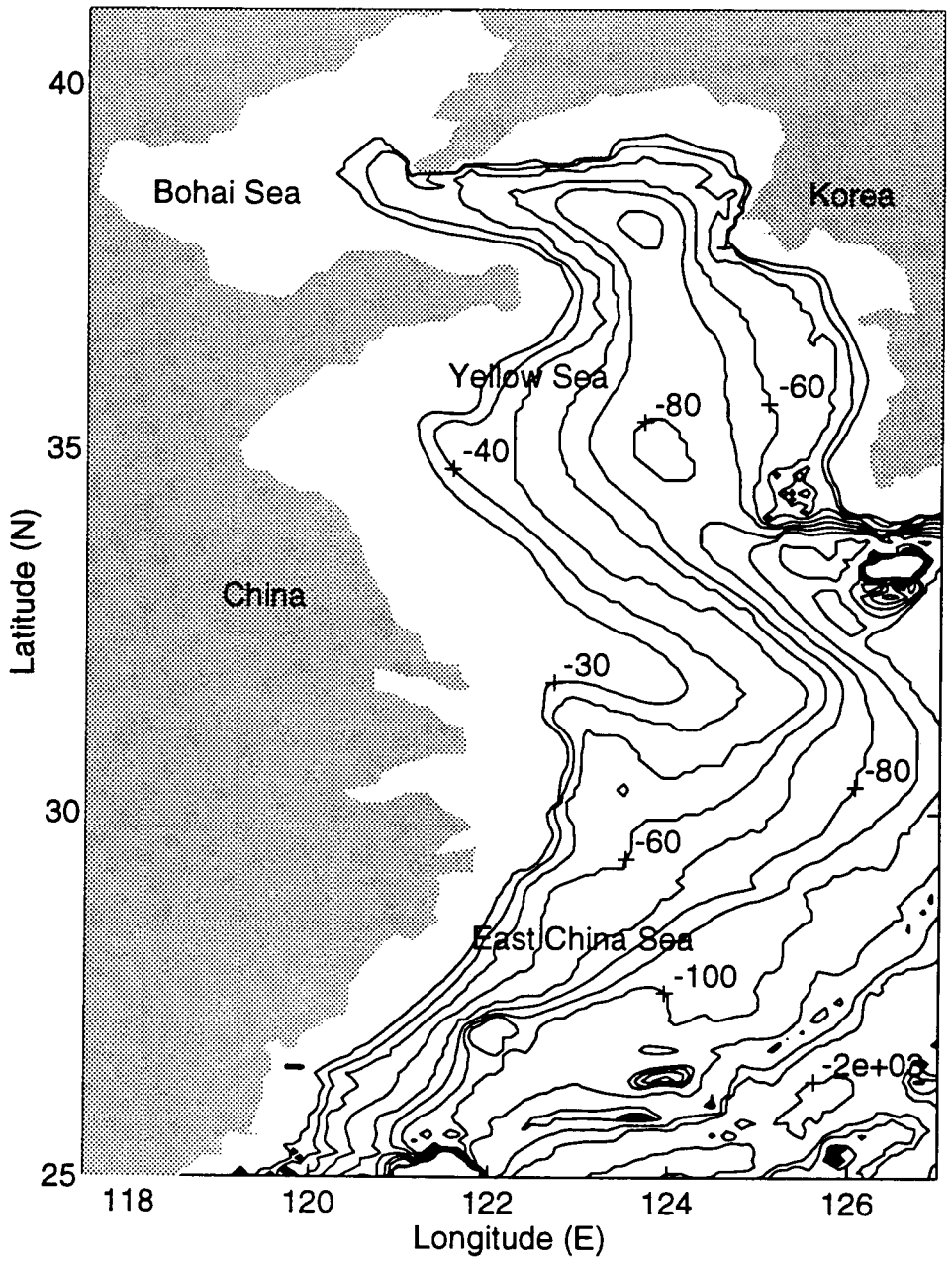

Figure 2.1 Bathymetry of the Bohai, Yellow and East China Seas. Depths are in 10 m Increments. Bathymetry Data are from the NGDC and NAVOCEANO World Wide DBD5 Bathymetry Data Bases.

interior of the continent along the east coast of the Asian mainland. The clockwise circulation of the Siberian high produces northerly or northwesterly winds referred to as the northwest monsoon. This is the predominant feature of the winter weather even though small low pressure areas known as Shanghai lows form over the Yellow Sea and travel over the Korean peninsula. Figure 2.2 shows the mean pressure and wind systems for February. Surface winds are normally from the north-northwest with an average speed of 8 m/s.

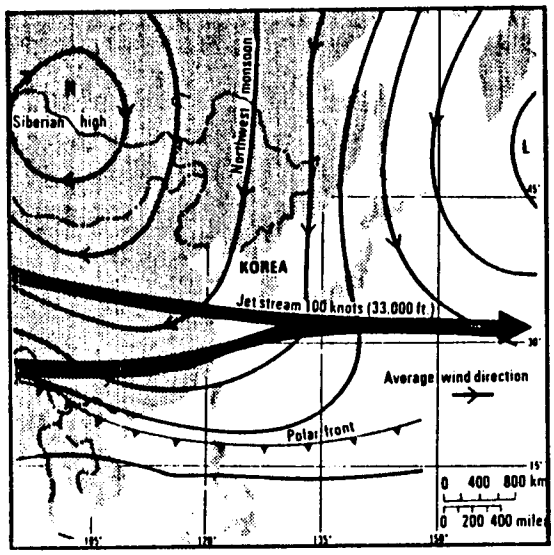

Figure 2.2 February Mean Pressure and Surface Wind Pattern During the Winter Monsoon (from Langill, 1976).

March marks the beginning of the transition from winter to spring. The weakening of the Siberian high permits the northerly migration of the polar front. Tropical maritime air begins to push northward displacing the cold, heavy Siberian air causing "migratory highs" that may in turn be displaced by low pressure areas from the south. Northerly winds are no longer dominant and by the end of the season winds are from the south averaging 4.6 m/s.

Summer begins in June and is also referred to as the southwest monsoon season. The polar front has migrated to its farthest northern extent. It is a boundary

zone between continental air masses from Asia and the warm moist air from the tropical oceans and serves as a buffer zone between the two air masses. Figure 2.3 shows the mean pressure and wind systems for the onset of summer. As summer

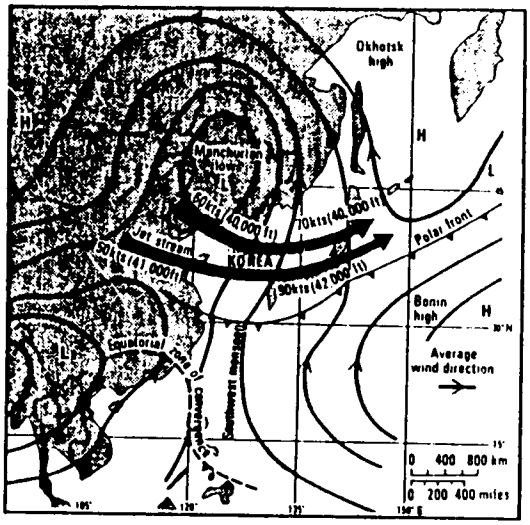

Figure 2.3 June Mean Pressure and Surface Wind Pattern During the Summer Monsoon (from Langill, 1976).

progresses, the Bonin high pressure cell expands westward into the East China Sea while the Manchurian low, caused by land mass heating, settles over northern China, just north of the Yellow Sea. This is the season of predominantly southward winds and heavy rains. Although the three months of summer are ripe for typhoons, the end of July and the beginning of September is the period of their greatest probability. The East China and central Yellow Seas have a 74% and 32% chance, respectively, of a tropical cyclone occurring in the region (Elms, 1989). The polar front is unstable and is conducive to heavy rainfall. The season starts with prevailing winds from the south at 5.1 m/s but shift to the north-northeast by September.

September marks the fall transition season with a rapid southward movement of the polar front accompanied by a wide band of rain. By the end of the month the

southerly warm, moist, tropical air of the summer monsoon has been replaced by a cooler, drier air from the continent. The Siberian high begins to form as the Asian

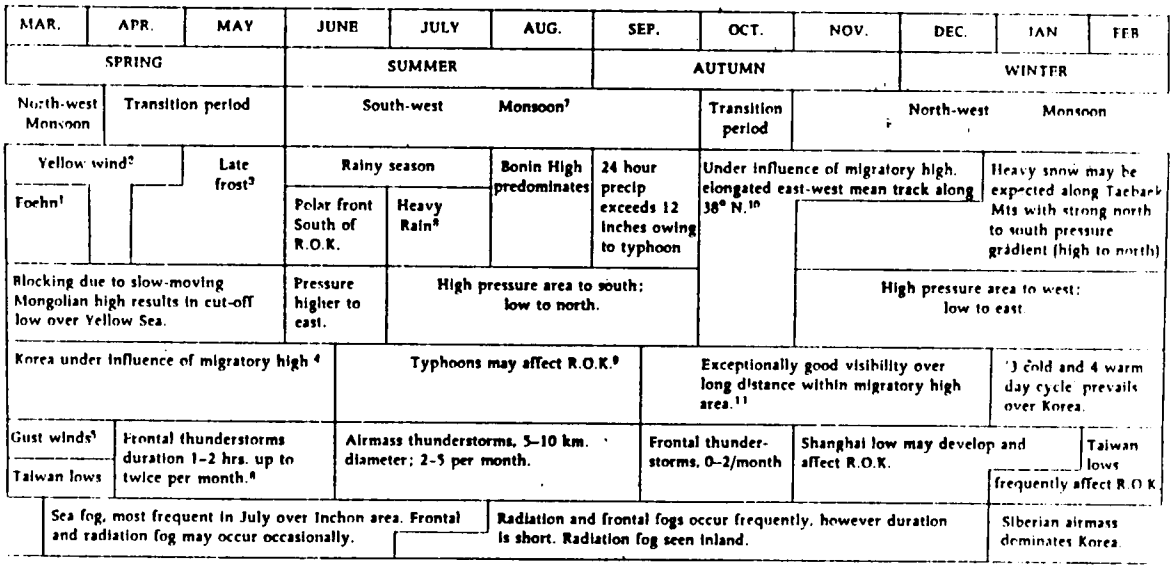

[1] North China low passing over North Korea causes foehn (hot, dry south to easterly flow) over west and central sectors of R.O.K.
[2] Mongolian low passing over southern Manchuria causes yellow winds (strong, dry west wind carrying yellow dust).
[3] Late frost may occur when migratory high predominates over R.O.K.
[4] Mean track of migratory high is along 33° N.
[5] Low over Shantung Peninsula may cause gusty winds over R.O.K.
[6] Intense frontal thunderstorms in May signal approach of rainy season.
[7] Cool summer and drought if South-west Monsoon weak and Okhotsk High intense.
[8] Heavy rain.latter part of rainy season.
[9] Hot and humid with maritime tropical air intrusion. None or as many as two tropical storms or typhoons from end of June through September may affect R.O.K.; least likely in August owing to Bonin High.
[10] Migratory highs move at about 20 knots, speed up with northward movement and vice versa.
[11] Often precedes bad weather.

Table 2.1: Climatic Calendar for South Korea (from Langill, 1976).

By the time July arrives the Yellow Sea Current has developed into a closed cyclonic circulation (Figure 2.4b) which causes an upwelling effect in the central

(a) (b)

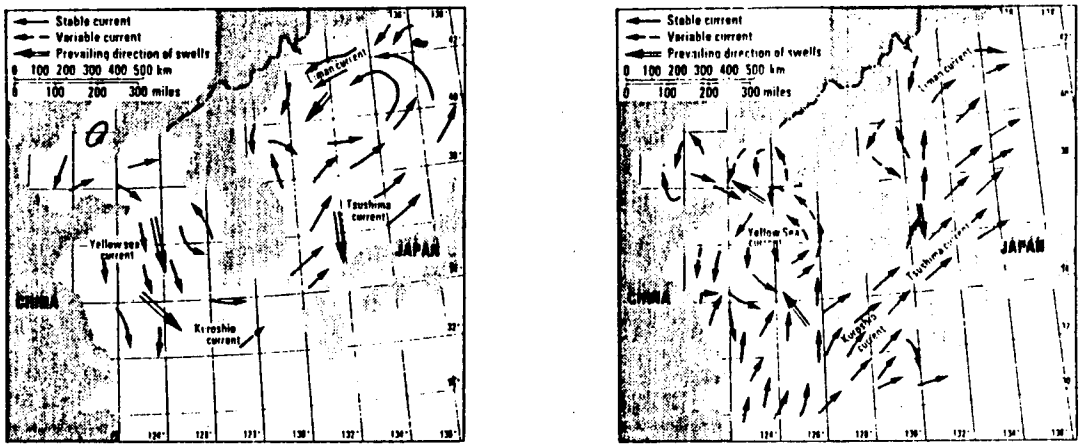

Figure 2.4 Representation of Surface Currents Off the Korean Peninsula in (a) Winter and (b) Summer (from Bartz, 1972).

region. This circulation occurs above the thermocline, which is about 13 m in August, and may reach a speed of 15.5 cm/s. Below this circulation is a cold water mass, commonly referred to as the 'Cold Water Mass of the Yellow Sea' (CWYS), that remains unchanged and motionless throughout the summer (Li and Yuan, 1992). The SST is nearly uniform throughout with an average temperature of 23°C. The MLD is at its shallowest and maybe negligible in the coastal and the Bohai Sea regions due to surface heating. The water is strongly stratified.

October is the beginning of the transition back to winter conditions. The southerly winds have weakened letting the sea surface slope reestablish itself again. The Yellow Sea warm current becomes weak and variable. The SST steadily decreases 20°C from the beginning of the season to the end. The MLD begins to

deepen as stronger winds and convective mixing occur, yet the water mass is still stratified.

Liu et al. (1992) presents a loose interpretation of the temporal and spatial distribution of water masses through temperature and salinity analyses. The Yellow Sea consists of five main water masses: the coastal water, the Yellow Sea surface water, the Bohai-Yellow Sea mixed water, the Yellow Sea bottom cold water and the Kuroshio water. The coastal water is influenced by the amount of river runoff. In the spring and summer, when run-off is the greatest, low salinities (28.4-30.5) and high temperatures (27.5°C) identify this water with the reverse true in the fall and winter. The Yellow Sea surface water encompasses the middle of the sea. It is the dominant water mass in the summer due to the intense surface heating. During the fall and winter months the water cools and becomes one water mass with the bottom water. The Bohai-Yellow Sea mixed water is in the northern region where the two seas connect. This water mass is a mixture of the coastal waters and the Yellow Sea surface water. Its greatest extent is in fall and winter when it reaches the Korean Peninsula. By summer the Yellow Sea surface water has penetrated into the Bohai Sea. The Yellow Sea bottom cold water or the CWYS is present in the spring and summer. Its mean temperature is 5 to 12°C and the mean salinity 31.8-33.8. As stated earlier, with the approach of winter the CWYS merges with the surface to form one water mass named the Yellow Sea surface water. The Kuroshio water is located along the shelf break and is characterized as high salinity and high temperature. The mean temperature is 18-29°C and the mean salinity is 34.2-34.9.

III. OPTIMUM THERMAL INTERPOLATION SYSTEM

The US Navy requires and conducts daily analyses of the ocean thermal structure for a wide variety of tasks. These analyses are made for both global and regional areas, with resolutions as small as 20 km in some regions. The Navy's Optimum Thermal Interpolation System (OTIS) combines real-time data, climatology and predictions from ocean mixed-layer models to represent an accurate picture of the ocean thermal structure on global and regional scales (Phoebus,1988; Clancy et al., 1989). OTIS can be executed in either "shallow" or "deep" analysis modes. This statement is somewhat deceptive since the term shallow in this case refers to a depth of 400 m. The analysis sequence for OTIS is the calculation of (1) SST, (2) the mixed layer depth, and the (3) temperature below the mixed layer depth. In truly shallow waters such as the Yellow Sea this analysis sequence may be inappropriate since isothermal profiles are possible.

OTIS is designed to receive its climatological data from the Generalized Digital Environmental Model (GDEM) which synthesizes a climatology from a given data base. Adequate climatologies for the world's marginal seas are not prevalent but are being rapidly developed by the Naval Oceanographic Office. Even though OTIS is not a shallow model in the literal sense, it is hoped that with the proper parameters OTIS can be modified for use in marginal seas.

OTIS is based on the Optimum Interpolation (OI) data assimilation technique of Gandin (1965). OI combines a climatological temperature at a gridpoint plus a weighted combination of observed and model predicted anomalies. Thus the analyzed SST at the k th gridpoint is

$$T_k = T_k^c + \sum_{i=1}^{N} \alpha_{ki} (T_i^o - T_i^c) + \beta_k (T_k^p - T_k^c) \qquad (3.1)$$

where T_k^c is the climatological surface temperature at the gridpoint, T_k^p the predicted temperature at the gridpoint produced by a 24-hour forecast, T_i^o the observed temperature at location i, T_i^c the climatological temperature at location i valid at the time of observation i, α_{ki} the weight applied to the observational correction, β_k the weight applied to the prediction correction, and N the number of observations. With the minimal mean square error, these weights satisfy the following equation:

$$\eta_{ki} = \sum_{j=1}^{N} (\eta_{ij} + \delta_{ij}\lambda_i^o)\,\alpha_{kj} + (\eta_{ik} + \delta_{ik}\lambda_k^p)\,\beta_k \qquad (3.2)$$

where η_{ij} is the space-time autocorrelation function between climatological anomalies at location i and location j, λ_i^o is the noise-to-signal ratio for the observation, λ_k^p is the noise-to-signal ratio for the prediction and δ_{ij} is the Kronecker delta function. The autocorrelation function is represented as

$$\eta_{ij} = exp\,(-A^2{}_k\Delta x^2{}_{ij} - B^2{}_k\Delta y^2{}_{ij} - C^2{}_k\Delta t^2{}_{ij}) \qquad (3.3)$$

where Δx_{ij}, Δy_{ij} and Δt_{ij} are the east-west, north-south and time separations between locations. The quantities A_k, B_k and C_k are the inverses of the east-west, north-south and time decorrelation scales at different depth levels, k. These parameters are user-specified within OTIS and must reflect the oceans's resolvable variability about climatology. The better the correlation scales are calculated, the higher the accuracy the thermal field will be. In order to implement OTIS to the Yellow Sea region decorrelation scales, A_k^{-1}, B_k^{-1} and C_k^{-1}, must be determined.

IV. METHODS OF ANALYSIS

A. MASTER OCEANOGRAPHIC OBSERVATION DATA SET (MOODS) OF THE YELLOW SEA

1. General

The oceanographic data used for this study were taken from the Master Oceanographic Observation Data Set (MOODS), the U.S. Navy's environmental data base. It is a collection of observed vertical profiles of temperature, salinity and computed vertical profiles of sound speed. MOODS consists of over five million world-wide profiles of oceanographic data and is considered to be the most comprehensive collection of temperature and salinity data known to exist. The data base has been compiled from military, academic and commercial sources, both foreign and domestic. It has a classified and unclassified version. The data were derived from various instrumentation types ranging from the Nansen bottles of the 1920's to the present day Conductivity-Temperature-Depth (CTD) recorder. The MOODS data are not in a gridded form; they are irregularly distributed in space and time.

The original MOODS data base used for this study consisted of approximately 50,000 temperature profiles located between 117-128 °E longitude and 25-41°N latitude (Figure 4.1a) which encompasses the Yellow Sea and the northern East China Sea. The data spans the period from 1929 to 1991. The data were screened to restrict observations only to those temperature profiles that were located on the continental shelf. This reduced the data set to 35,658 profiles (Figure 4.1b). Since horizontal scales have seasonal variations, the data base was binned into four seasons. The seasons were defined according to the convention of the Naval Oceanographic Office for the Yellow Sea (Haeger, personal communication) January, February and March constituted winter; April, May and June, spring; July,

August and September, summer; October, November and December fall. Table 4.1 shows the partition of the data; winter has the least profiles and summer the most.

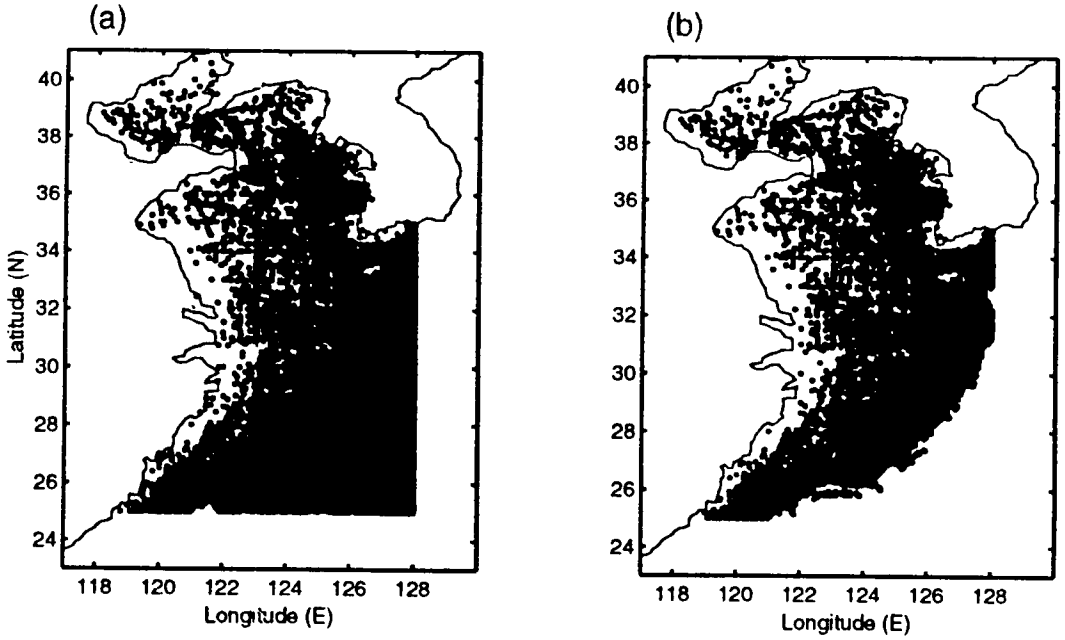

Figure 4.1 (a) Distribution of Entire MOODS Temperature Profile Data Set, (b) Profile Distribution After Removal of Data Deeper than Restricted to the Shelf Break.

Season	Number of Profiles
Winter	7391
Spring	9868
Summer	9915
Fall	8484

TABLE 4.1: Number of Temperature Profiles in the Data Base for Each Season.

The number of temperature profiles from year to year fluctuates greatly. The period of 1963 to 1977 is found to have the greatest concentration of profiles averaging 315 per season.

2. Limitations

The main limitation of the MOODS data is its irregular distribution in time and space. Certain areas and events are over sampled while other areas lack enough observations to gain any meaningful insight. Vertical resolution and data quality are also highly variable depending much on instrument type and sampler expertise.

The sparsity of profiles have a direct impact on the type of analysis conducted on the data. A prime example of this is the Bohai Sea region in winter. Access for data gathering in this region has been limited. In fact, most observations in the area have been conducted prior to the 1960's. Figure 4.2a depicts unclassified observation locations for the winter seasons of 1963 to 1977. Another data poor area is the eastern coastline of mainland China (Figure 4.2b). The spring of 1969 had the greatest number of profiles for a given season yet the entire Chinese coastline lacks a single recorded hydrographic cast. An analysis of location plots from 1963 to 1977 (Appendix A) shows this same general lack of data for these two regions. Statistical relevance must be considered when trying to calculate spatial scales with such sparsely located observations.

Temporally uneven distributions are just as great. Over all, the data base ranges from a low of one profile for 1944 to a high of 1790 profiles in 1968. The number of yearly temperature profiles in the 15 year analysis period (1929 to 1991) is ranges from 592 to 925. When further subdivided into seasons, this greatly reduces the pool of temperature profiles for which statistical analysis may be conducted. Figure 4.3 and Appendix B provide examples of the temporal irregularities and sparseness of the observations. There are frequent 15 to 20 day gaps of ten observations or less per day. For an area as large as the Yellow Sea this does not provide an adequate data base to establish the inherent variability on a yearly basis.

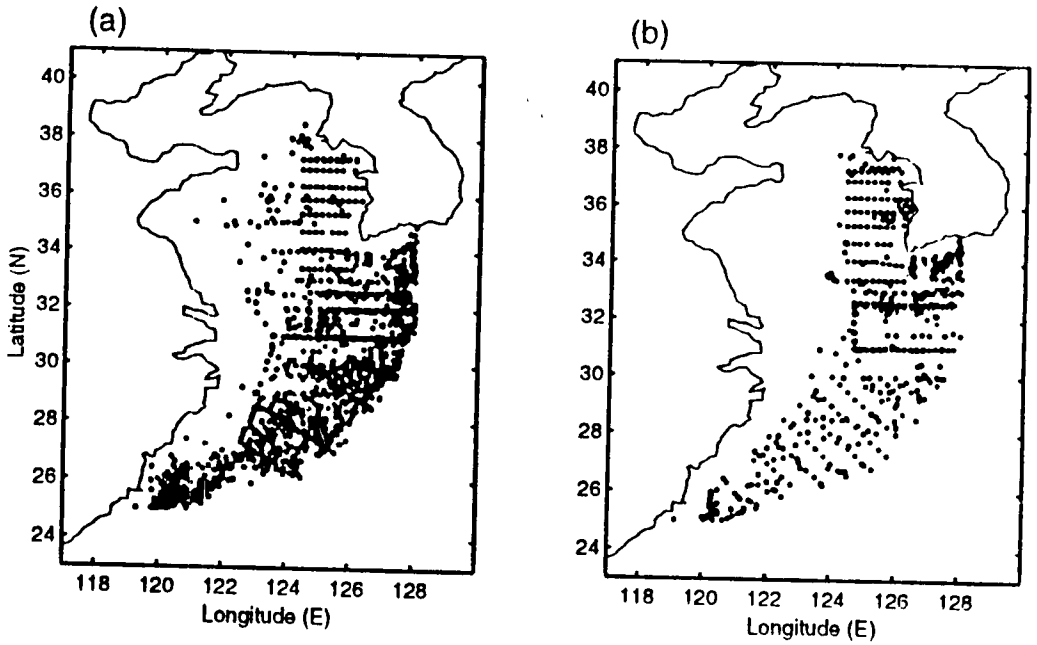

Figure 4.2 (a) Winter Temperature Profile Locations from MOODS Data Base From 1963 to 1977, (b) Locations of Temperature Profiles During Spring 1969, a Period Illustrating Maximum Data Density in a Given Year.

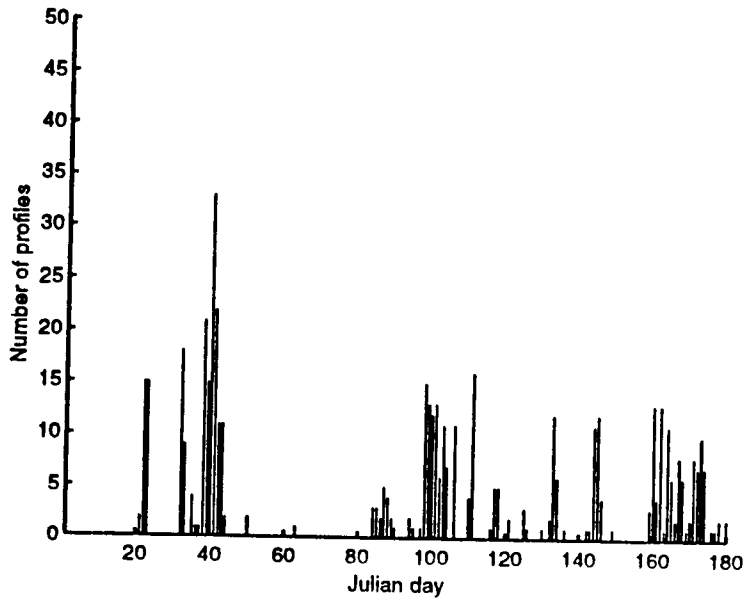

Figure 4.3 Number of Temperature Observations During Winter and Spring 1977, Illustrative of Typical Data Density in Any Given Half Year.

Spatial and temporal irregularities along with the shear lack of data must be carefully weighed in order to avoid statistically-induced variability. Originally, it was hoped that there would be sufficient data to compute horizontal autocorrelation

deep water climatologies several submodels are constructed in the vertical (Figure 4.4a). These submodels extend temperature profiles that do not extend to the sea floor (or to a given depth level) by interpolating values from profiles that do extend each submodel level.

In shallow waters having sloping bottoms, if vertical submodels are used (Figure 4.4b), some areas (hashed area) are not covered by any submodels and therefore no climatology can be constructed for the area (Haeger, 1991). In order to compensate for this problem a vertical interpolating scheme that produces horizontal sloping surfaces was used (Figure 4.5). Horizontal temperature climatologies were constructed for the surface, 50% and 80% depth of the water column. Mid-water properties were expected to be modeled by the 50% depth whereas, the 80% depth was chosen since it was near the bottom but provided enough height for small scale depth variations. The surface temperatures in this case were actually any observations from the surface to 2 m below.

After the temperature profiles were interpolated for the specified depths the temperature values were then horizontally gridded using the Minimum Curvature Spline Interpolator (MISP) algorithm. The MISP can be broken into three stages: partial grid computation, regional grid computation and final computation. The partial grid computation consists of binning the input data into bins equal to the specified output grid size. All data falling within a distance of half a grid cell of a grid point (i, j) were averaged to form an averaged $\bar{x}_{ij}, \bar{y}_{ij}$(location) and $\bar{T}_{ij}$ (temperature) set associated with that grid cell. At this stage $\bar{T}_{ij}$ is not situated at the gridpoint (i, j) but is located at the position $(\bar{x}_{ij}, \bar{y}_{ij})$. After all data have been read, a 'partial grid' has been formed and consists of grid points with and without associated $(\bar{T}_{ij}, \bar{x}_{ij}, \bar{y}_{ij})$ values.

The second stage of the gridding process consists of computing a regional grid. The $(\bar{T}_{ij}, \bar{x}_{ij}, \bar{y}_{ij})$ sets obtained for a grid cell in the first stage are used as input.

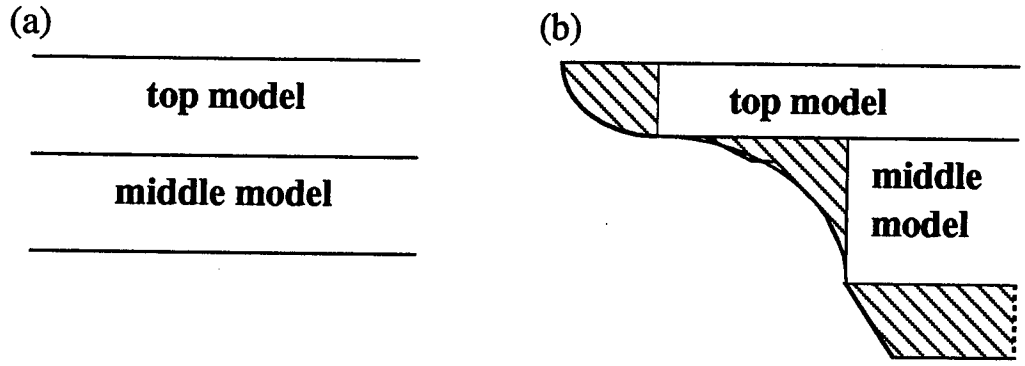

Figure 4.4 The Geometries of Vertical Submodel in the Construction of Climatology Temperature Profiles in the (a) Deep Water and (b) Continental Shelf.

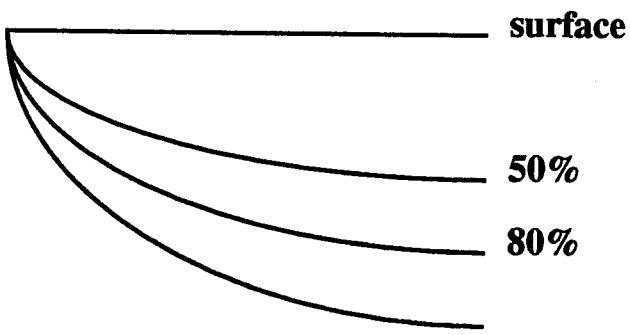

Figure 4.5 Depiction of the Depth Levels that Horizontal Temperature Climatologies were Constructed for in the Yellow Sea.

These values are first smoothed by rebinning to a grid three times the size of the original grid. A grid cell may or may not have a value at this stage. The minimum curvature spline interpolation routine was used to interpolate temperature $(\hat{T}_{ij})$ values to the gridpoints (i, j) centered at the grid cell resulting in the completion of the regional grid.

The third stage is to adjust the mean temperature ($\bar{T}_{ij}$) values of the partial grid to their respective gridpoints (i, j). First, the regional grid is interpolated back to the original grid size with a bi-cubic spline to match the partial grid. Then the gradient computed for each regional grid cell to the associated partial grid cell. The new partial grid is then merged with the regional grid. The merging consists of using the partial adjusted grid values where they exist at a gridpoint and the regional grid values where the partial grid cells are empty. This allows the input data to dominate in data rich areas and the regional data to dominate in data sparse areas (Haeger, personal communication).

Sometimes a climatology field is sensitive to the selection of the grid size. Too small a grid spacing produces false gradients appearing as bull's-eyes. Yet, if the spacing is too large, features that do exist may not appear. Grid spacings of 20 minutes and 30 minutes were analyzed in this study. As expected, the contours associated with a 30 minute grid are smoother (Figure 4.6a) than the 20 minute grid (Figure 4.6b) causing mesoscale features to be lost. In general, the 20 minute grid better depicts the findings of Elms (1989) for the Yellow Sea and hence this grid will be used for the rest of the study.

3. Yellow Sea Mean Temperature Fields

The surface temperatures for all four seasons (Appendix C) show that temperatures increase toward the south. During winter, freezing temperatures occur in the Bohai Sea region which result in surface ice. In the Yellow Sea winter temperatures are significantly higher, with readings in the high teens (14-18 °C) near the shelf break. As the year progresses towards summer, the horizontal temperature gradient decreases. Spring temperatures range from 6 °C in the Bohai Sea, 14 °C in the central Yellow Sea and 24 °C near the Kuroshio Current. By the time summer arrives the SST of the entire Yellow Sea is above 20 °C and is almost uniformly the

same. With the onset of cooler fall conditions the north-south gradient reappears. The Bohai Sea shows the presence of a pool of warm (18 °C) water while the Yellow Sea begins to establish its winter gradient with lower temperatures (14 °C) to the north and a steady increase to the shelf break (24 °C).

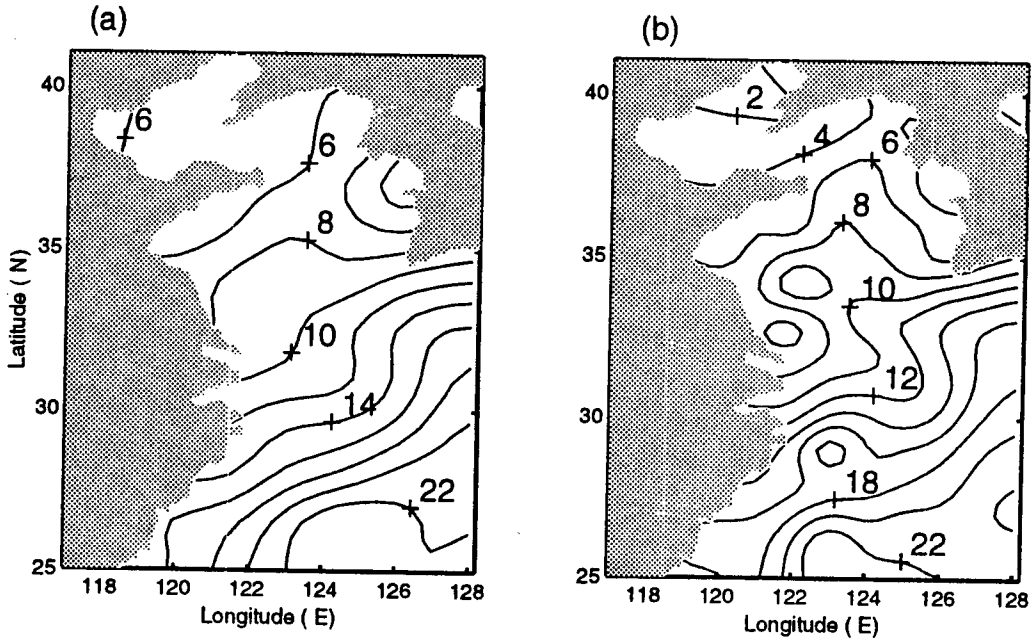

Figure 4.6 Climatological SST Field on (a) a 30 Minute Grid and (b) a 20 Minute Grid.

The horizontal temperature contours at 50% and 80% water column depths tend to mimic each other from season to season. The winter subsurface climatologies closely mirror that of the surface. The largest difference is in the shelf break area where surface temperatures are slightly higher. On the other extreme, summer shows the most contrast between surface and subsurface temperatures. The surface temperature field shows almost uniform values throughout whereas the 50% and 80% depth contours show a cold core in the middle of the Yellow Sea. Both 50%

and 80% depth levels show this cold core beginning to form in spring and dissipating in fall.

C. SPACE / TIME SORTING

At present, the spatial and temporal scales for the OTIS model are artificially prescribed as 100-250 km (Phoebus, 1988) and 20 days (Clancy et al., 1989) for the region of Japan and the South China Sea. Since synoptic temporal and horizontal scales are usually smaller than 30 days and 300 km (Mooers and Robinson, 1981), it was decided that a matrix with a maximum temporal lag of 30 days with a one day increment and the maximum spatial lag of 300 km with a 10 km increment would be used. Each matrix bin is associated with a specific temporal and spatial lag. Other matrix sizes were tested. It was found that smaller temporal and spatial lags excluded too much data while larger lags did not necessarily improve the results.

As mentioned earlier, an important feature of the Yellow Sea thermal field is the existence of the CWYS (Li and Yuan, 1992). This water mass is located in the central bottom of the Yellow Sea. In the winter it merges with the surface water but from April to November it is a distinct water mass with temperatures of 4-5°C. During the summer the overlying waters are 10-15°C warmer. The isotherms are closed curves (Figure 4.7), suggesting the basin may be treated as an isolated system (Guan, 1994). Therefore, it is reasonable to assume that the spatial autocorrelations of temperatures inside the Yellow Sea basin are isotropic, i.e.,the autocorrelations are independent of direction (N-S or E-W) and depend only on the distance between two temperature locations. This assumption of horizontal isotropicity greatly simplifies the computation.

After the matrix size was defined and the isotropic assumption made, anomaly pairs were placed within the temporal and spatial bins. To accomplish this, it is necessary to take each observation, T_o, find the closest gridpoint and compute

the anomaly, T_o', by subtracting the climatological value at this gridpoint $\overline{T_k}$ from the observation, i.e., $T_o' = T_o - \overline{T_k}$. For every individual temperature anomaly, T_o', it is paired with the other data points, $\hat{T}_o'$, within the data base. The temporal and

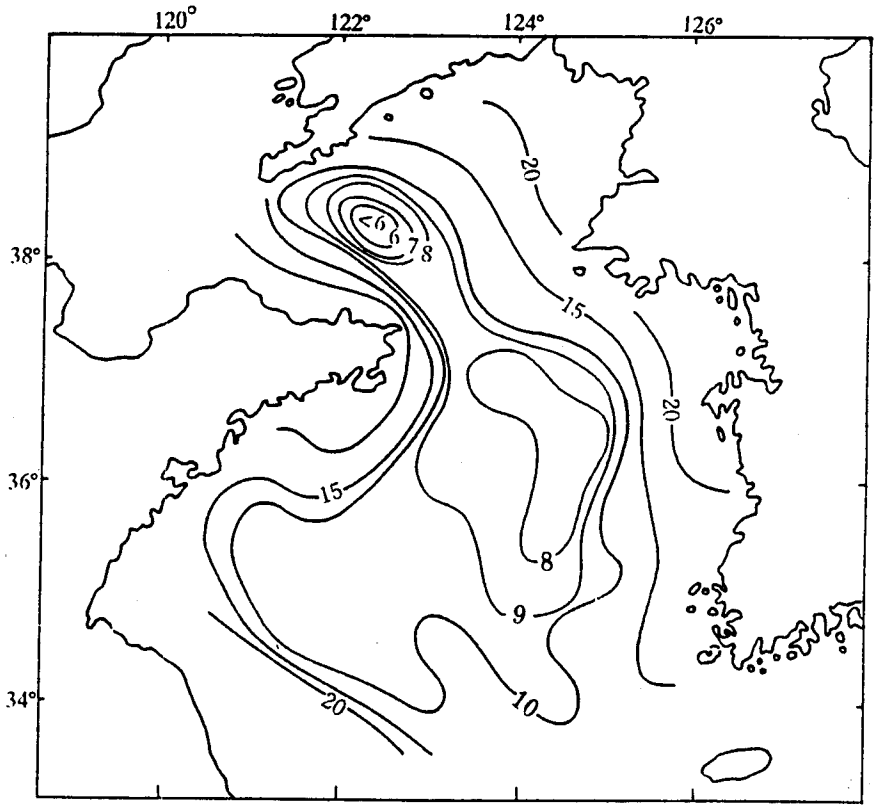

Figure 4.7 Temperature Distribution in Summer (April-November) of the 'Cold Water Mass of the Yellow Sea' (CWYS) Near the Sea Floor (from Su and Weng, 1994). Isotherms in Degrees Celsius.

spatial difference or lag is then calculated between the two anomalies. The anomaly pairs $(T_o', \hat{T}_o')$ are then placed in the corresponding temporal and spatial lag bin.

Three separate data runs were conducted. The first data run was to use separate seasons and individual years from 1963 to 1977. The second run was to use all the MOODS data binned by season. There was no delineation between years; therefore an observation from 23 January 1963 could be paired with an observation from 24 January 1969 and only have a lag time of one day. The third run also included the entire data set binned seasonally but each observation retained its year.Hence, it was paired with observations of the same year, then sorted into the matrix. For simplicity the different input types will be referred to as Type I, Type II, and Type III.

The number of observations in the data set (N) will determine the number of pairs that can be binned. The number of pairs (S) is computed by

$$S = \frac{N(N-1)}{2} \qquad (4.1)$$

In Type I and Type II data the computation S is straight forward but for Type III the value of S is the summation of S for each individual year. As to be expected, Type I has the fewest pairs in each bin. It ranges from one pair to a high of 2000 pairs. In contrast Type II ranges from approximately 750 to over 24000 pairs and Type III from approximately 40 to the 4000. Figure 4.8 shows the pair distribution of Type I and Type II. It can be easily seen that the Type I scheme (Figure 4.8a) produced three main (green) concentrations of profile pairs, the other areas lack substantial data. Type II (Figure 4.8b) has a much higher and more even distribution. From this lack of data in Type I it was determined that statistically relevant information could not be obtained. This study will analyze the advantages and disadvantages of Type II and Type III data.

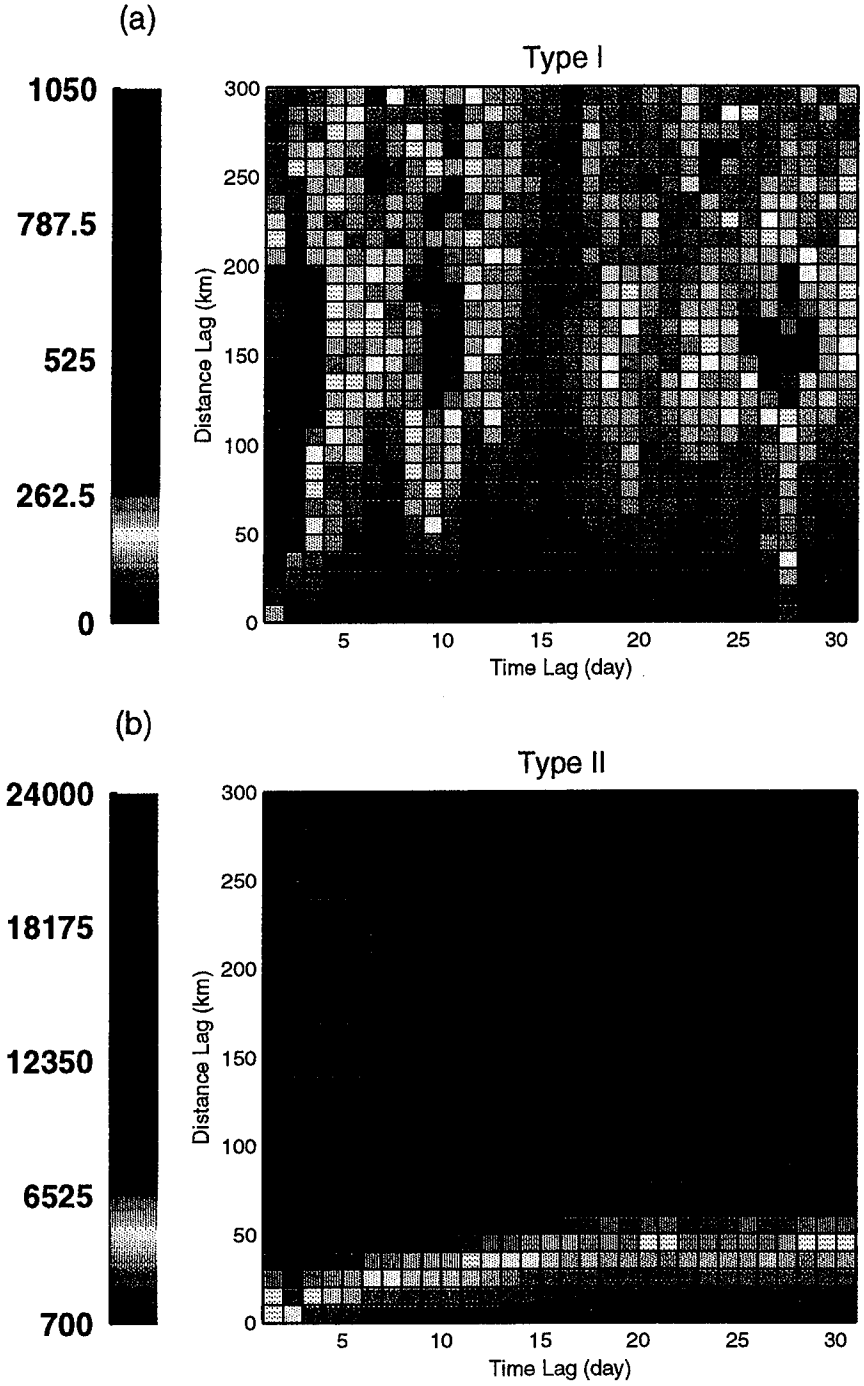

Figure 4.8 Contour Plots of Time-Distance Lag Pair Distribution (a) TYPE I for Spring of 1969 and (b) TYPE II for Spring.

D. AUTOCORRELATION FUNCTION

After the anomaly pairs have been spatially and temporal sorted, an autocorrelation function ($\eta(m,n)$) for each bin with temporal lag $n\Delta t$ and horizontal lag $m\Delta\gamma$ (Δt = 1 day, $\Delta\gamma$ = 10 km) identified as the *bin (m, n)* is computed by

$$\eta(m,n) = \frac{\sum_{bin\,(m,n)} T_o' \hat{T}_o'}{\sqrt{\sum_{bin\,(m,n)} T_o'^2}\sqrt{\sum_{bin\,(m,n)} \hat{T}_o'^2}} \qquad (4.2)$$

Figure 4.9 shows the temporal variation of autocorrelation ((m,n) at the surface for the winter season of Type II and Type III data. The three curves on each graph show the dependency of $\eta(m,n)$ on temporal lag nΔt for three different spatial lags: m = 0 (no lag, dash-dot), m = 1 (10 km lag, solid), and m = 15 (150 km lag, dots). Such a decrease of $\eta(m,n)$ with $n\Delta t$ reveals approximately a Gaussian type relation. On both graphs there is no unity or a correlation of one at zero lag. This occurs since the covariance estimates at zero temporal lag did not include products of each data point with itself and also because substantial subgrid noise was present (White et al., 1982). $\eta(0,0)$ is greater for Type III than the Type II computations which is expected since temperatures of the same year are being compared with each other. Type II plots (Figure 4.9a) are much smoother than the Type III plots (Figure 4.9b). This high frequency temporal variability may be induced by a smaller data base and by forcing mechanisms like meteorological, tidal and freshwater runoff that were averaged out in the Type II computations but are clearly recorded in the Type III calculations. It is unclear how many or what type of natural forcing mechanisms are creating this variability or if it is an artifact of having too little data

that artificially induces variability. In each case the e-folding time for zero lag distance is approximately 13 days.

The spatial autocorrelations showed similar characteristics (Figure 4.10). Type III had higher autocorrelations at zero lag. Variability is large in the Type III scheme and the reason for this is still unclear. The e-folding distance for Type II data was roughly estimated from Figure 4.10 to be approximately 125 km while for the Type III it is 150 km. Since the e-folding scales are similar for both computations (Type II and Type III) and Type II exhibits statistical stability, the Type II computations were considered the more appropriate choice in calculating the decorrelation scales.

E. E-FOLDING DECORRELATION SCALES OF THE YELLOW SEA THERMAL FIELD

With regard to the surface and subsurface thermal indicator parameters, the e-folding temporal and spatial decorrelation scales can be obtained from the autocorrelation coefficient function, $\eta(m, n)$. The variations of $\eta(m, n)$ verses the horizontal spatial and temporal lags ($m\Delta\gamma$ and $n\Delta t$) reveals a Gaussian-type dependency (e.g., Figure 4.9). The autocorrelation matrices $\eta^{(k)}(m, n)$ are fitted by the Gaussian function

$$\eta^{(k)}(m, n) = \eta^{(k)}_{(0, 0)} e^{-A_k^2 (m\Delta\gamma)^2 - C_k^2 (n\Delta t)^2} \qquad (4.3)$$

where k denotes the different levels (k =1 for the surface, k =2 for the 50% water column depth, and k =3 for the 80% water column depth). The regression coefficients, A_k^{-1} and C_k^{-1}, are the e-folding horizontal spatial and temporal decorrelation scales. For a given time lag $n\Delta t$, the coefficient A_k^{-1} is interpreted as an e-folding distance, $m_i\Delta\gamma$, for the level k

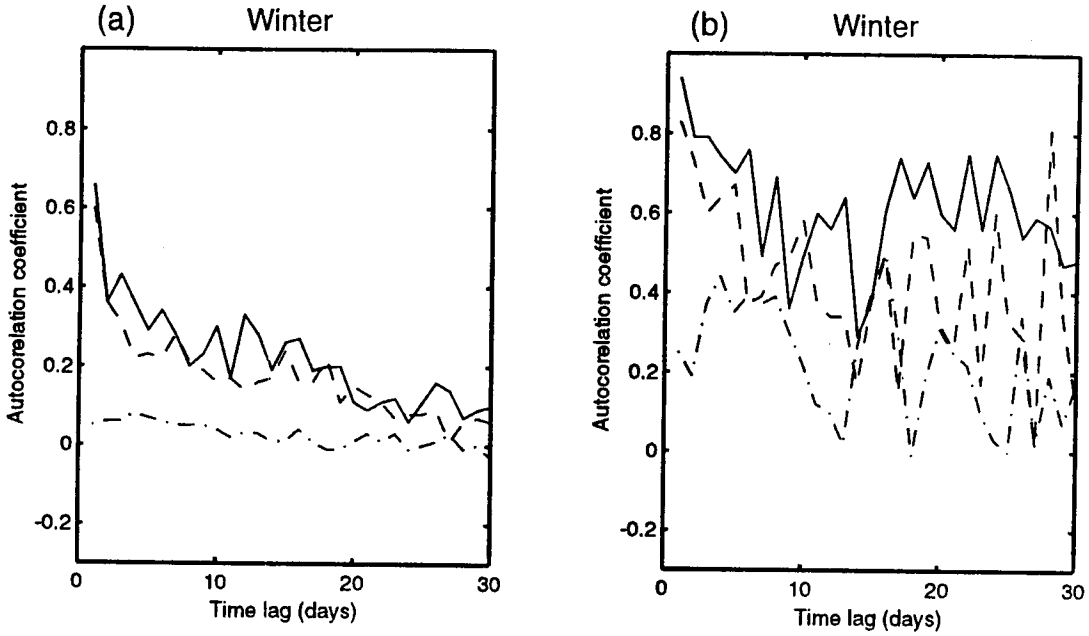

Figure 4.9 Temporal Variations of Autocorrelation Function $\eta\,(m, n)$ for (a) Type II and (b) Type III Data at the Surface.The Three Curves on Each Graph are the Dependency of $\eta\,(m, n)$ on Time Lag $n\Delta t$ for $m = 0$ (no lag, dash-dot), $m = 1$ (10 km lag, solid), and $m = 15$ (150 km lag, dots). Data were Obtained from the MOODS Temperature Data Base for the Years 1929 to 1991.

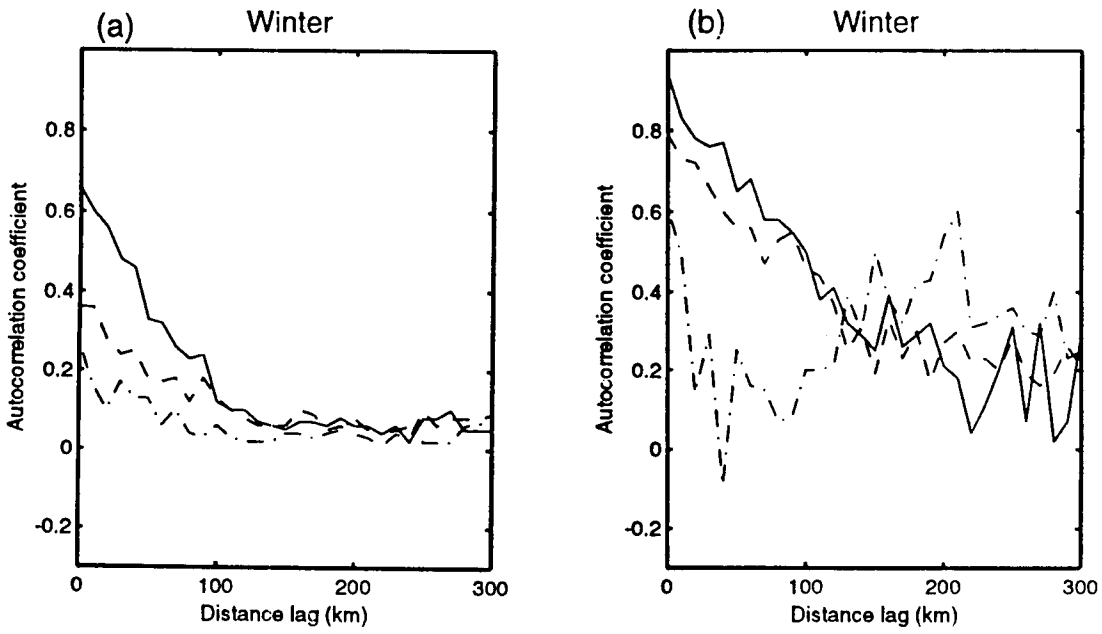

Figure 4.10 Spatial Variations of Autocorrelation Function $\eta(m, n)$ for (a) Type II and (b) Type III at the Surface. The Three Curves on Each Graph are the Dependency of $\eta(m, n)$ on Spatial Lag $(m\Delta\gamma)$ for $n = 0$ (no temporal lag, dash-dot), $n = 1$ (1 day lag, solid), and $n = 15$ (15 day lag, dots). Data were Obtained from the MOODS Temperature Data Base for the Years 1929 to 1991.

$$-A_k^{\,2}(m_i\Delta\gamma) = ln\frac{\eta^{(k)}(m_i, n)}{\eta^{(k)}(0, n)} = -1 \qquad (4.4)$$

where the autocorrelation function reduces from zero spatial lag, $\eta^{(k)}(0, n)$, to $m_i\Delta\gamma$ spatial lag, $\eta^{(k)}(m_i, n) = e^{-1}\eta^{(k)}(0, n)$.

Similarly, for a given spatial lag $(m\Delta\gamma)$, the coefficient C_k^{-1} is interpreted as an e-folding temporal separation $(n_i\Delta t)$ for the level k

$$-C_k^2(n_i\Delta t)^2 = ln\frac{\eta^{(k)}(m, n_i)}{\eta^{(k)}(m, 0)} = -1 \qquad (4.5)$$

where the autocorrelation function reduces from $\eta^{(k)}(m, 0)$ to $\eta^{(k)}(m, n_i) = e^{-1}\eta^{(k)}(m, 0)$.

F. SIGNAL-TO-NOISE RATIO

In applying the optimum interpolation for the OTIS model or an optimal network design, certain statistics of the field of interest such as the variance of both the signal and the noise must be known. The signal variance for the *bin (m, n)* is estimated by

$$\sigma^2_{s(m,n)} = \sum_{bin\,(m,n)} \hat{T}'^2_o \qquad (4.4)$$

The noise variance is derived from two sources (Sprintall and Meyers, 1991), geophysical error and instrument error. Geophysical error is unresolved thermal variability with scales smaller than the typical time and distance scales between two temperature profiles. Instrumental error can be shown to be negligible compared to geophysical noise (White and Bernstein, 1979). These noise sources inhibit the

detection of large-scale variability and can be an important factor in establishing the sampling density necessary to detect the signal (Sprintall and Meyers, 1991).

In calculating the autocorrelation value of the first bin (zero to 1 day and zero to 10 km lag) the temperature anomalies were never paired with themselves. The values of the autocorrelation coefficient function at zero temporal and spatial lag [η (0, 0)] were extrapolated from the first bin into the origin. Therefore, η (0, 0) is not equal to 1.0. The relationship between the temperature signal and the noise signal can be described by the signal-to-noise parameter (Sprintall and Meyers, 1991)

$$\lambda = \sqrt{\frac{\eta\,(0,0)}{1-\eta\,(0,0)}} = \frac{\sigma_s}{\sigma_n} \qquad (4.5)$$

where σ_n^2 is the noise variance and σ_s^2 is the signal variance. λ represents the signal-to-noise ratio or level. The larger the λ, the less noise that exists in the bin. Theoretically, if there is no noise, η (0, 0) = 1 and $\sigma_n^2 = 0$. Therefore λ will be ∞. If $\lambda > 2$, the ratio of the signal variance, σ_s^2, to the noise variance, σ_n^2, is greater than 4 which is considered good by White et al. (1982) and Sprintall and Meyers (1991).

V. DISCUSSION

A. TEMPORAL AND SPATIAL DECORRELATION SCALES

All temperature profiles from 1929 to 1991 were used in the calculation of temporal and spatial decorrelation scales. Delineation of separate years within the autocorrelation computations was not permitted (Type II averaging) which averaged the various forcing mechanisms prevalent in this shallow water basin. The computed autocorrelations for each season were then fitted to a Gaussian function of the form of (4.3). The regression method was used to calculate the spatial and temporal decorrelation scales at three different levels, A_k^{-1} and C_k^{-1}, respectively. Since an isotropic assumption concerning the spatial temperature distribution was made, there was no directional dependency. This means that decorrelation scales were assumed to be the same throughout the Yellow Sea basin. Table 5.1 presents these decorrelation scales and signal-to-noise ratios for winter and summer.

Season	Depth	Temporal (days)	Spatial (km)	Signal-to noise ratio(λ)
Winter	sfc	14.7	158	2.06
	50%	14.7	167	1.88
	80%	15.2	172	2.21
Summer	sfc	12.3	251	3.0
	50%	15.8	169	2.21
	80%	17.2	157	3.0

Table 5.1: Seasonal Temporal and Spatial Scales

The signal-to-noise ratio for both winter and summer are higher than the signal-to-noise ratio for the deep waters of the Eastern Equatorial Pacific (~ 1.0) as reported by Sprintall and Meyers (1991). This infers that the temperature signal in

this study is stronger (more stable) than the background noise. In both seasons the smallest signal occurs at the 50% water column depth. This is expected since this is the transitional (thermocline) depth between the surface layer and the deep layer, where meteorological and topographic effects occur. The surface signal-to-noise ratio was smaller in winter than in summer.

Winter temporal and horizontal decorrelation scales are the smaller than summer and exhibit nearly uniform values at all three depths. The temporal scales vary only by a half a day and the horizontal scales by only 14 km. This uniformity is expected considering the oceanographic conditions of the region. Sea surface icing occurs to the north in the Bohai Sea and the northern Yellow Sea and along the northern coastal regions of Korea and China. Temperatures range from freezing in the north to 20°C in the south along the shelf break. This large temperature range will inherently make horizontal decorrelation scales small. Vertically, winter experiences the greatest mixing (Nester,1977) with monsoonal winds at their strongest throughout the entire season. With a large part of the Yellow Sea having depths less than 50 m, mixing reaches to the bottom creating isothermal profiles. Thus, decorrelation scales will be similar from the surface to the 80% water column depth.

Summer surface spatial decorrelation scales are 100 km longer than winter. This is reasonable since this region experiences large solar heating in the summer. The summer climatology (Appendix C, Figure C.1) shows the SST to be nearly constant throughout the region. The surface temporal scale is less by five days than at deeper depths. This may be due to a combination of factors. Besides the large solar heating that occurs in the summer, the summer monsoonal winds are much weaker than the winter winds. Therefore, vertical mixing is not as great as in winter. A strong thermocline is present in summer. Thus, the upper layer water is affected by the meteorological synoptic events rather than the entire water column as is in

winter. The temporal scale at the surface should be shorter in summer than in winter (Table 5.1). In the deeper layers (50% and 80% depths) temperatures are not directly affected by the meteorological events of the surface and experience longer temporal scales. The 80% water column depth has the longest temporal scale which could be directly related to the 'Cold Water Mass of the Yellow Sea' (CWYS) (Li and Yuan, 1992) that exists throughout the summer in the middle of the Yellow Sea. Spatial scales are close to 100 km smaller than that at the surface. Without the extreme vertically mixing, the CWYS retains some its winter water mass characteristics from which it is derived (Liu et al., 1992) and remains a distinct cold water mass that resists mixing. This will cause smaller decorrelation scales.

B. OBSERVATIONAL NETWORK DESIGN

The temporal and horizontal decorrelation scales provide useful information for an optimal design of an observational network. The principle is to minimize both instrumental and geophysical errors. Since noise due to instrumental error in XBT measurements is usually only about 0.1°C (Barnett and Bernstein, 1980), and even smaller in CTD measurements, instrumental error can be neglected. This implies that the reduction of noise must be accomplished by the reduction of geophysical error. This is usually done by increasing the sample density. Sprintall and Meyers (1991) suggested that an optimal sampling density of two or three samples per decorrelation scale would be adequate to resolve thermal variability.

This would mean that spatially, any future temperature measurement in the winter may be conducted at 50-80 km intervals with the knowledge that the subsurface features will also be adequately sampled. The summer season will require more consideration. If only surface features are considered, a larger measurement interval of 80-125 km may be used. In order to provide full coverage

of subsurface features a 50-80 km interval is recommended.Temporally, a 4-6 day sampling interval will provide the minimal coverage for both seasons.

C. UNCERTAINTIES IN THE TRANSITIONAL SEASONS

The transitional seasons, spring and fall, showed unusual temporal and spatial decorrelation scales (Table 5.2). The scales were significantly larger than in winter or summer. The spatial surface scales computed are 521 km in the spring and 757 km in the fall. It might be expected that the transitional surface scales be longer than winter and summer due to the lack of meteorological synoptic forcing or the tendency for the temperature contours (Appendix C), especially in spring and to a lesser degree in fall, to rap around or follow the coastline around the Yellow Sea basin. This could mean that an eastern coastal temperature profile would be more correlated to a western coastal profile 300 km away than it is to the profiles in the

Season	Depth	Temporal (days)	Spatial (km)	Signal-to noise ratio(λ)
Spring	sfc	20.5	521	4.9
	50%	17.7	226	2.48
	80%	18.0	204	2.38
Fall	sfc	18.0	757	4.9
	50%	16.9	278	2.48
	80%	18.2	179	2.59

Table 5.2: Seasonal Temporal and Spatial Scales

middle of the basin that are closer. In either case, the extremely large scales are unrealistic if not for the only reason that the enclosed Yellow Sea basin itself is approximately 450 km in the east-west direction and over 700 km in the north-south direction.

The temporal scales are approximately six days longer than in winter and summer. There was no evidence to support these larger values. Since the onset or cessation of seasonal changes vary from year to year and this study specifically defined April, May and June as spring and October, November, and December as fall, statistical errors are expected. It is highly recommended that future studies examine different month groupings for these transition seasons.

Vertically both the temporal and spatial scales decreased with depth. The larger change is in the spatial scales. In spring there was a 300 km and in fall a 500 km difference from the 50% and 80% depths to that at the surface. As stated earlier, these findings seem highly improbably and the irregularities of the MOODS data and the determination of season must be examined further.

D. LIMITATIONS

The purpose of this study was to calculate the seasonal temporal and spatial decorrelation scales to be used by OTIS. Scales were obtained but the validity of these findings must be examined and a potential user discouraged from blindly implementing these scales into various models.

The isotropic assumption of uniform conditions throughout the basin was based on the existence of closed isotherms for the majority of the time in the Yellow Sea basin. This made computations feasible and provided a general reference for temporal and horizontal scales. In reality, there probably exists a similar latitudinal and longitudinal dependence as in deep water (White et al., 1982; Sprintall and Meyers, 1991). This is due to the fact that isotherms are not closed year round, the basin is elongated in the north-south direction and coastal regions typically have different cross-shore and along-shore scales. Thus, future studies should examine the possibilities of calculating two directional scales.

The convention used in defining seasons can have a large statistical impact. The convention used in this study was recommended by the Naval Oceanography Office. It was found that spring and fall had unrealistic surface scales which may be a direct result of the seasonal binning. A more realistic approach may be to define spring and fall as two months or less in duration as opposed to three used in this study.

The MOODS data base is a limiting factor of itself. In this study, decorrelation scales that pertain to the entire Yellow Sea basin were desired. Yet, the data were biased in location (Appendix B). Most of the profiles were located in the eastern region of the sea, with significantly fewer in the Bohai Sea and along the coastline of China. Temporally the profiles were irregular (Appendix A) from month to month and year to year. This irregularity led to the analysis of three different computational schemes.

The first scheme, Type I, calculated autocorrelations on a yearly basis. Values were erroneous since not enough data existed to produce statistically relevant results. Type II calculations used the entire MOODS data base but no delineation was permitted between years. This scheme averaged the high frequency variability such as meteorological events, tidal forcing and river runoff. This scheme showed a definite seasonality (Appendix D) both temporally and spatially. Type III calculations also used the entire MOODS data but this time temperatures were paired with only temperatures of the same year. Although the autocorrelations computed from Type II and Type III schemes are similar, the Type III scheme produced large variability both temporally and spatially (Appendix D). It is not known if the variability is statistically produced by a smaller data base or are the result of the many shallow water forcing mechanisms. Therefore, more effort is needed to determine the best use for both schemes.

The last limitation to be discussed is the fitting function. Even though it is customary to fit the calculated autocorrelations to a Gaussian curve, as in the OTIS model, it may not be the most accurate procedure for shallow water. The winter and summer autocorrelations rapidly decreased in time and space. The spring and summer curves did not. In future studies it may be better to use a combination of a linear function and a Gaussian curve.

VI. CONCLUSION

The goal of this study was to compute seasonal temporal and spatial temperature autocorrelation scales for the Yellow Sea. These scales are an integral part of the accurate running of the OTIS model which at this time is designed for deep water thermal analysis. Decorrelation scales were calculated for three depths, i.e., the surface and at 50% and 80% of the water column depth, and for four seasons. Variations were found to be both seasonally and depth dependent.

The temperature data were comprised of approximately 36,000 observed profiles from the MOODS worldwide data base. All profiles were located on the continental shelf and spanned the time period of 1929 to 1991. The widely irregular distribution of temperature profiles in time and space made yearly analysis statistically irrelevant. Two time-organized schemes were analyzed: (1) temperatures were paired with no delineation between years, referred to as Type II data and, (2) temperatures paired with temperatures of the same year, referred to as Type III data. The Type II scheme was used in the calculation of the temporal and spatial scales since it produced a larger data set and averaged the high frequency variability due to individual forcing mechanisms.

The winter season had the smallest temporal and spatial scales of the four seasons. This is attributed to the strong cold monsoonal winds which produced the strongest vertical mixing of all the seasons and the extreme temperature range extending from freezing in the north to 20°C in the south along the continental shelf. The temporal decorrelation scales approximated to 15 days and spatial decorrelation scales to 165 km at all depths.

The summer season had the next smallest scales, but unlike winter it showed some vertical variability. The scales range from 12.3 days and 251 km at the surface

to 17.2 days and 157 km at 80% depth. The approximately 100 km difference between the levels is due to the lack of vertical mixing and the presence of CWYS.

An optimal network design was suggested. It was found that a 50-80 km interval will provide adequate sample density to discern winter features. The summer season exhibits a surface and subsurface minimum density interval. To discern only surface features a 80-125 km interval is adequate but for complete depth coverage a 50-80 km interval should be used. Temporally, a 4-6 day sampling interval will provide coverage for both seasons.

The use of these scales in the OTIS model must be cautiously considered. The inherent problems in the MOODS data base, irregularity in space and time, the organization of the data base into seasons and the neglect of different forcing mechanisms all have an effect on the calculation of the temporal and spatial scales. More temperature profiles and analysis is required in order to better refine these scales and improve the OTIS model.

LIST OF REFERENCES

Barnett, T.P., and R.L. Bernstein, Expendable measuring devices, in *Air-Sea Interaction Instruments and Methods*, edited by F. Dobson, L. Hasse, and R. Davis, pp. 387-398, Plenum, New York, 1980.

Bartz, P., 1972: *South Korea.* Oxford University Press, New York.

Cheang, B.K., Short- and long-range monsoon prediction in Southeast Asia, in *Monsoons*, edited by J.S. Fein and P.L. Stephens, pp. 579-606, Wiley-Interscience, New York, 1987.

Clancy, R.M., P.A. Phoebus and K.D., Pollak, Technical description of the Optimum Thermal Interpolation System, Version 1: A model for oceanographic data assimilation, U.S. Naval Ocean Research and Development Activity Report No. 240, Stennis Space Center, MS, 1989.

Elms, J.D., U.S. Navy regional climatic study of the central east Asian coast and associated waters, U.S. Naval Oceanography Command report NAVAIR 50-1C-556, 1990.

Gandin, L. S., 1965: Objective Analysis of Meteorological Fields, *Israel Progrm for Scientific Translations*, Jerusalem, pp. 242.

Guan, B.X., Patterns and structures of the currents in the Bohai, Huanghai and East China Seas, in *Oceanology of China Seas*, edited by Y. Liang and C.K. Tseng, pp. 17-26, Kluwer, Boston, 1994.

Haeger, S.D., Variability of shallow water temperature structure and its impact on construction of climatological data base, Proceedings of the Marine Technology Society Conference, New Orleans, LA, November 1991.

Hsueh, Y., Recent current observations in the Eastern Yellow Sea, *J. Geophys. Res.*, 93, 6875-6884, 1988.

Hu, D.X., Some striking features of circulation in Huanghai Sea and East China Sea, in *Oceanology of China Seas*, edited by Y. Liang and C.K. Tseng, pp. 27-38, Kluwer, Boston, 1994.

Krishnamurti, T.N. and H.N. Bhalme, Oscillations of a monsoon system. Part I. Observational aspects, *J. Atmos. Sci.*, 33, 1937-1954, 1976.

Langill, R.H., Forecasting Guide for the Republic of Korea, Det. 18, 20th Weather Squadron, 1st Weather Wing, USAF, 1976.

Li, H. and Y. Yuan, On the Formation and maintenance mechanisms of the cold water mass of the Yellow Sea. *Chin. J. Oceanol. Limnol., 10(2)*, 97-106, 1992.

Liu, S.X., X.Q. Shen, Y.Q. Wang and S.X. Han, Preliminary analysis of distribution and variation of perennial monthly mean water masses in the Bohai Sea, the Huanghai Sea and the East China Sea. *Acta Oceanologica Sinica, 11(4),* 483-498, 1992.

Mooers, C. N. K. and A. R. Robinson, Ocean prediction: The scientific basis and the Navy's needs, Proceedings of the Ocean Predictions Workshop, Monterey, CA, 34, May 1981.

Nestor, M.J.R., The environment of South Korea and adjacent sea areas, U.S. Naval Environmental Prediction Research Facility, Technical Report No. 77-03, Monterey, CA, 1977.

Özsoy, E., A. Hecht and Ü. Ünlüata, Circulation and hydrology of the Levantine Basin, Results of POEM coordinated experiments 1985-1986. *Prog. Oceanography,* 22, 125-170, 1989.

Phoebus, P.A., Improvements to the data selection algorithms in the Optimum Thermal Interpolation System (OTIS), Naval Ocean Research and Development Activity Report No. 239, Stennis Space Center, MS, 1988.

Provost, C., and P.-Y. Le Traon, Spatial and temporal scales in altimetric variability in the Brazil-Malvinas Current confluence region: Dominance of the semiannual period and large spatial scales, *J. Geophys. Res., 98*, 18,037-18,051, 1993.

Sprintall, J., and G. Meyers, An Optimal XBT sampling network for the Eastern Pacific Ocean, *J. Geophys. Res., 96*, 10,539-10,552, 1991.

Su, Y.S. and X.C. Weng, Water masses in China Seas, in *Oceanology of China Seas*, edited by Y. Liang and C.K. Tseng, pp. 3-16, Kluwer, Boston, 1994.

White, W.B., and R.L. Bernstein, Design of an oceanographic network in the midlatitude north Pacific, *J. Phys. Oceanogr., 9*, 592-606, 1979.

White, W.B., G. Meyers, K. Hasunuma, Space/time statistics of short-term climatic variability in the Western North Pacific, *J. Geophys. Res., 87,* 1979-1989, 1982.

APPENDIX A SEASONAL LOCATION PLOTS OF MOODS TEMPERATURE PROFILES FROM 1963 TO 1977

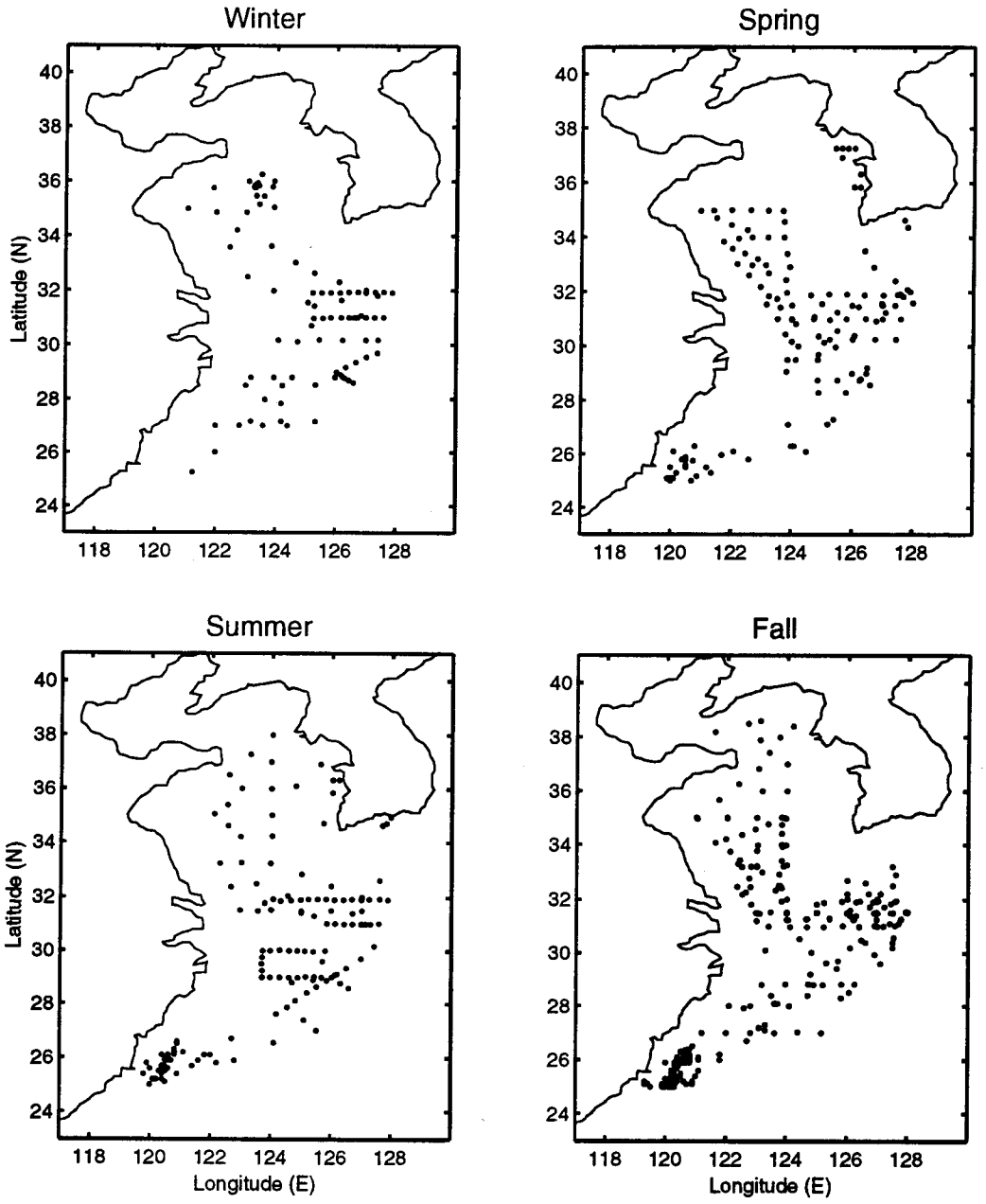

Figure A.1 Seasonal Location of MOODS Temperature Profiles in the Yellow Sea for 1963.

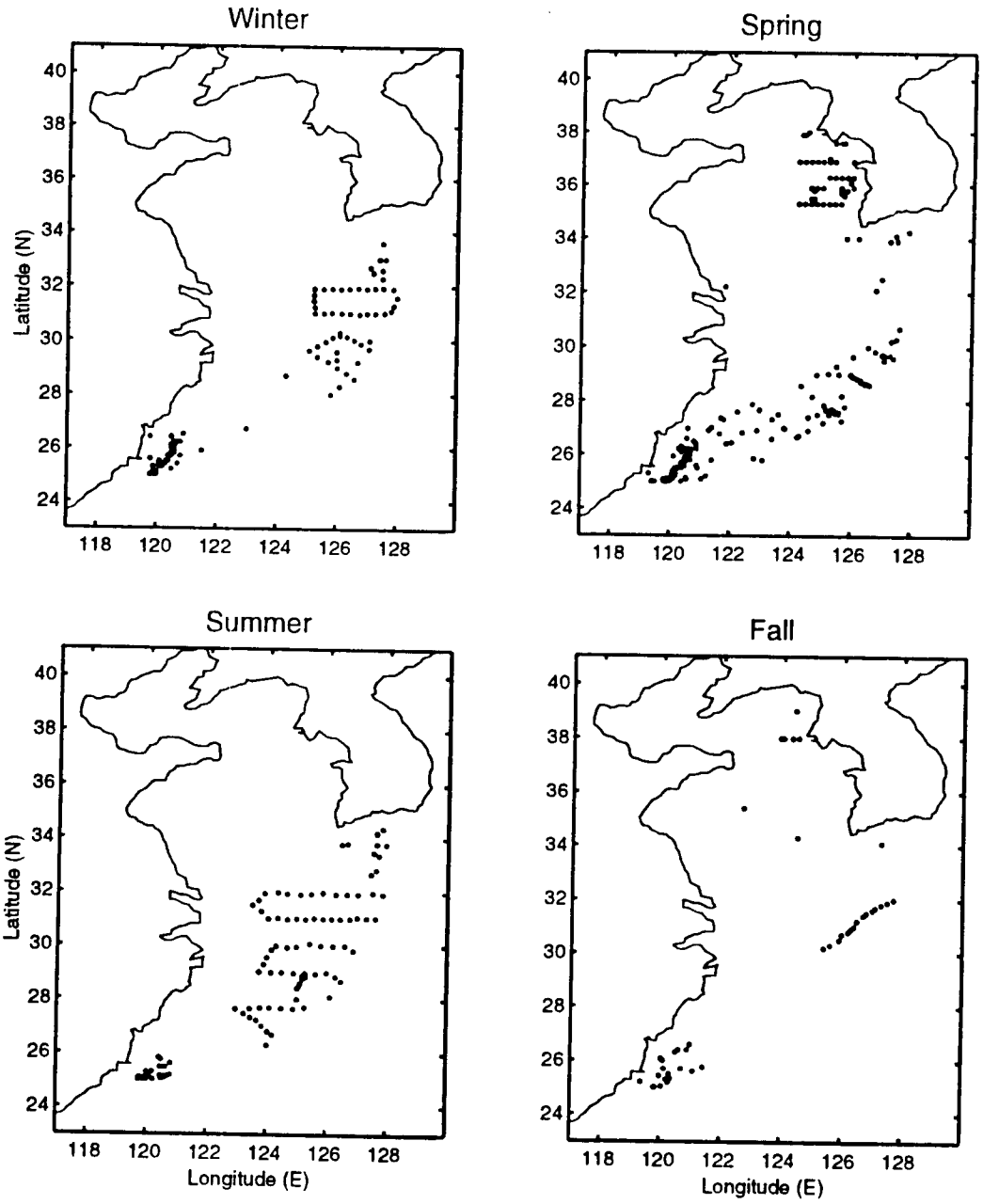

Figure A.2 Seasonal Location of MOODS Temperature Profiles in the Yellow Sea for 1964.

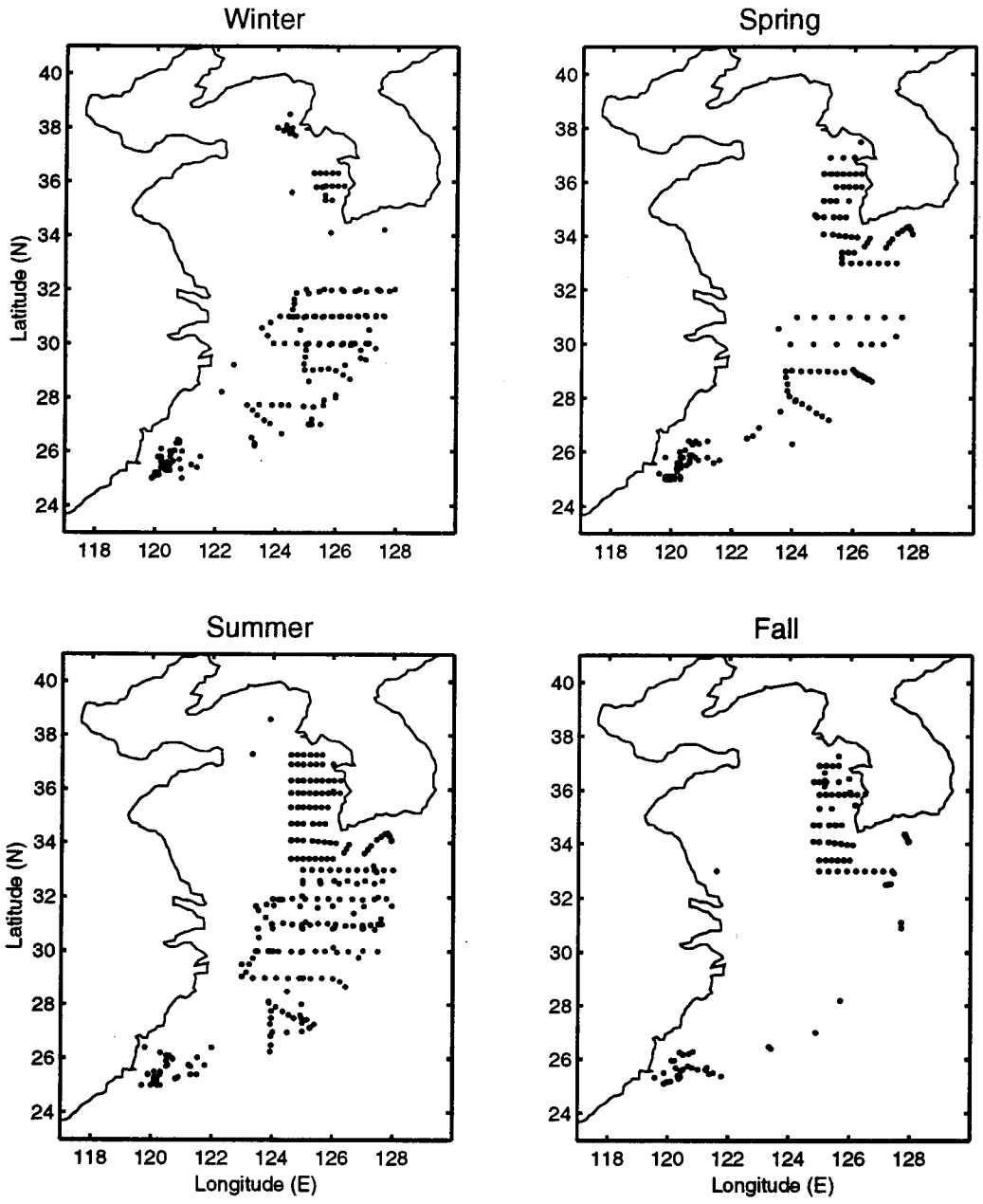

Figure A.3 Seasonal Location of MOODS Temperature Profiles in the Yellow Sea for 1965.

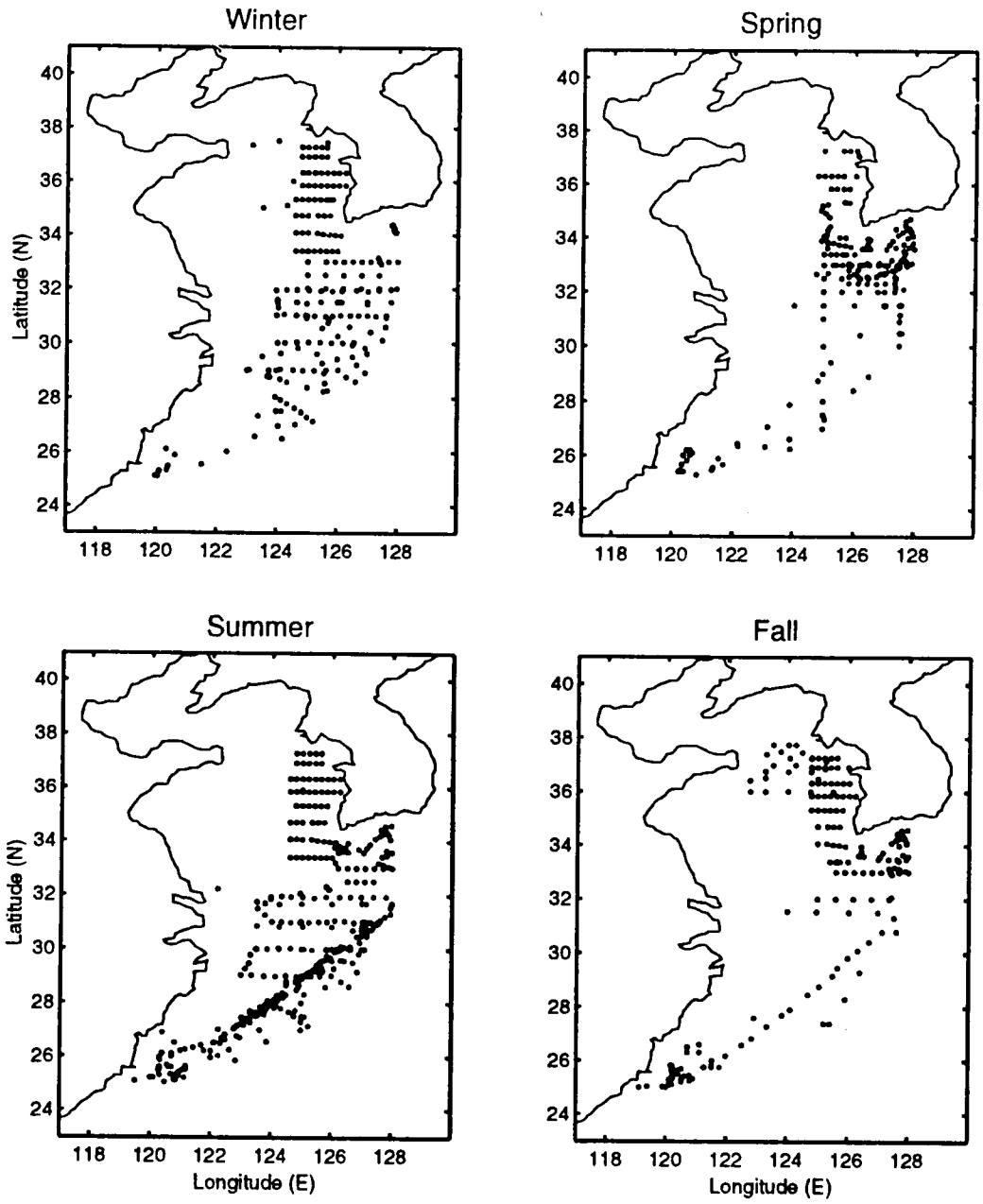

Figure A.4 Seasonal Location of MOODS Temperature Profiles in the Yellow Sea for 1966.

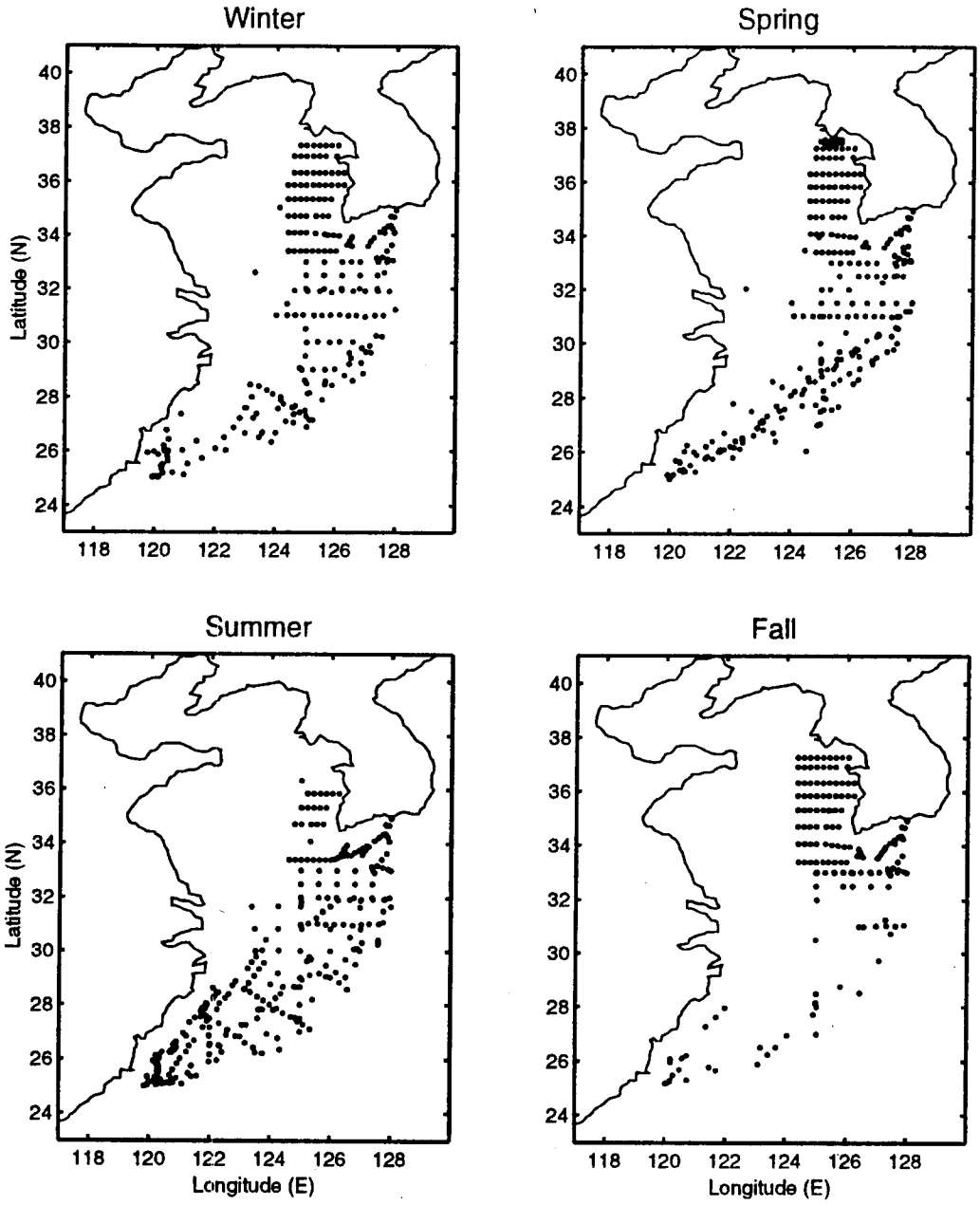

Figure A.5 Seasonal Location of MOODS Temperature Profiles in the Yellow Sea for 1967.

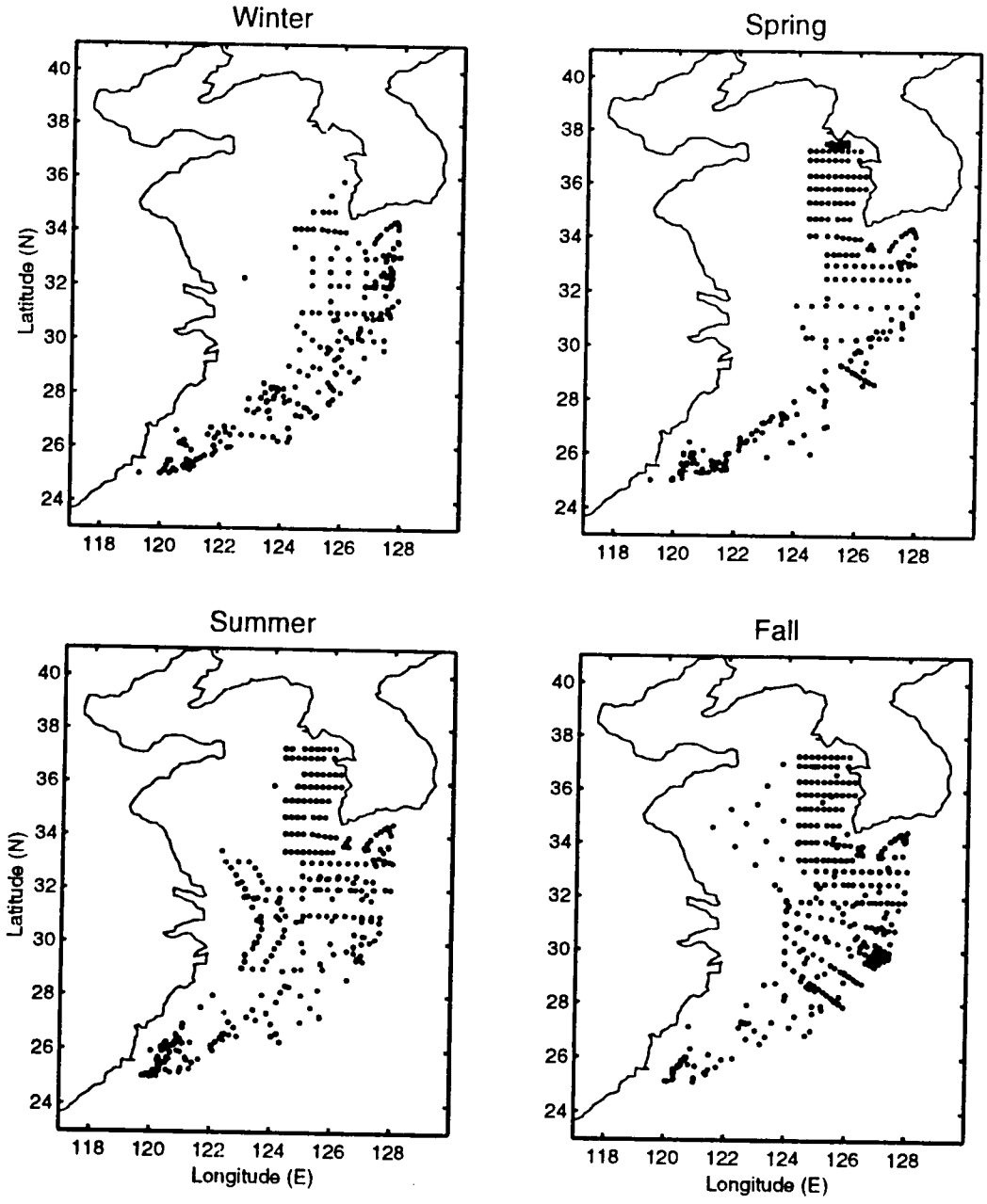

Figure A.6 Seasonal Location of MOODS Temperature Profiles in the Yellow Sea for 1968.

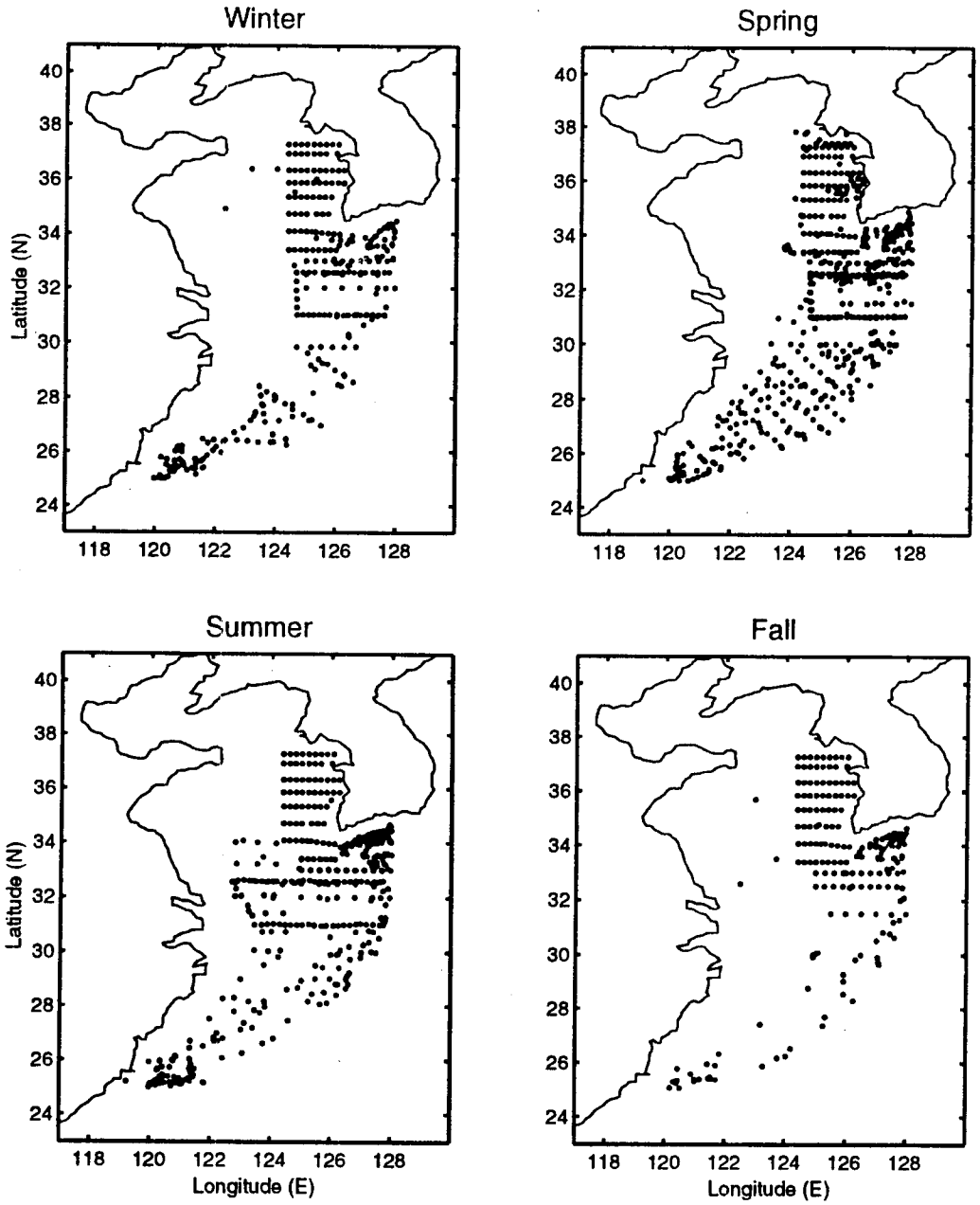

Figure A.7 Seasonal Location of MOODS Temperature Profiles in the Yellow Sea for 1969.

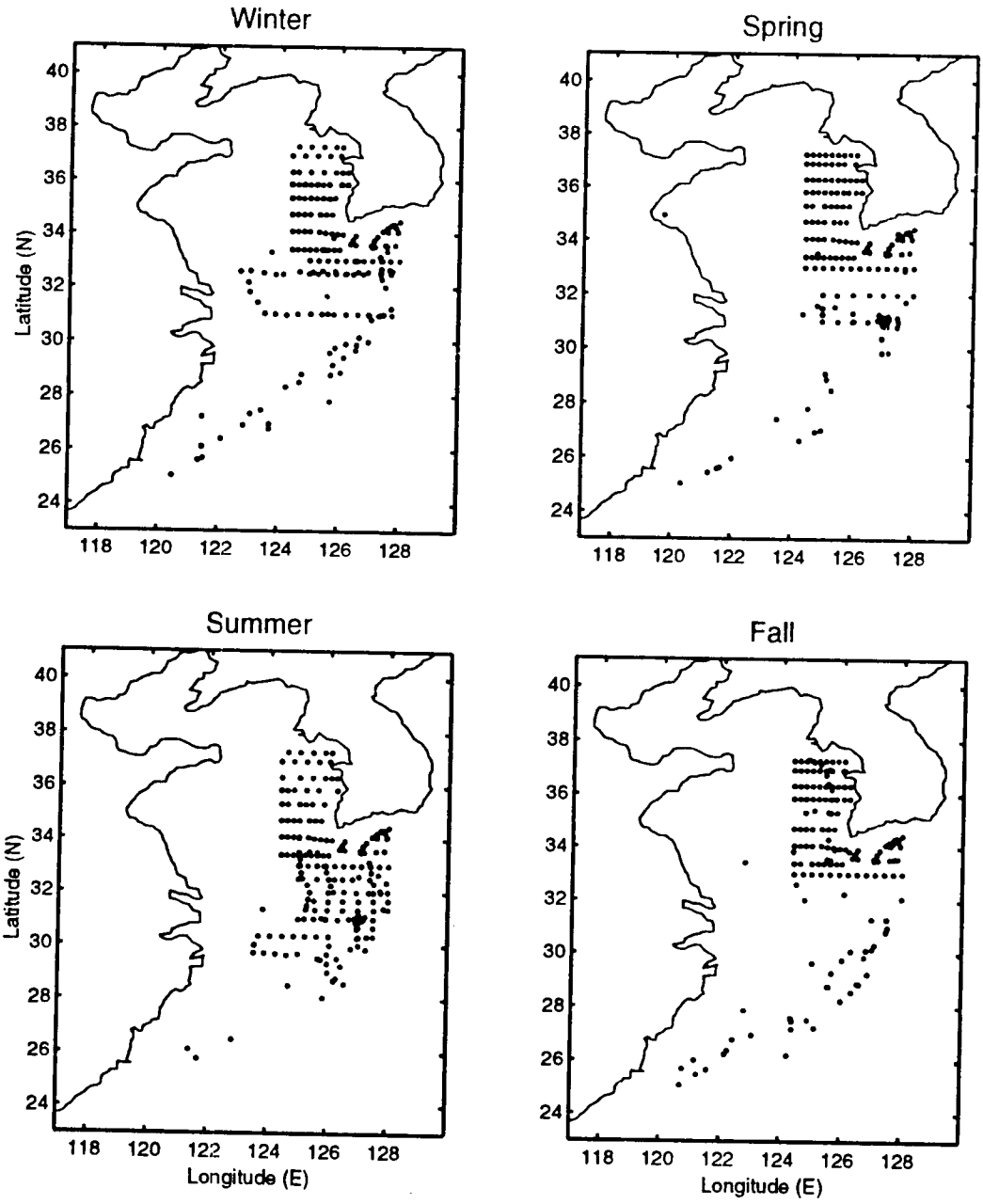

Figure A.8 Seasonal Location of MOODS Temperature Profiles in the Yellow Sea for 1970.

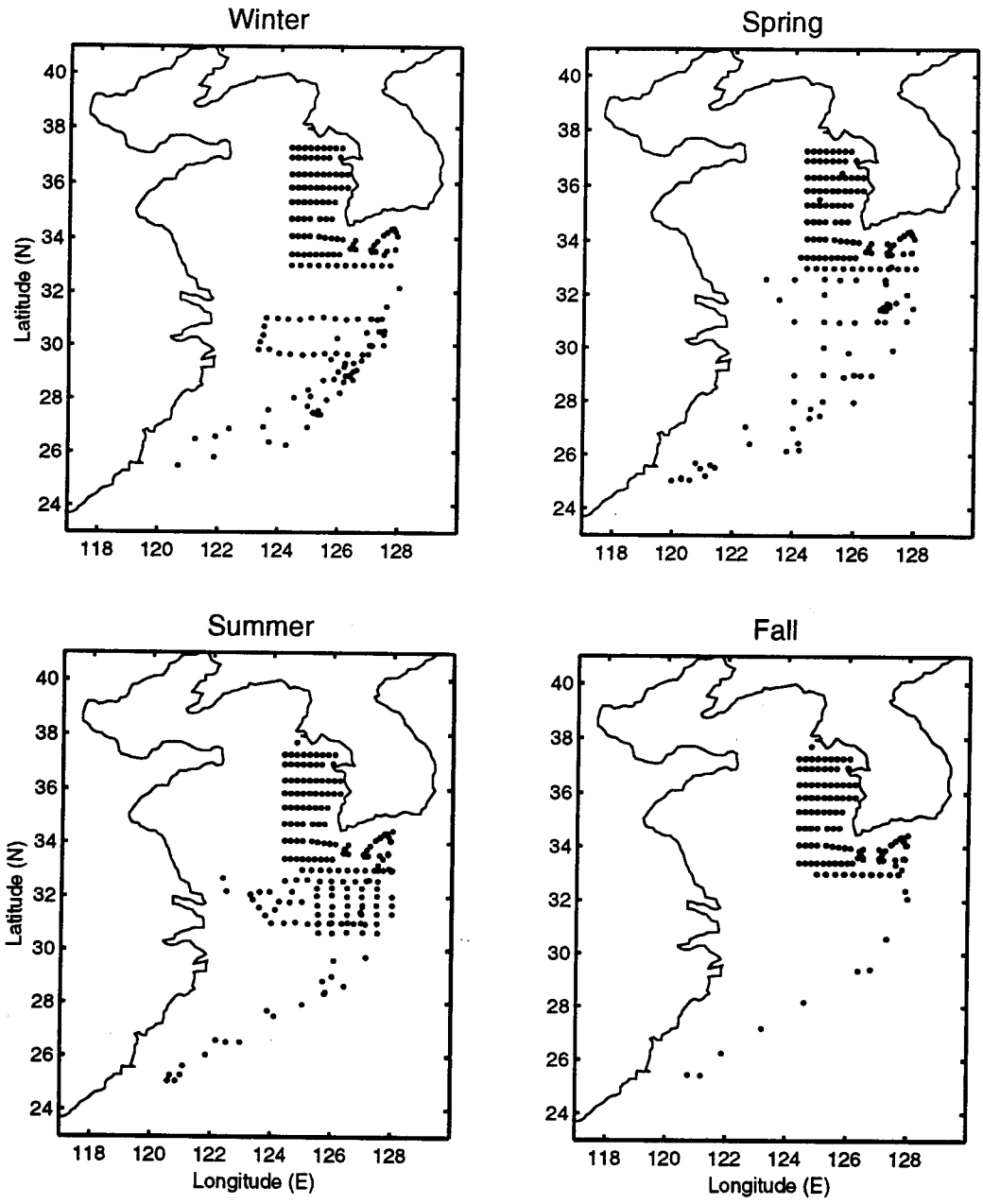

Figure A.9 Seasonal Location of MOODS Temperature Profiles in the Yellow Sea for 1971.

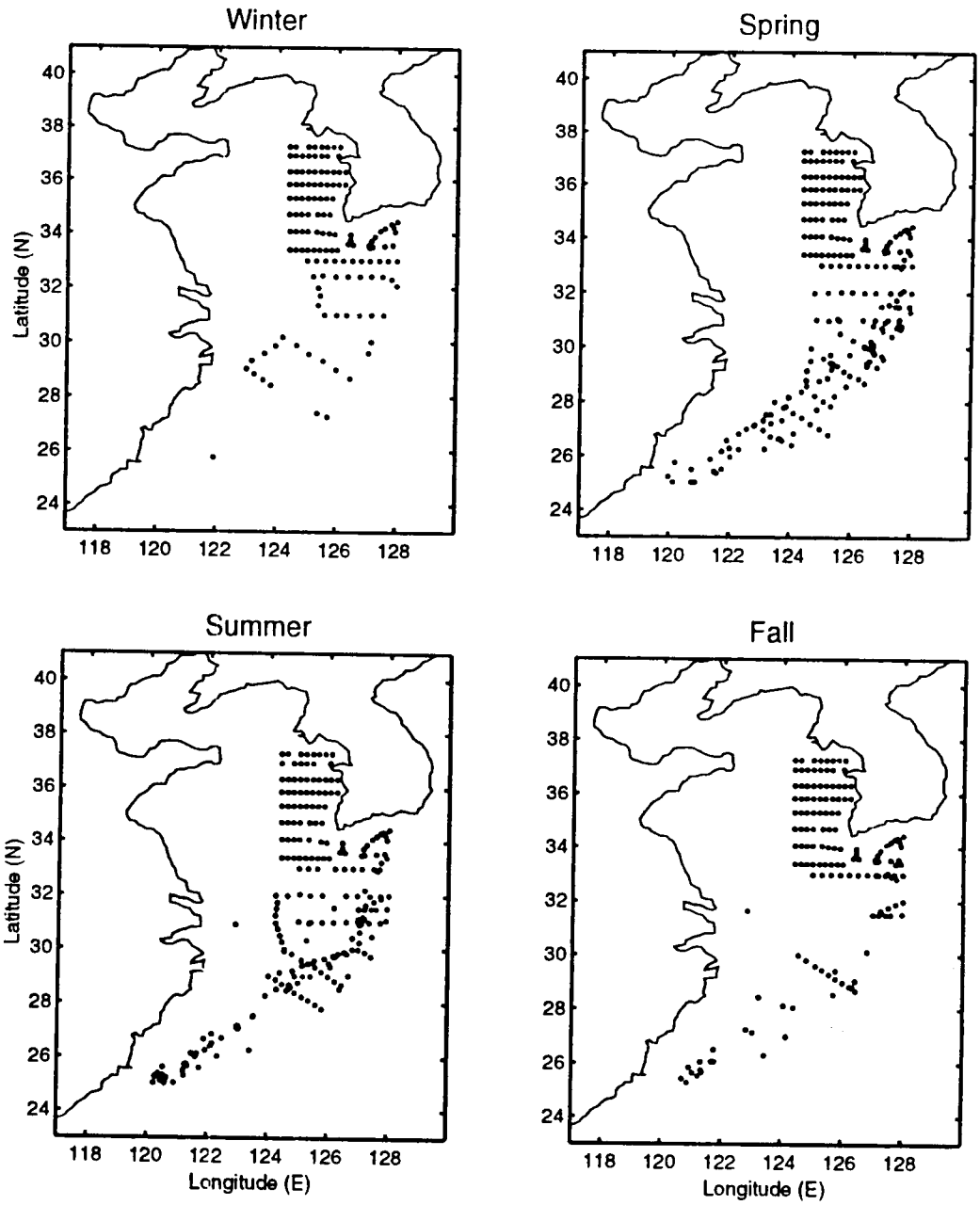

Figure A.10 Seasonal Location of MOODS Temperature Profiles in the Yellow Sea for 1972.

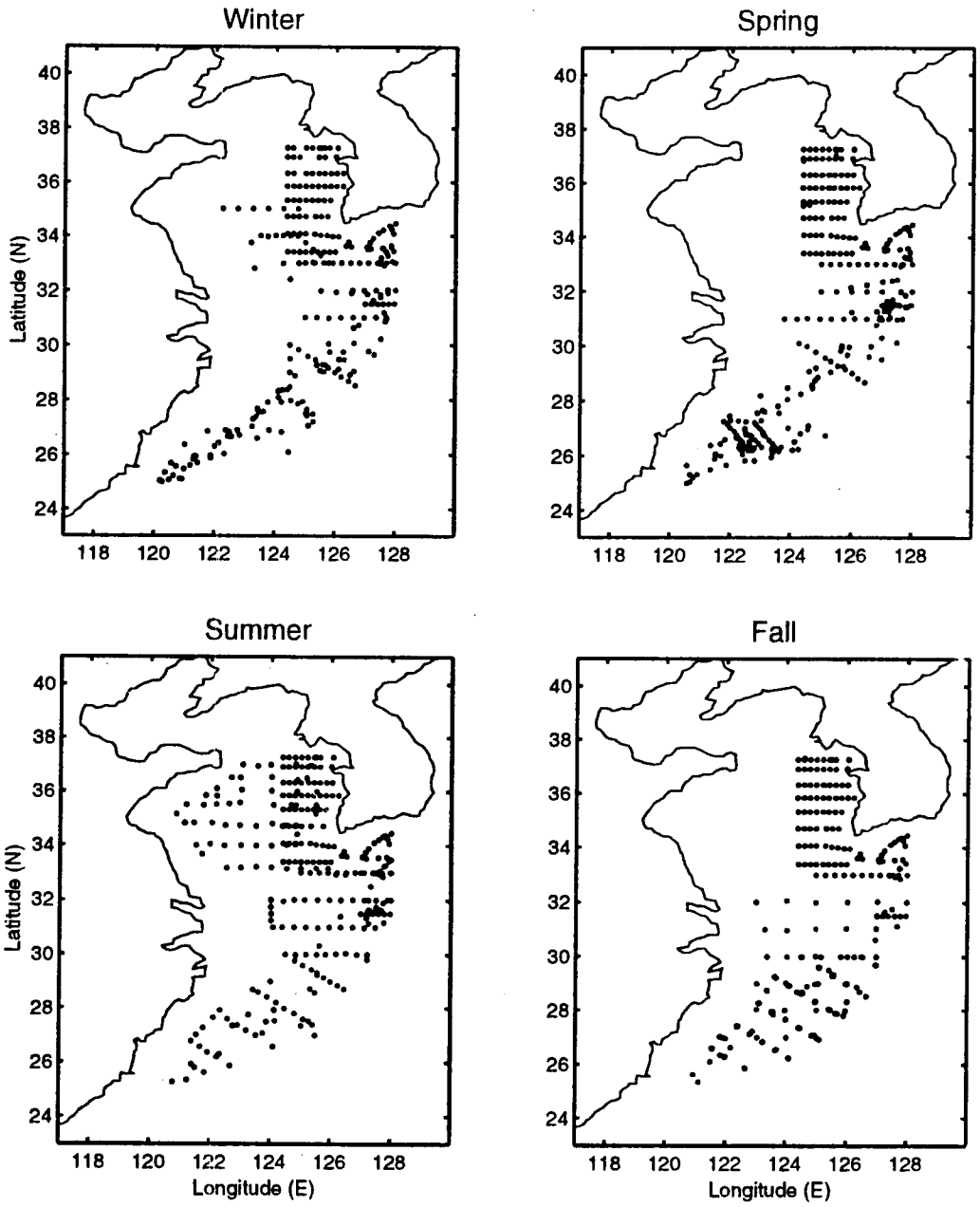

Figure A.11 Seasonal Location of MOODS Temperature Profiles in the Yellow Sea for 1973.

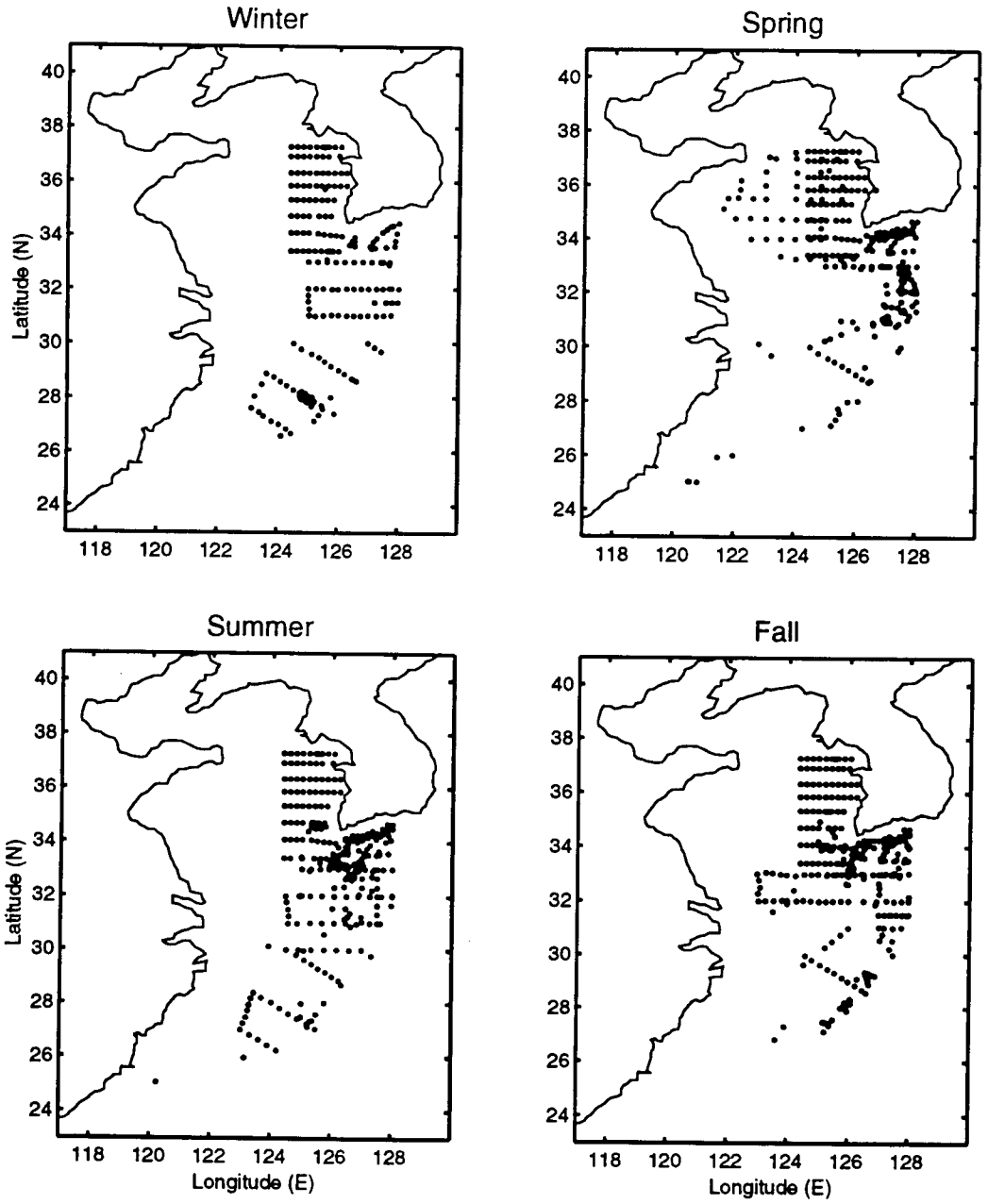

Figure A.12 Seasonal Location of MOODS Temperature Profiles in the Yellow Sea for 1974.

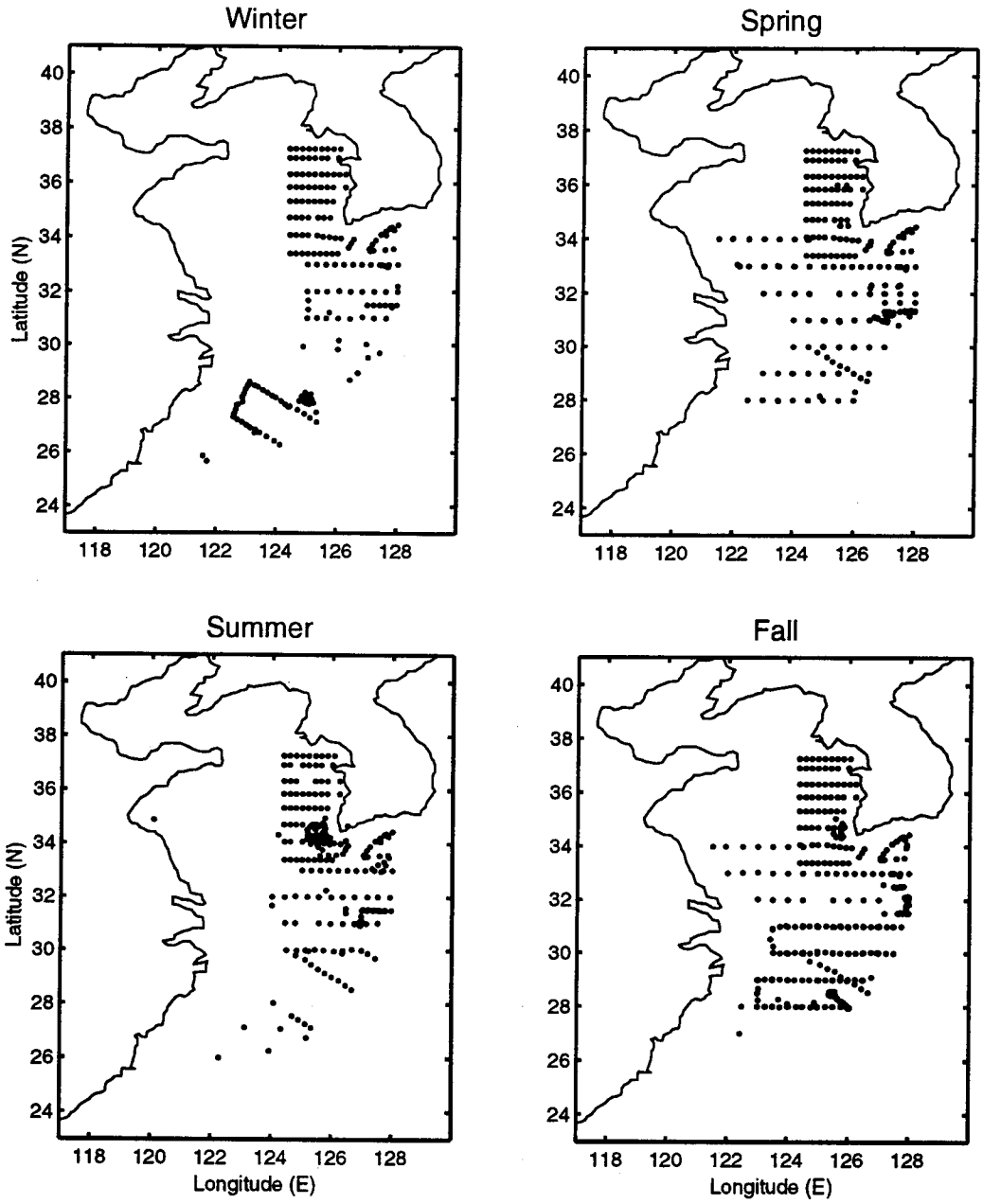

Figure A.13 Seasonal Location of MOODS Temperature Profiles in the Yellow Sea for 1975.

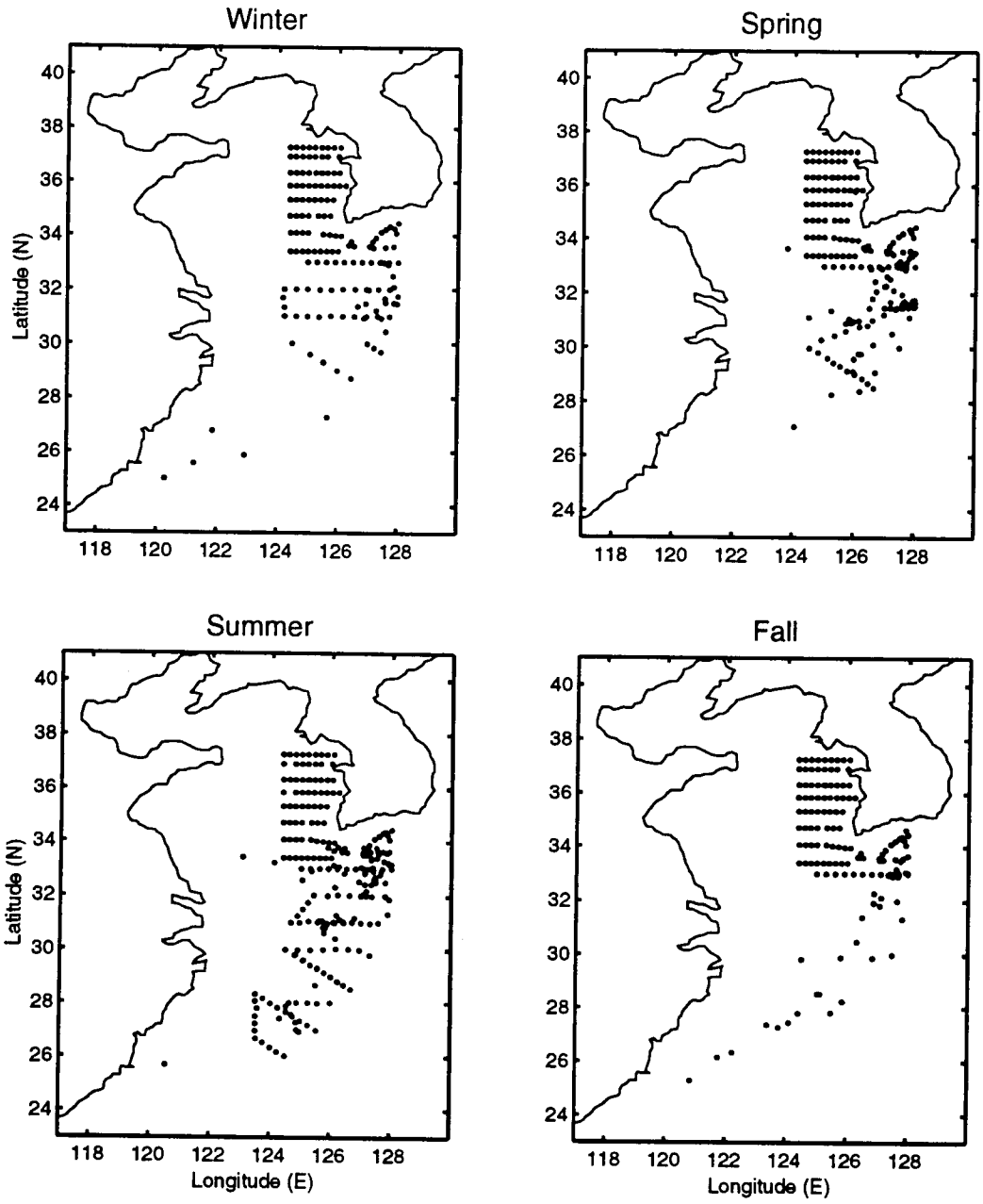

Figure A.14 Seasonal Location of MOODS Temperature Profiles in the Yellow Sea for 1976.

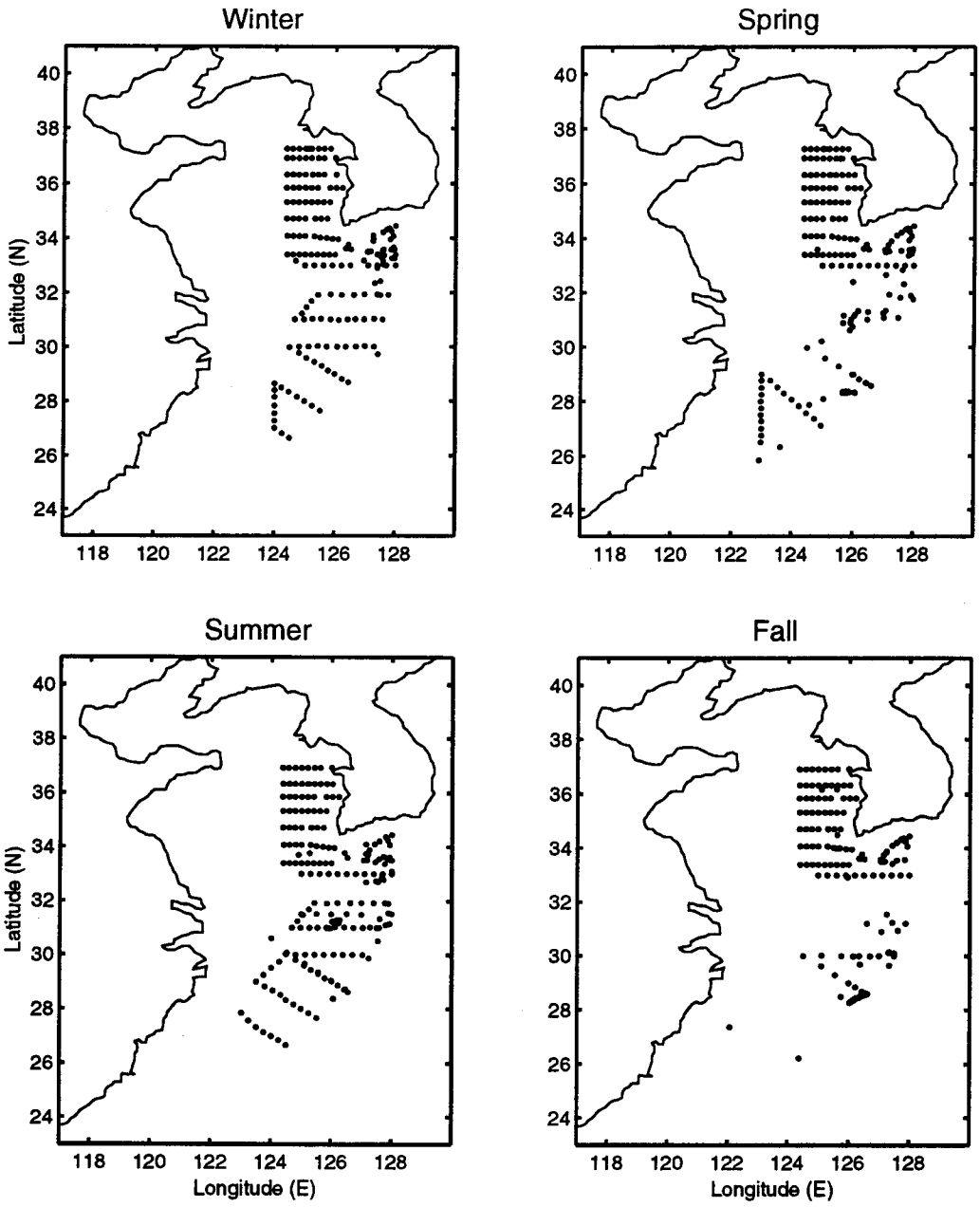

Figure A.15 Seasonal Location of MOODS Temperature Profiles in the Yellow Sea for 1977.

APPENDIX B TEMPORAL DISTRIBUTION OF MOODS TEMPERATURE PROFILES FROM 1963 TO 1977

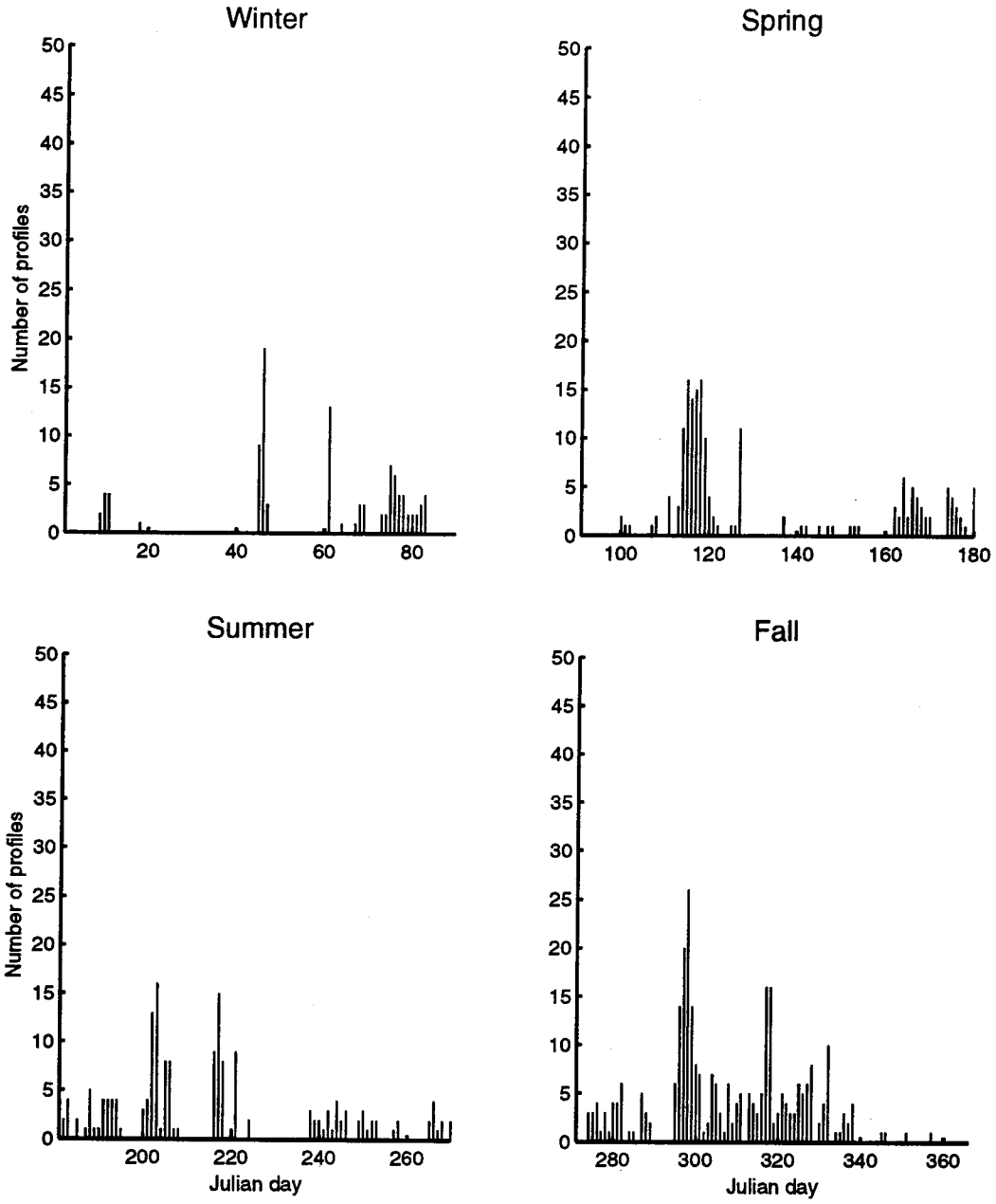

Figure B.1 The Number of MOODS Temperature Profiles During 1963 in the Yellow Sea.

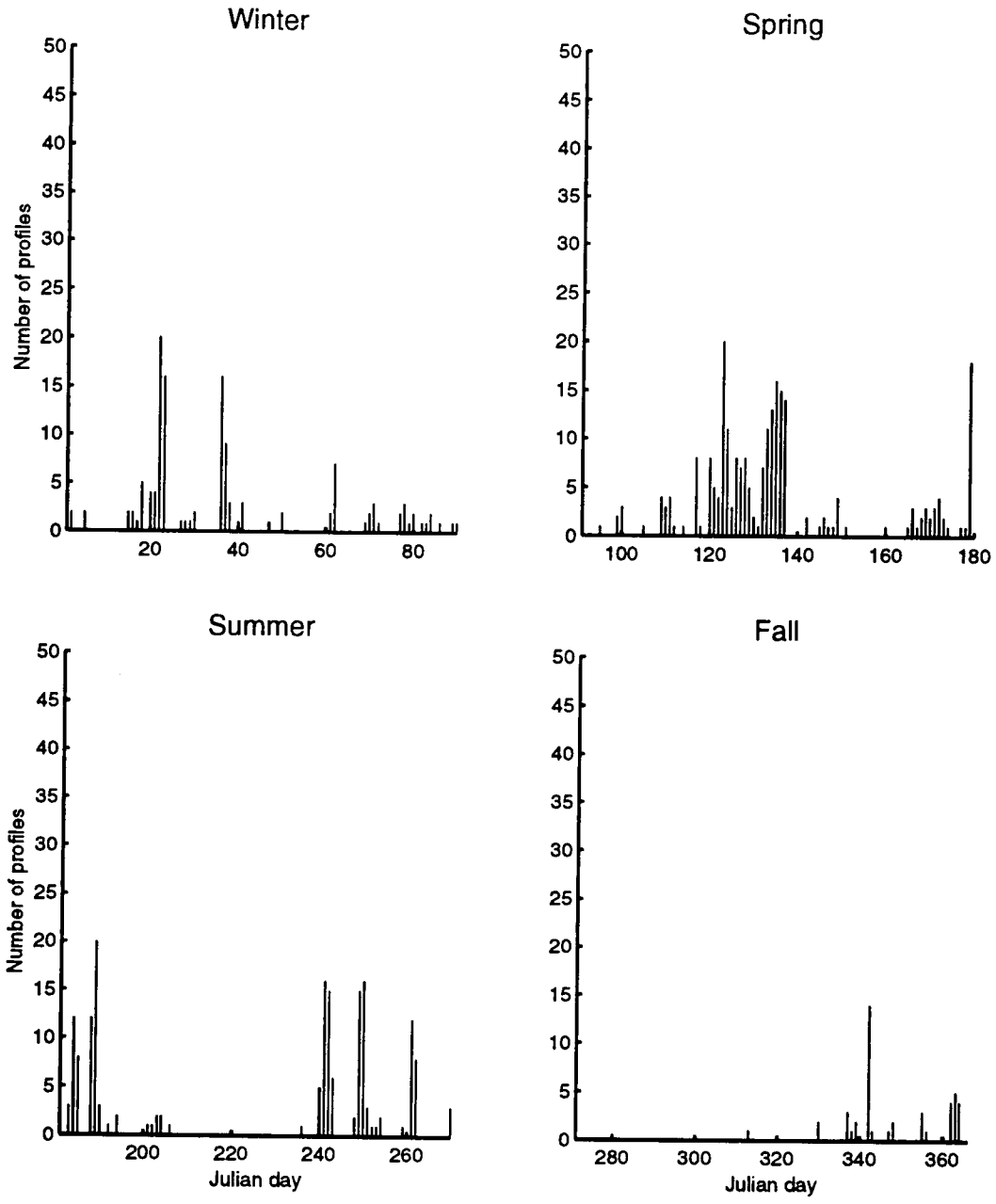

Figure B.2 The Number of MOODS Temperature Profiles During 1964 in the Yellow Sea.

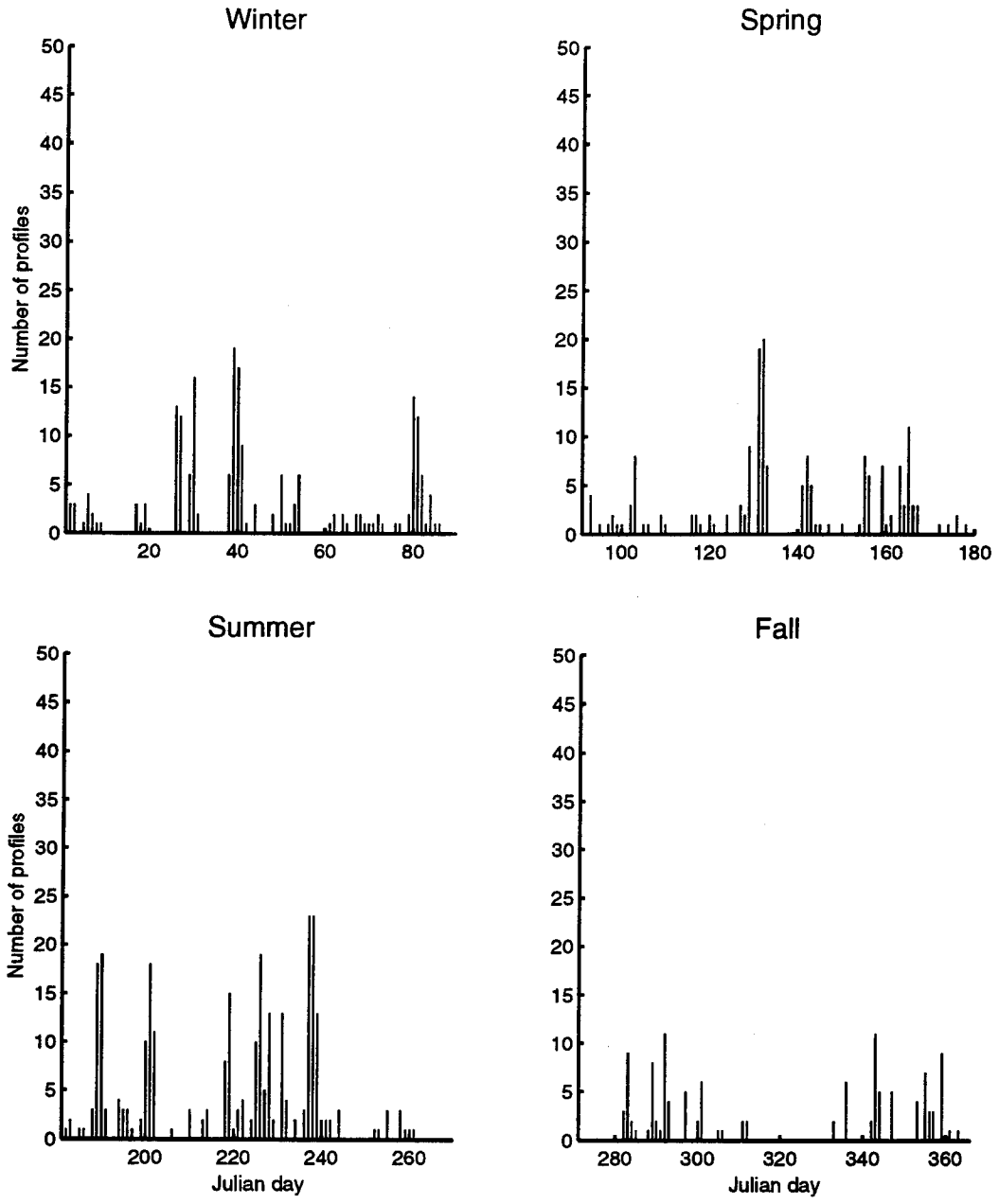

Figure B.3 The Number of MOODS Temperature Profiles During 1965 in the Yellow Sea.

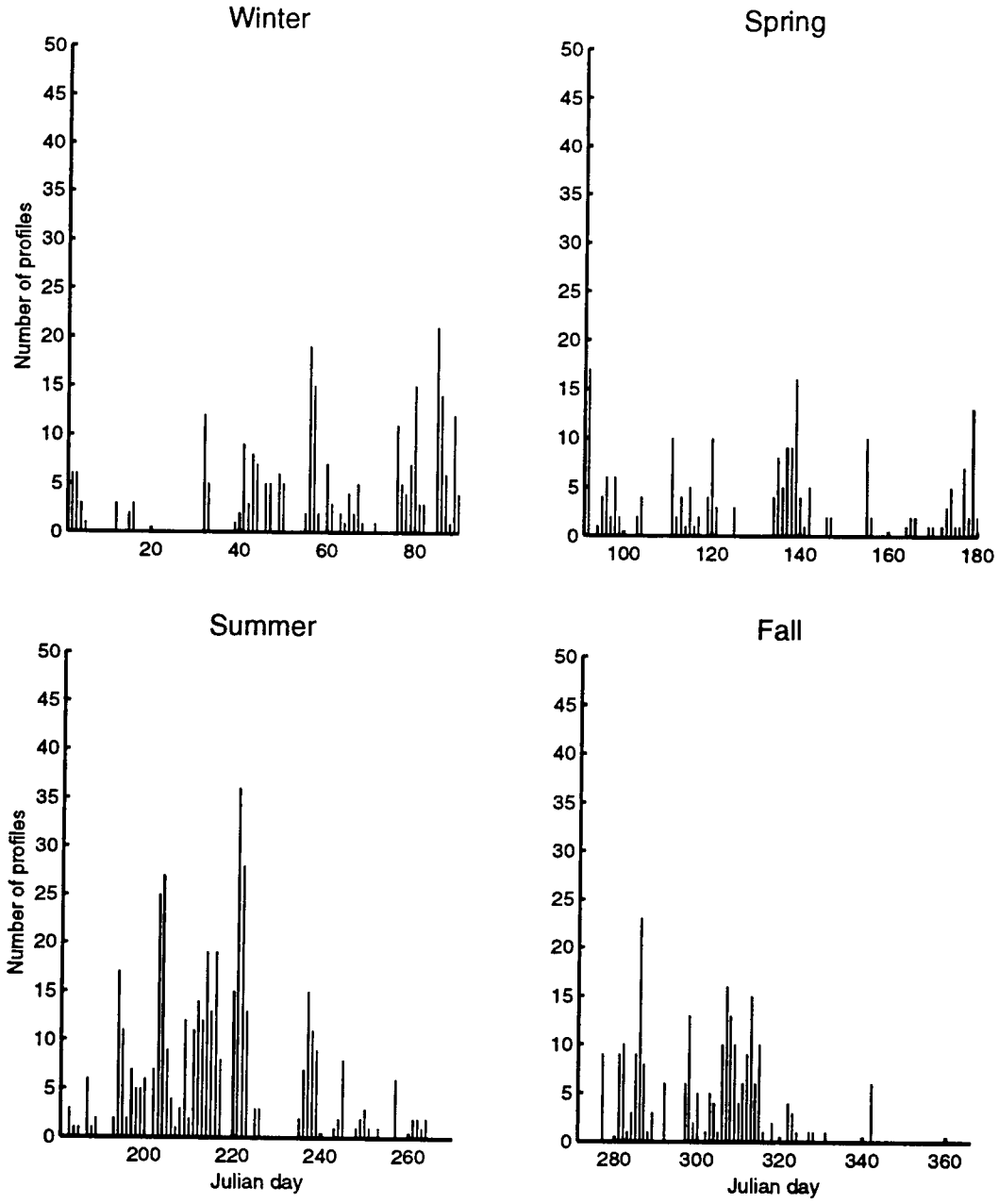

Figure B.4 The Number of MOODS Temperature Profiles During 1966 in the Yellow Sea.

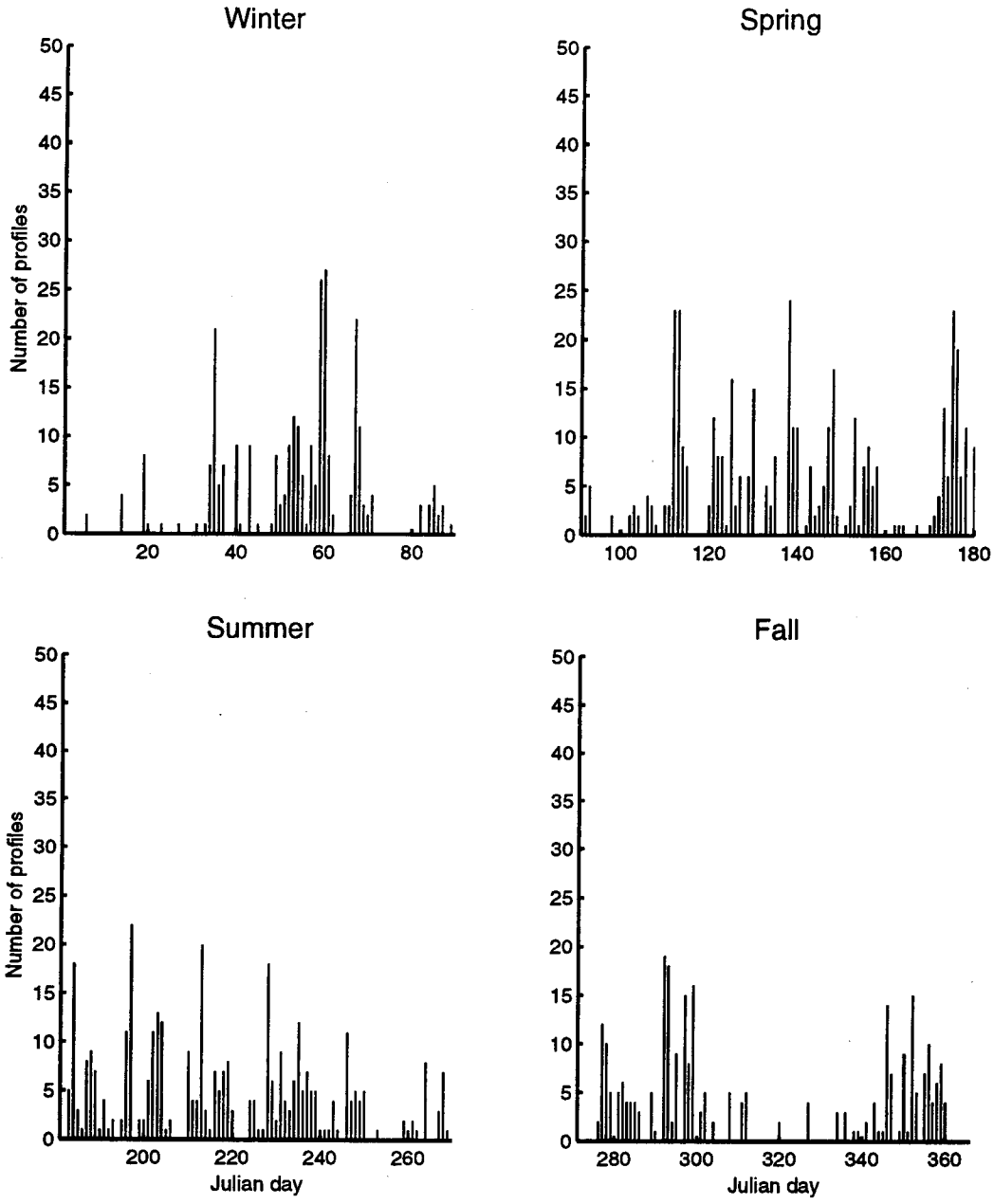

Figure B.5 The Number of MOODS Temperature Profiles During 1967 in the Yellow Sea.

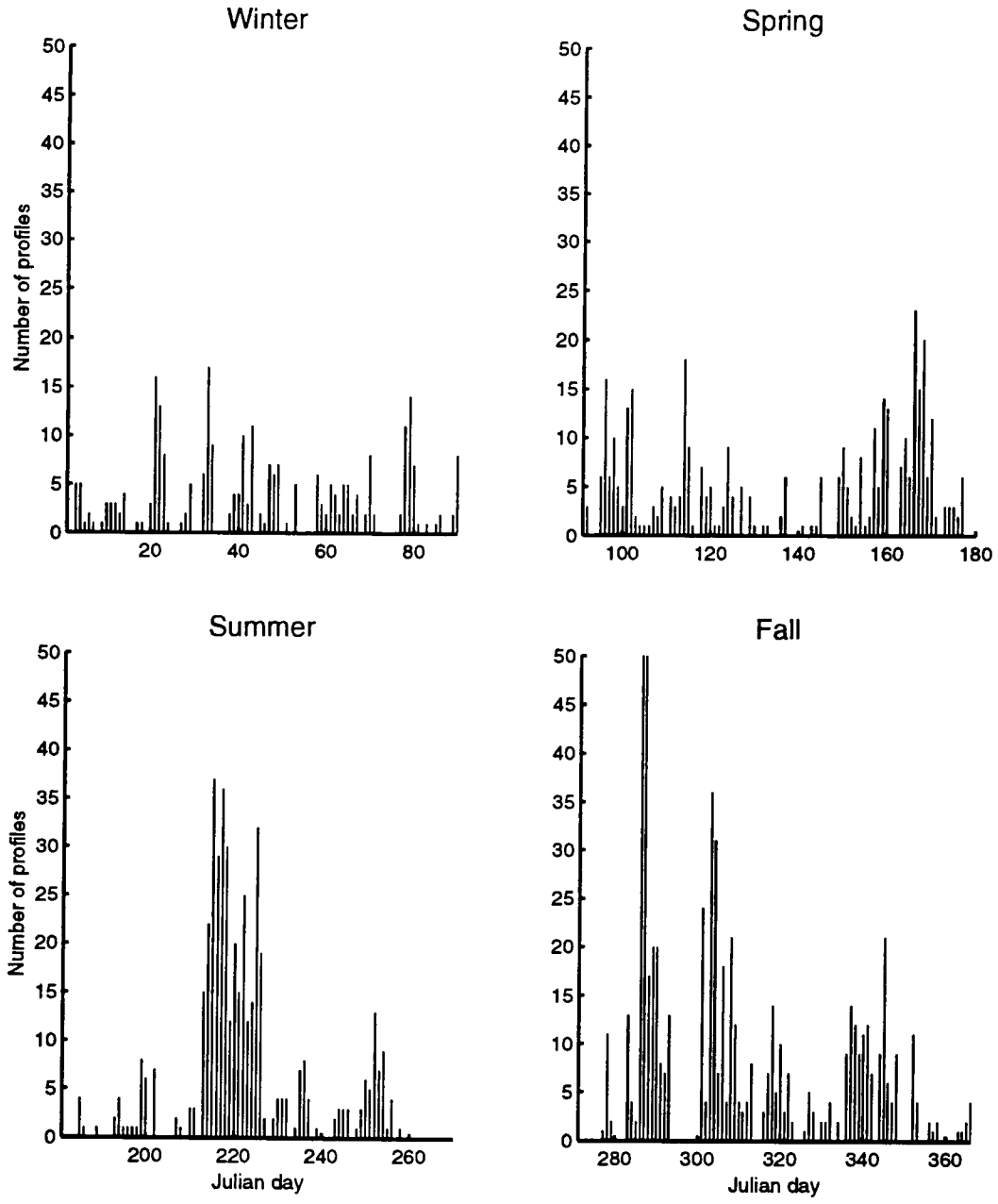

Figure B.6 The Number of MOODS Temperature Profiles During 1968 in the Yellow Sea.

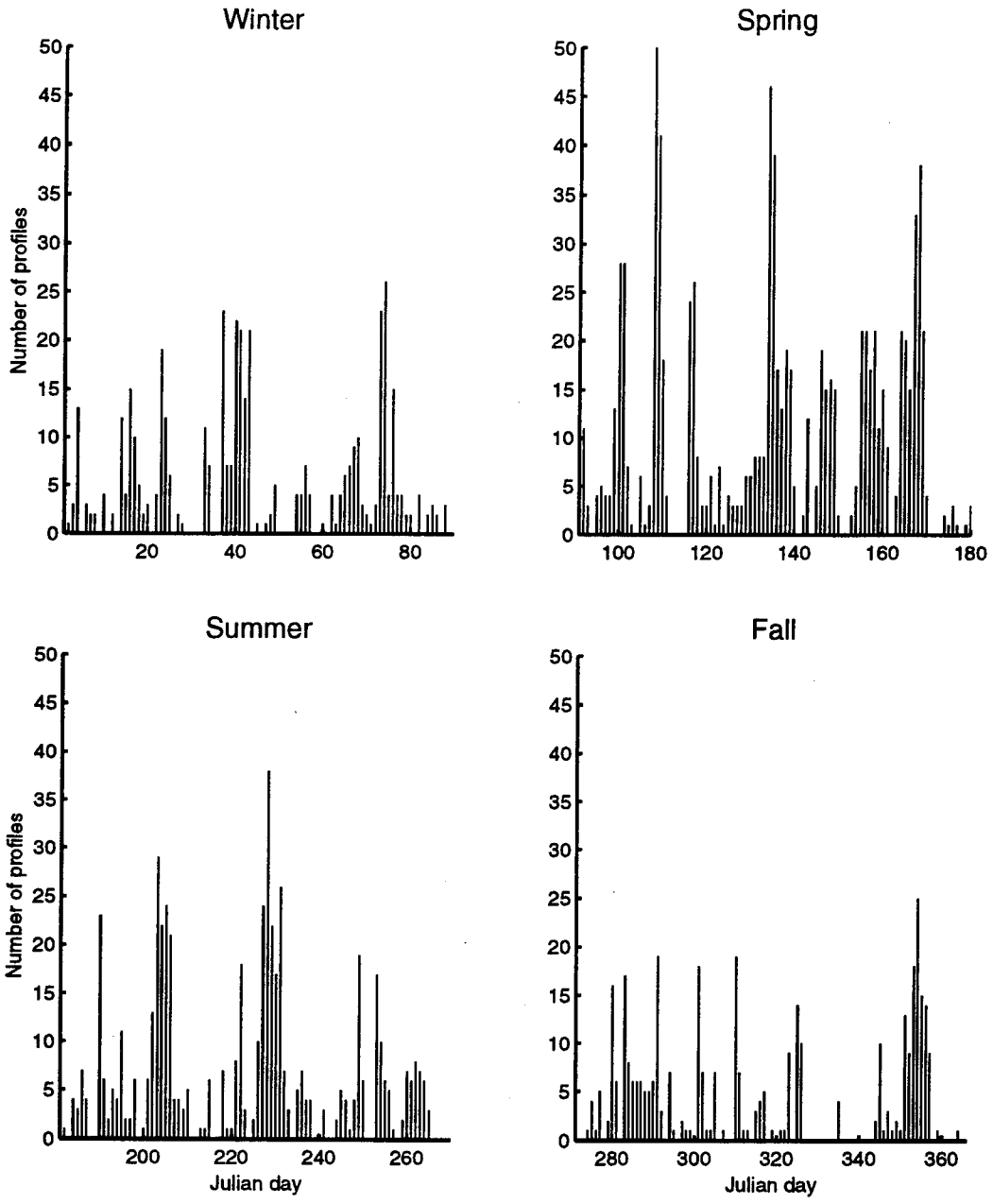

Figure B.7 The Number of MOODS Temperature Profiles During 1969 in the Yellow Sea.

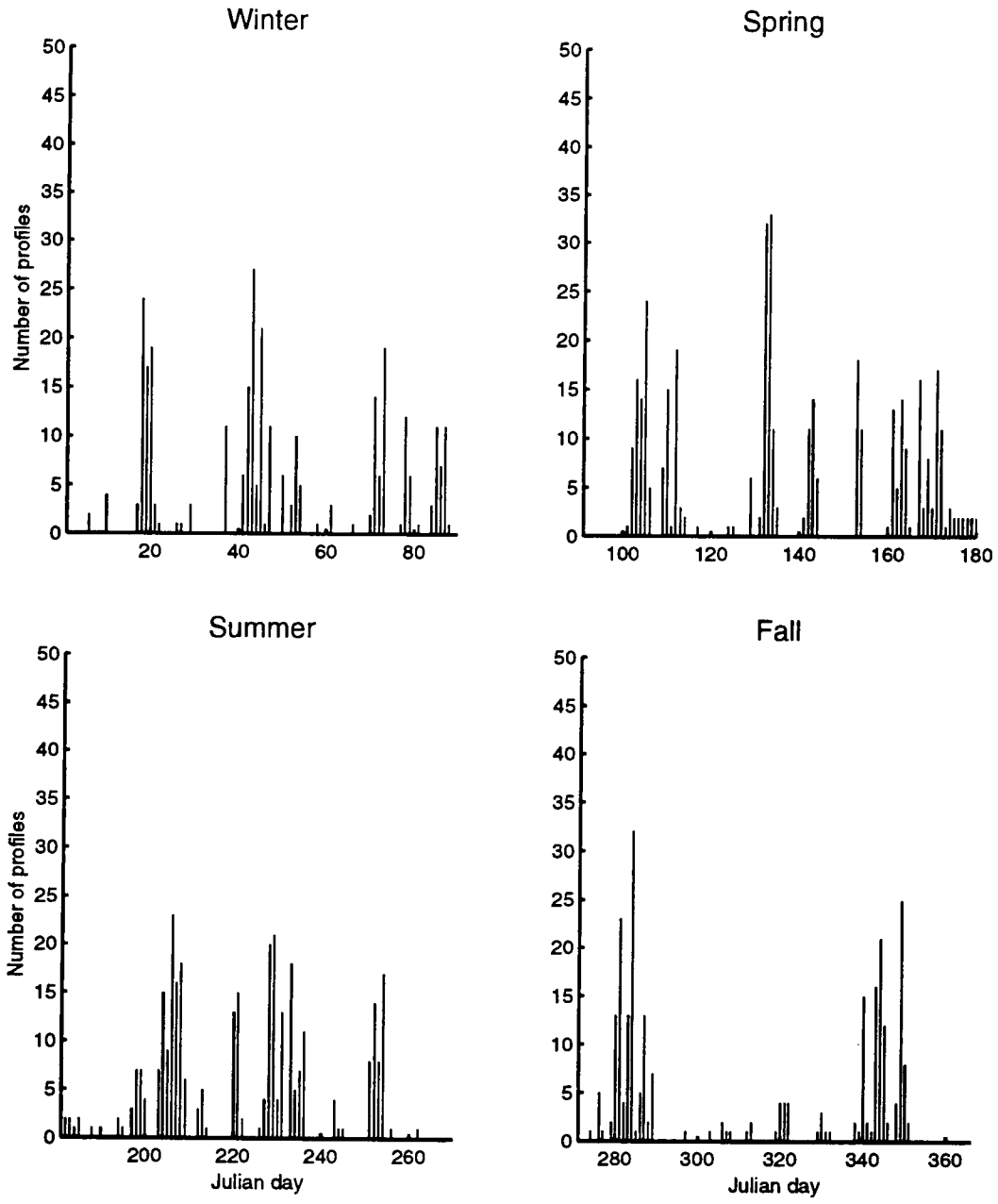

Figure B.8 The Number of MOODS Temperature Profiles During 1970 in the Yellow Sea.

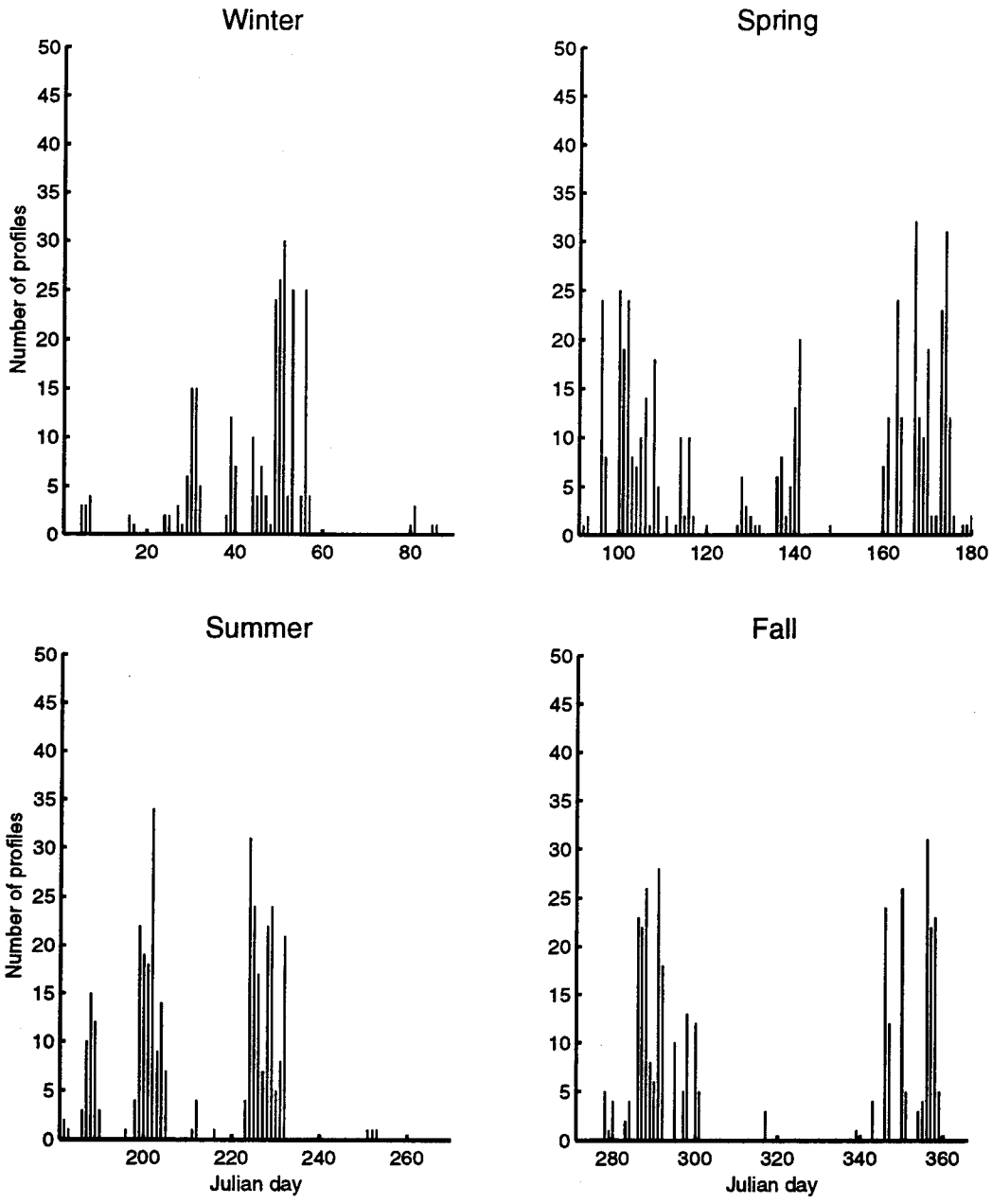

Figure B.9 The Number of MOODS Temperature Profiles During 1971 in the Yellow Sea.

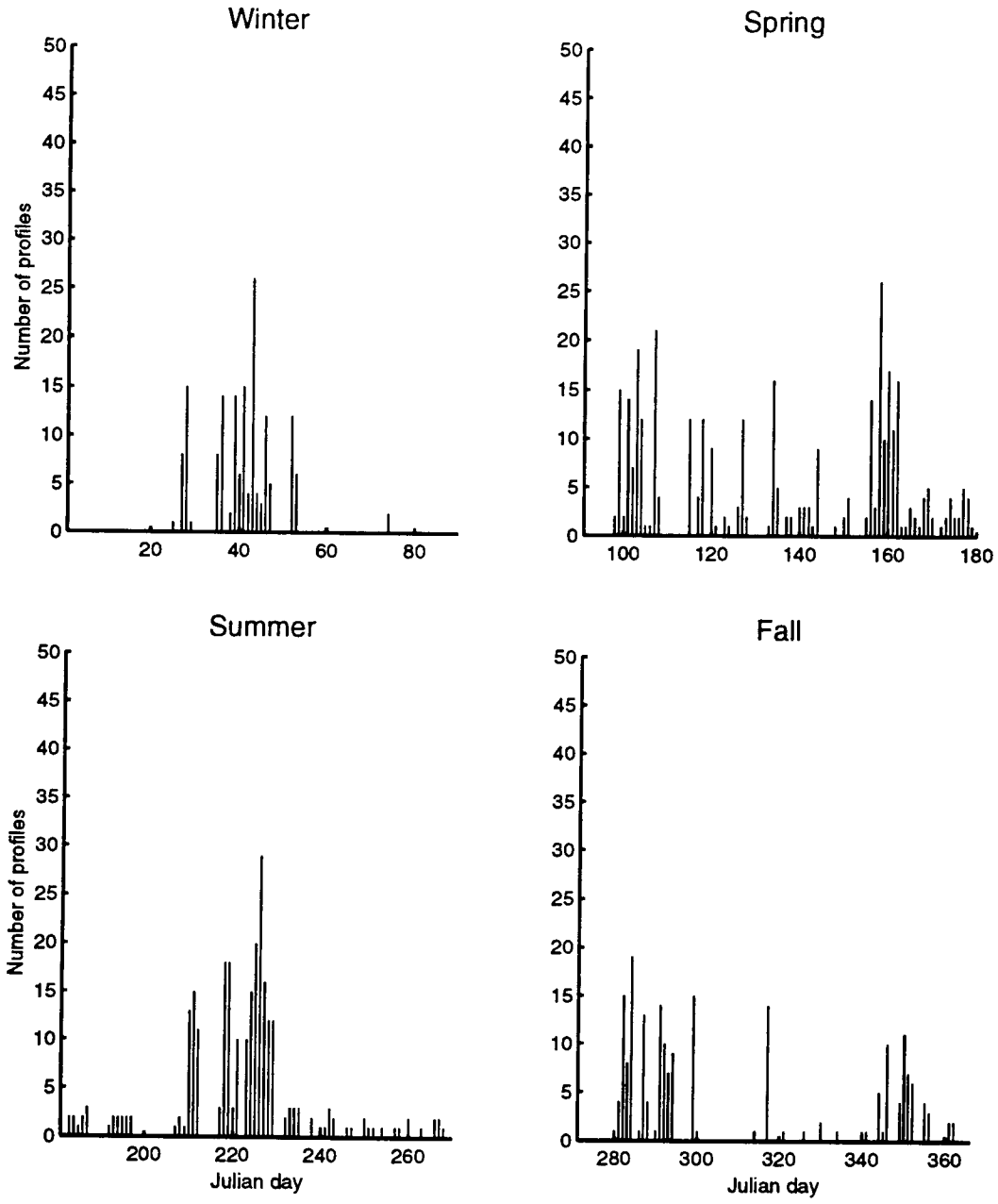

Figure B.10 The Number of MOODS Temperature Profiles During 1972 in the Yellow Sea.

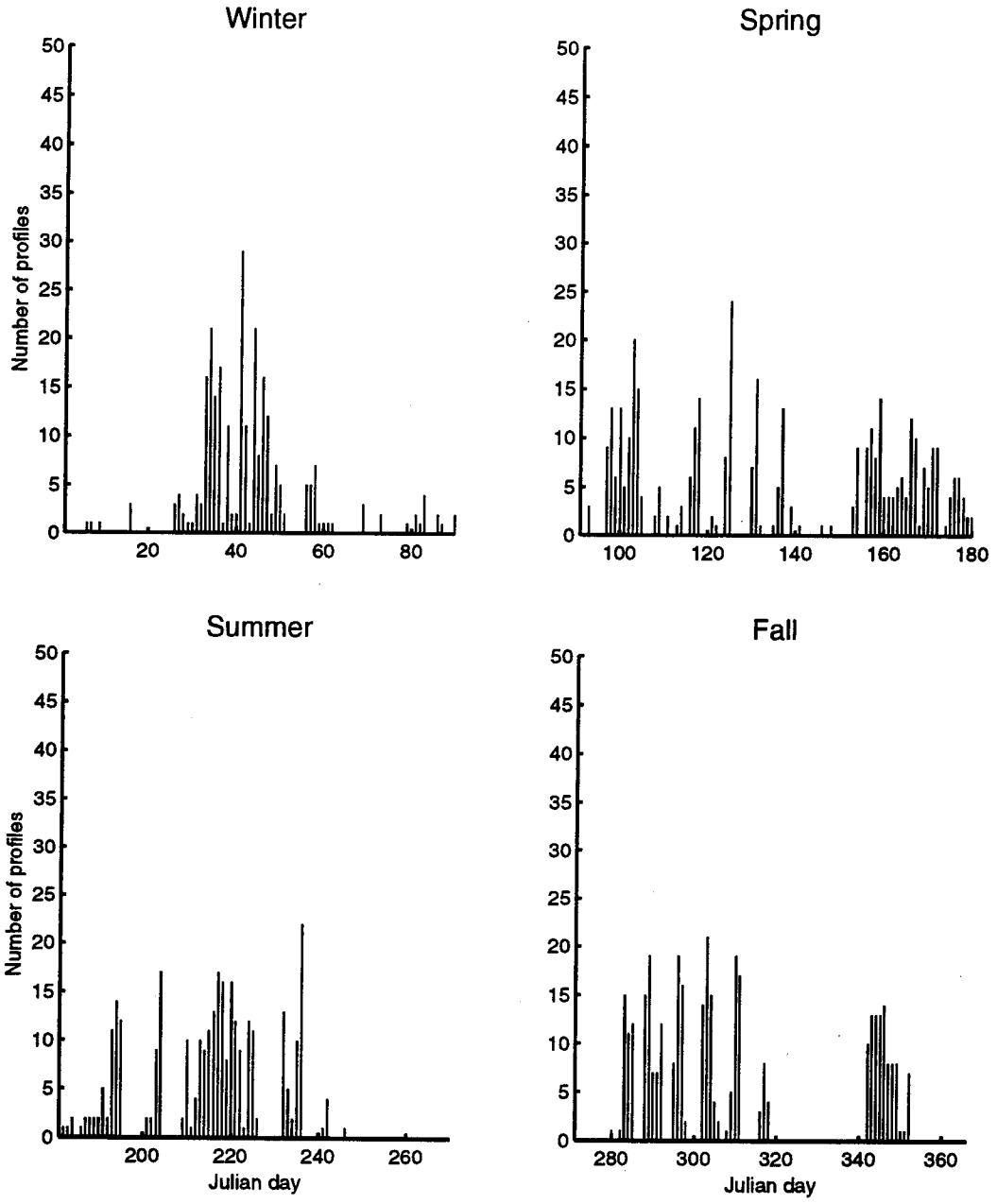

Figure B.11 The Number of MOODS Temperature Profiles During 1973 in the Yellow Sea.

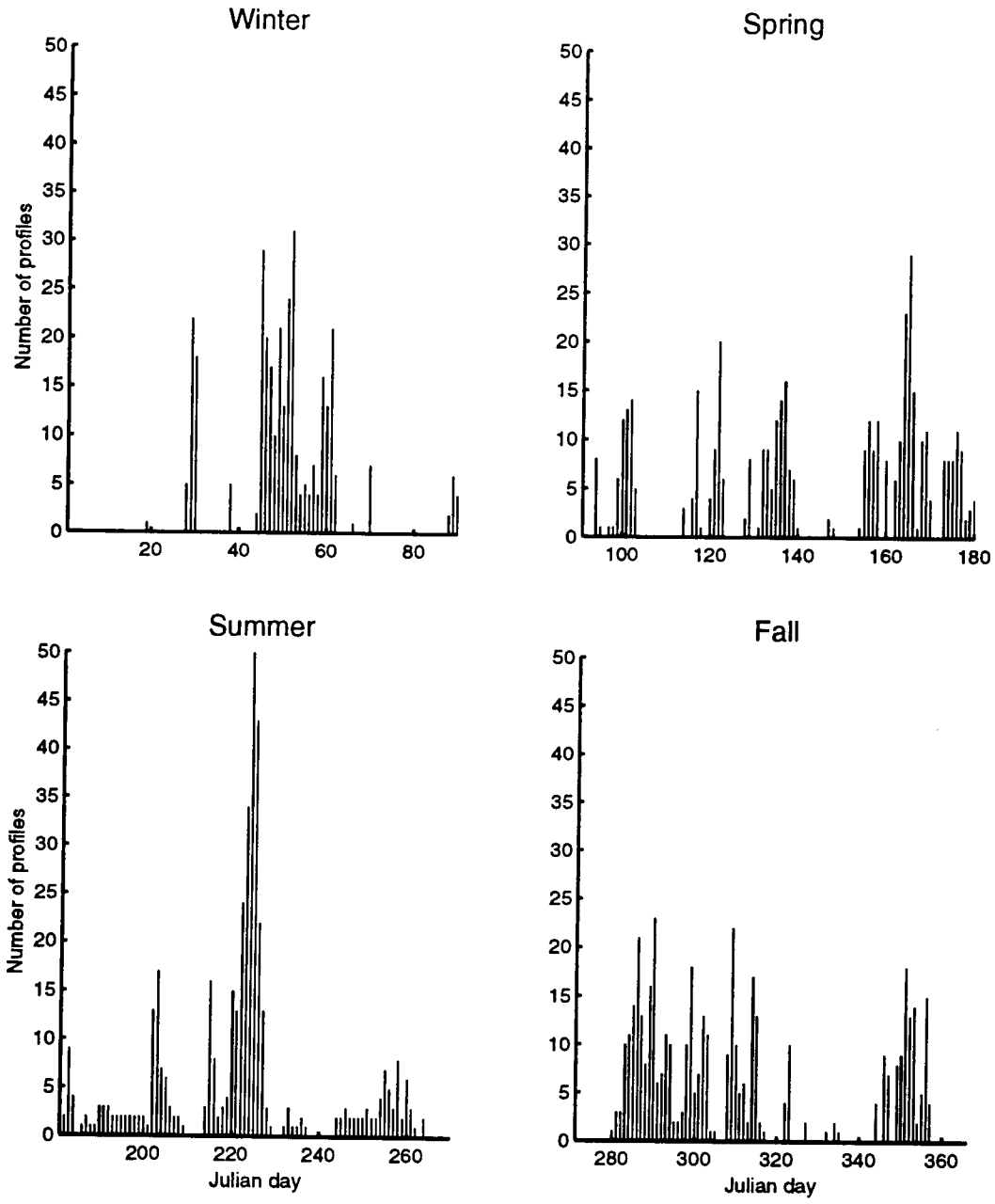

Figure B.12 The Number of MOODS Temperature Profiles During 1974 in the Yellow Sea.

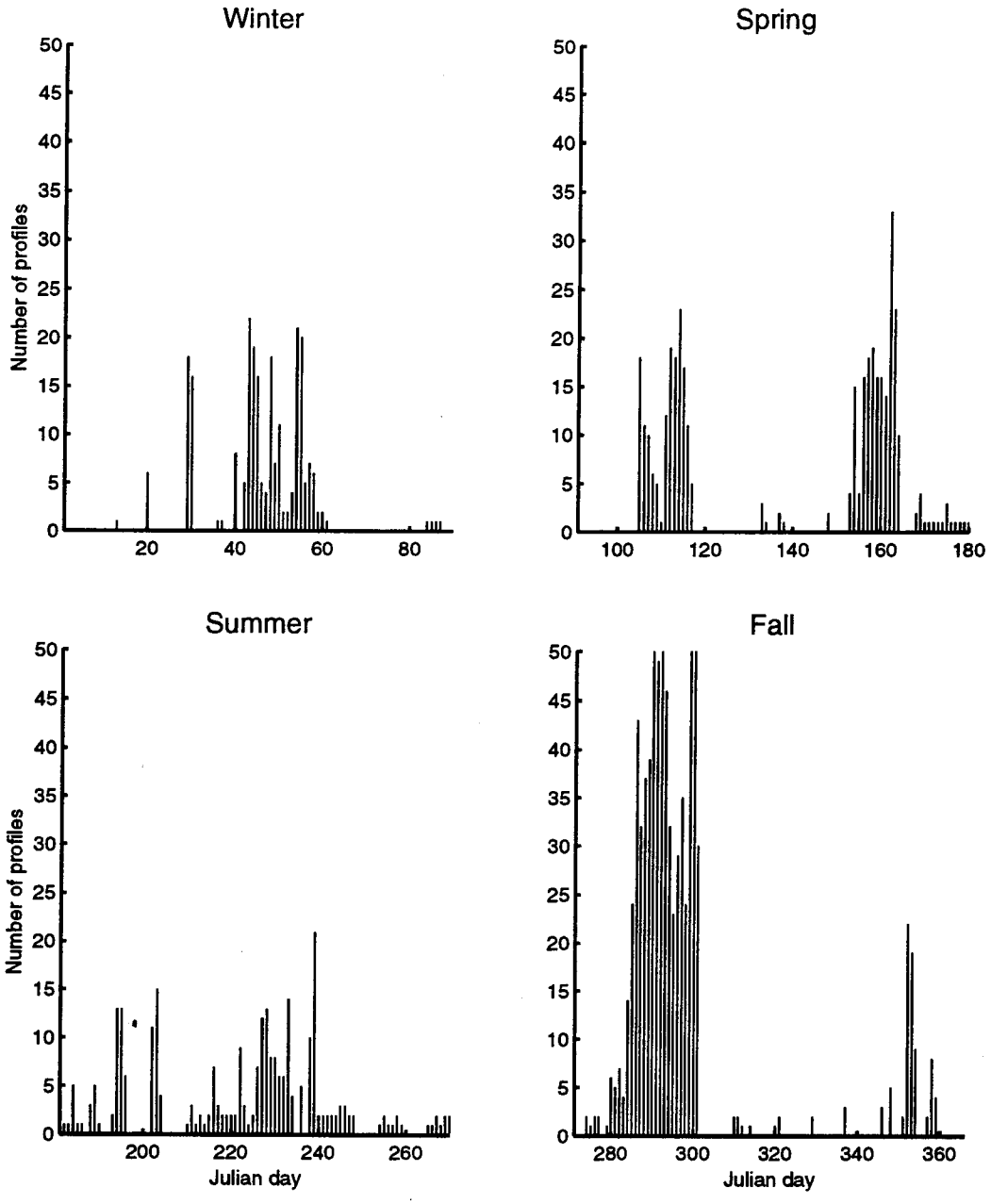

Figure B.13 The Number of MOODS Temperature Profiles During 1975 in the Yellow Sea.

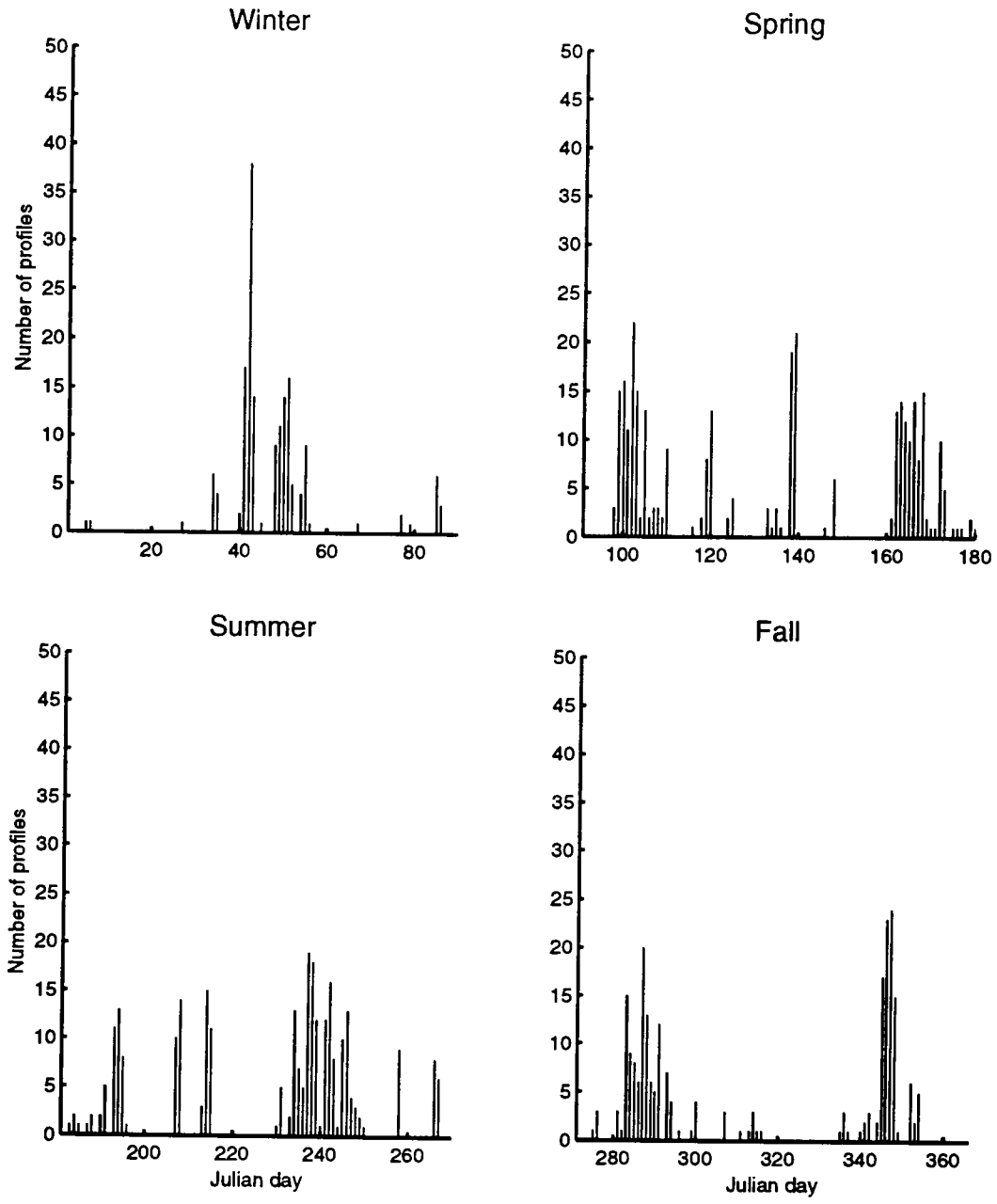

Figure B.14 The Number of MOODS Temperature Profiles During 1976 in the Yellow Sea.

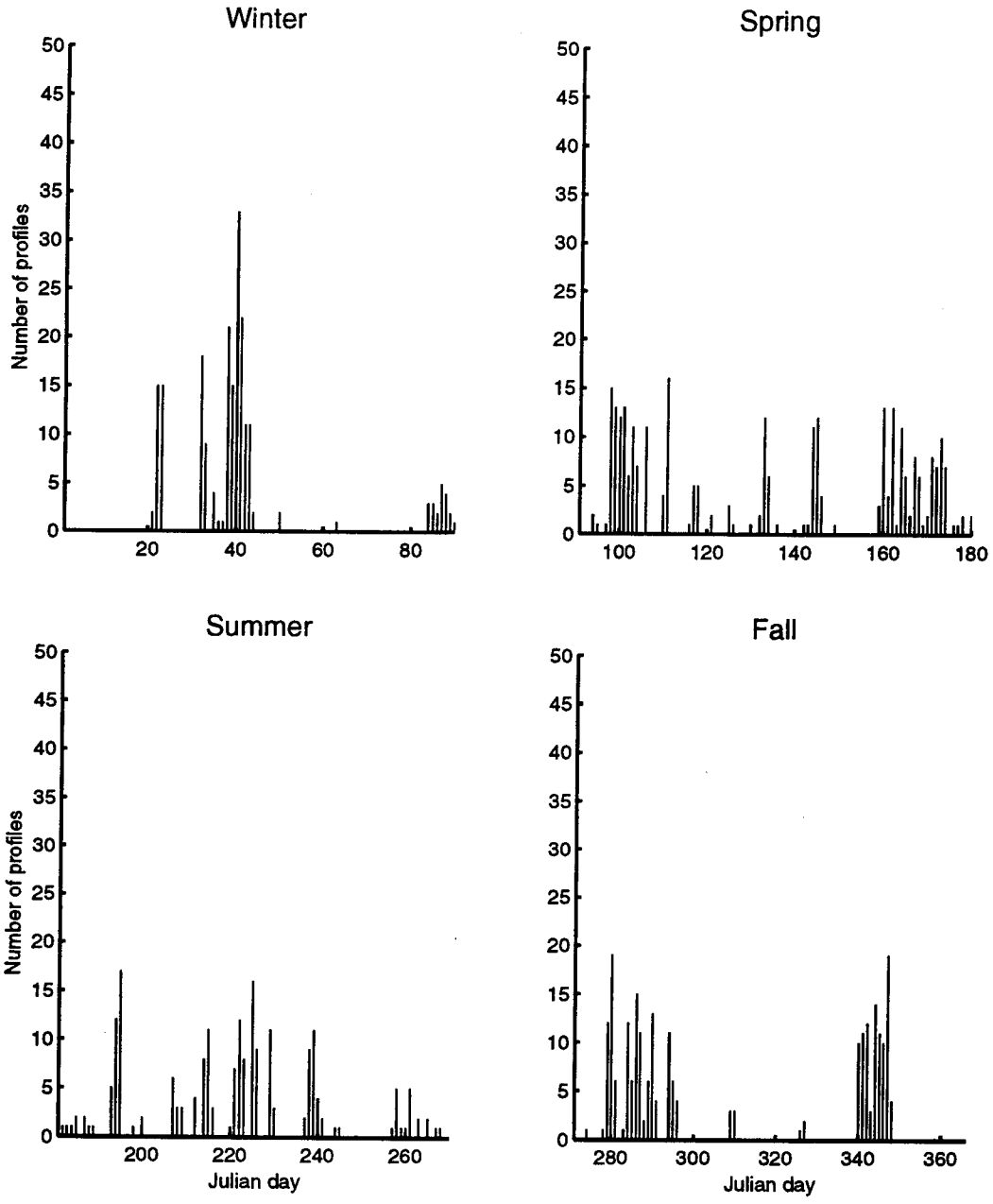

Figure B.15 The Number of MOODS Temperature Profiles During 1977 in the Yellow Sea.

APPENDIX C YELLOW SEA SEASONAL MEAN TEMPERATURE FIELDS

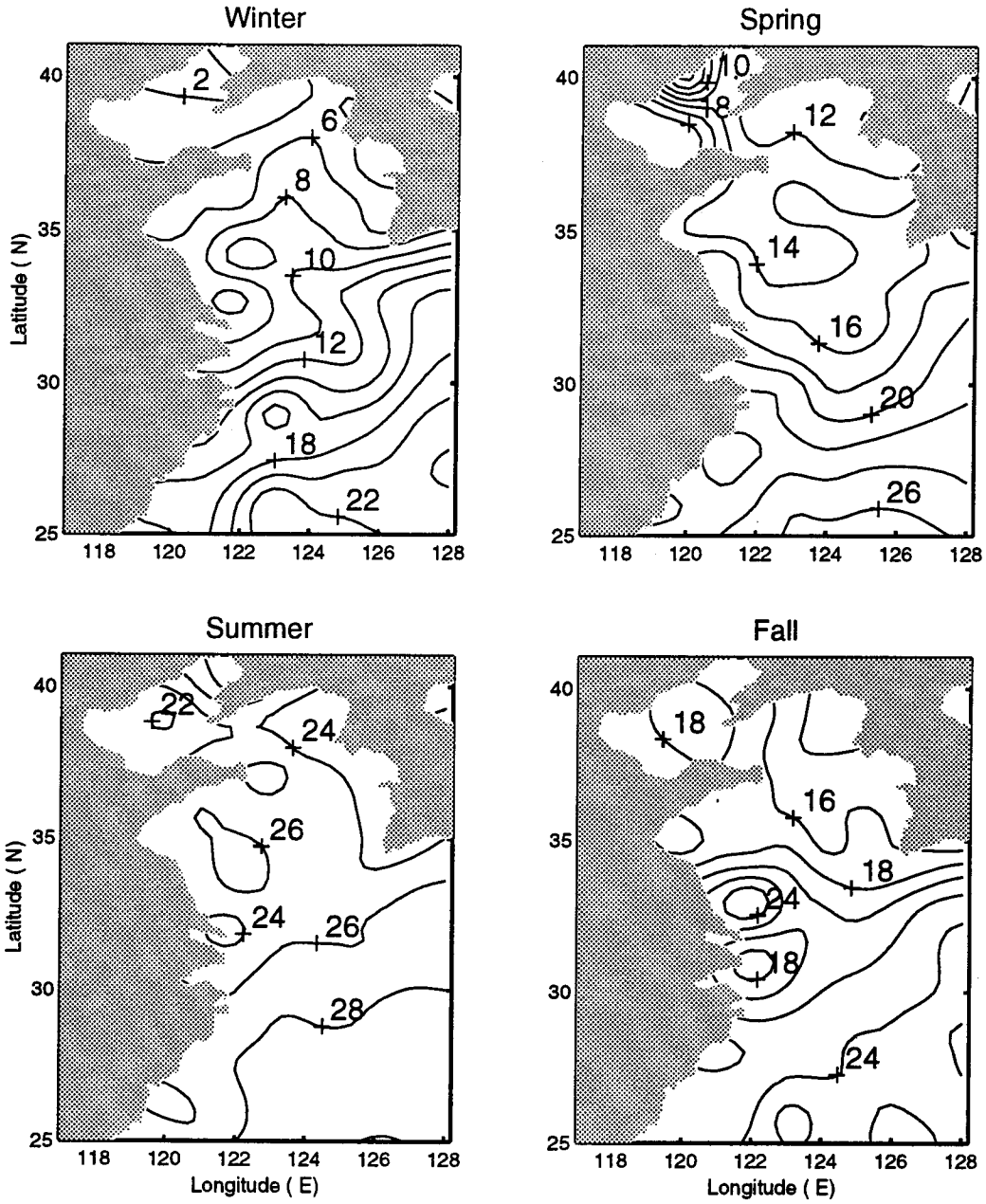

Figure C.1 Yellow Sea Seasonal Mean Temperature Field for the Surface on a 20 Minute Grid. Data were Obtained from the MOODS Temperature Data Base for the Years 1929 to 1991.

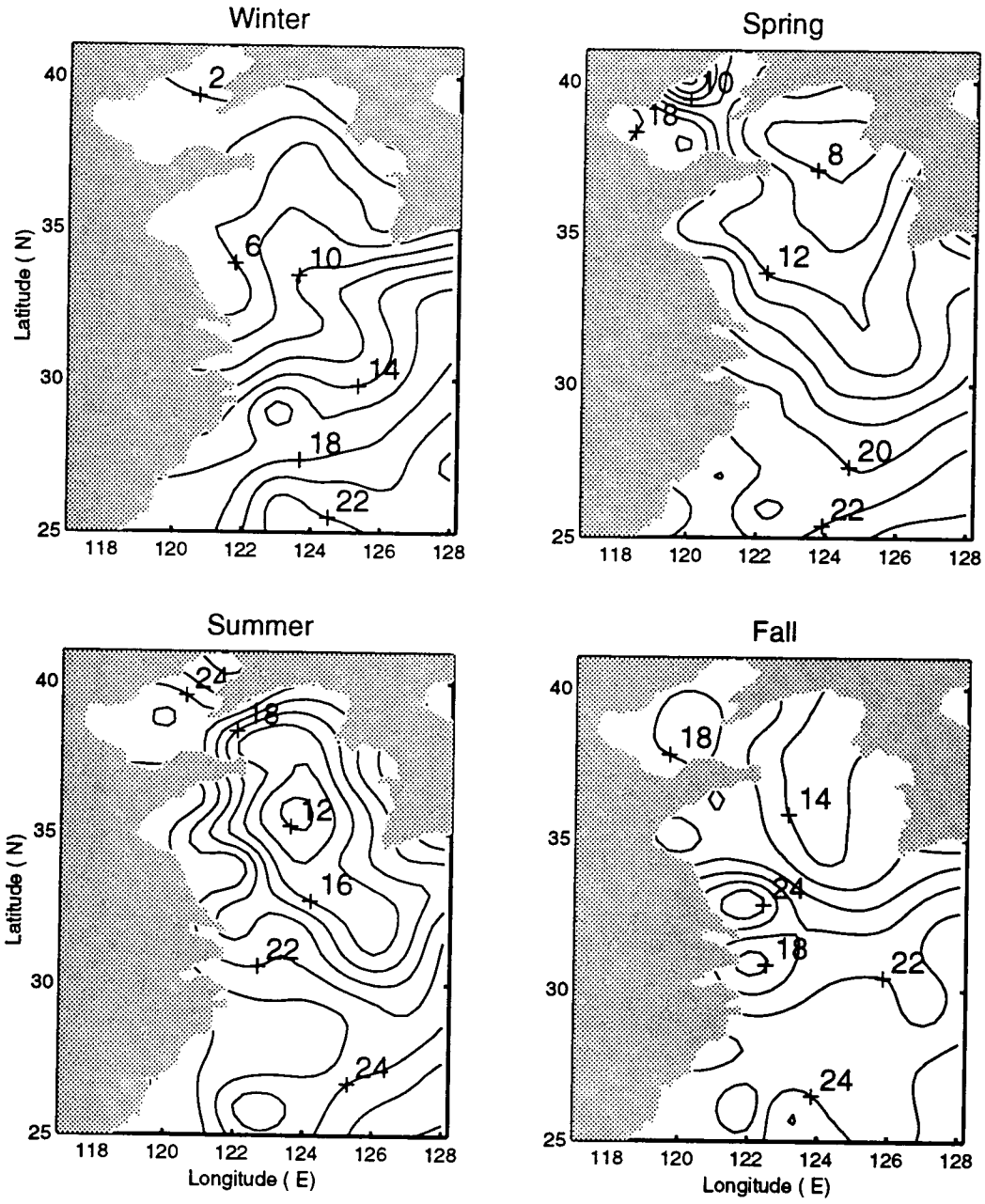

Figure C.2 Yellow Sea Seasonal Mean Temperature Field for 50% Water Depth on a 20 Minute Grid. Data were Obtained from the MOODS Temperature Data Base for the Years 1929 to 1991.

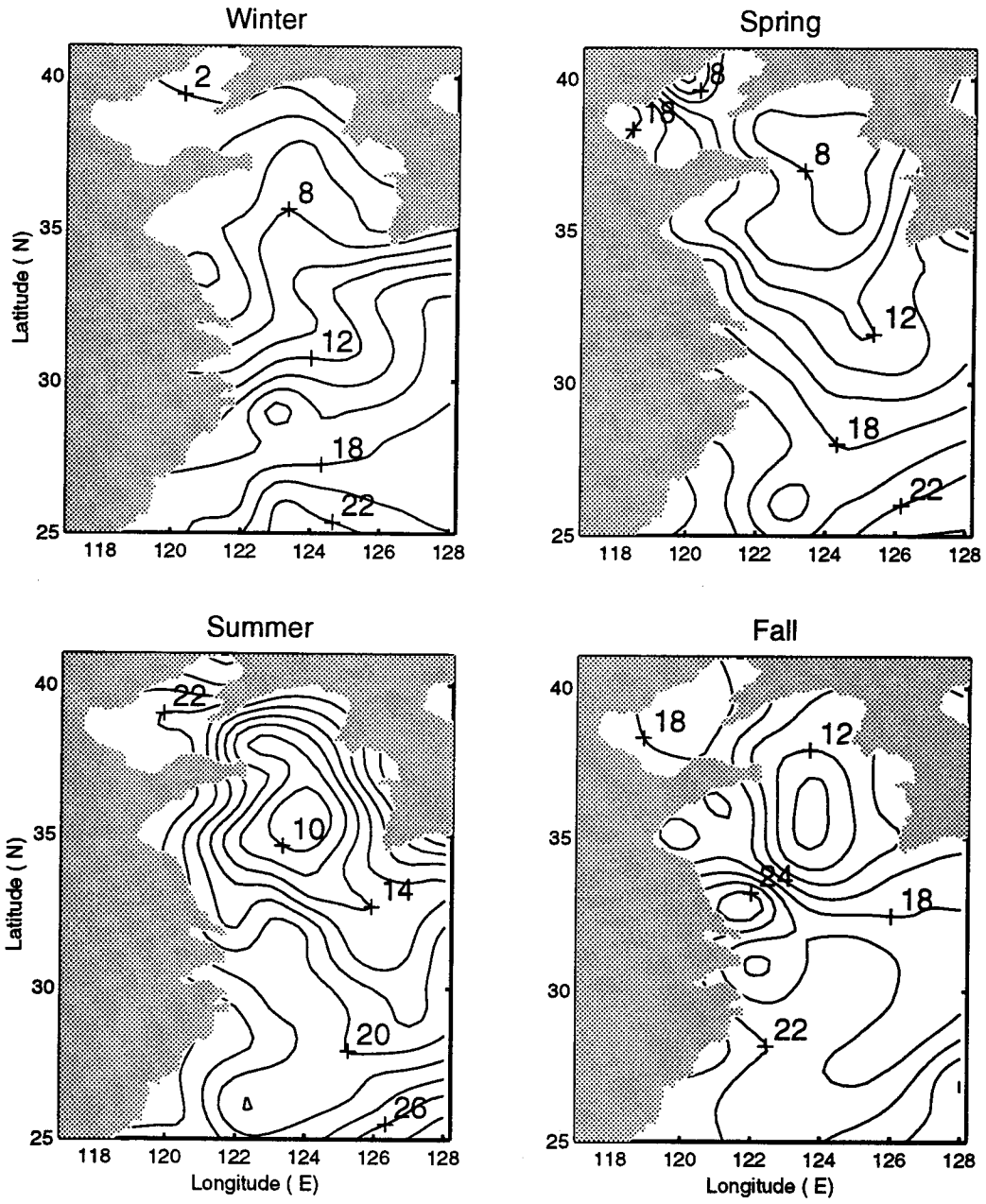

Figure C.3 Yellow Sea Seasonal Mean Temperature Field for 80% Water Depth on a 20 Minute Grid. Data were Obtained from the MOODS Temperature Data Base for the Years 1929 to 1991.

APPENDIX D AUTOCORRELATION FUNCTIONS

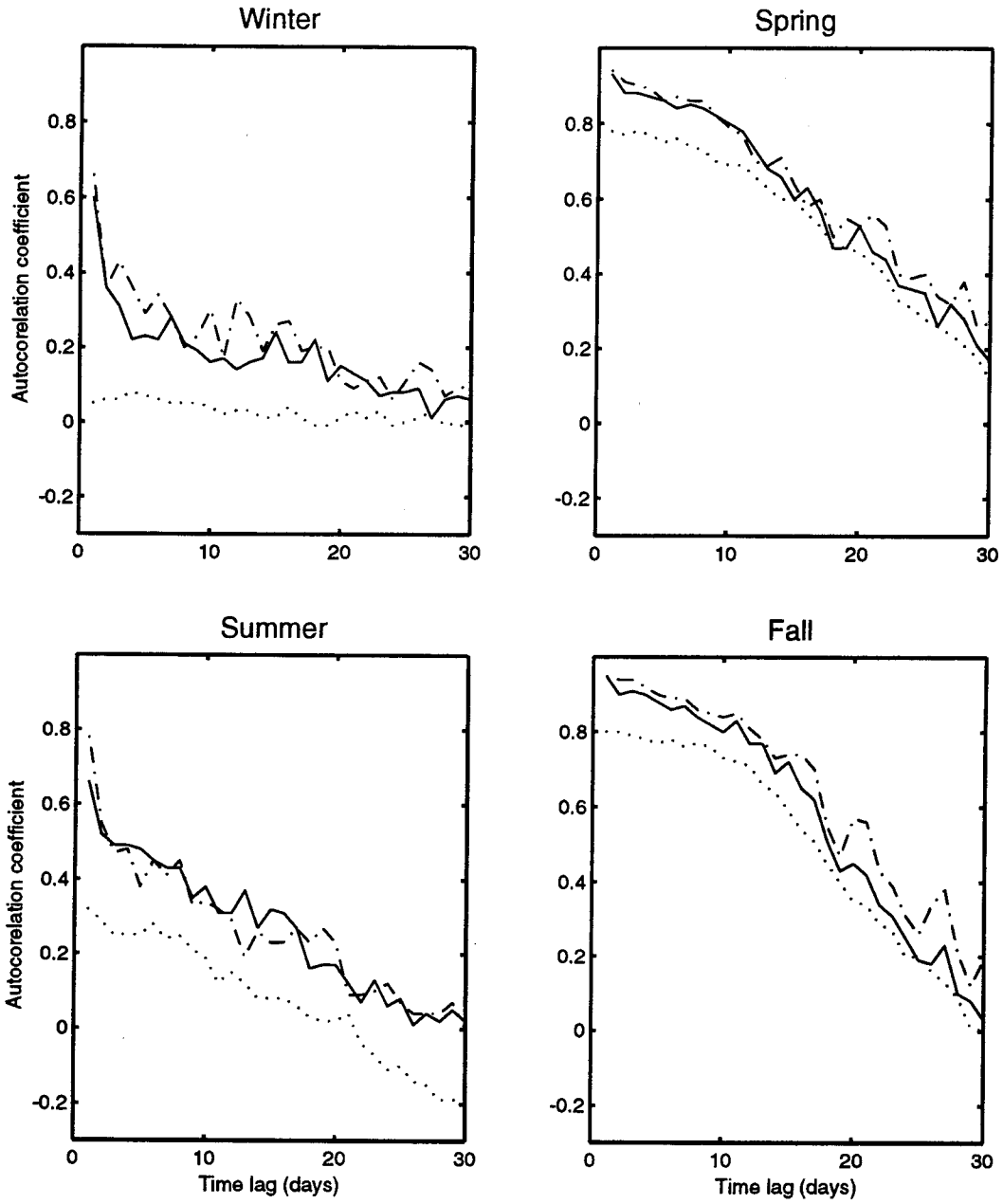

Figure D.1 Temporal Variations of Autocorrelation Function $\eta\,(m, n)$ for Type II Data at the Surface.The Three Curves on Each Graph are the Dependency of $\eta\,(m, n)$ on Time Lag $n\Delta t$ for $m = 0$ (no lag, dash-dot), $m = 1$ (10 km lag, solid), and $m = 15$ (150 km lag, dots). Data were Obtained from the MOODS Temperature Data Base for the Years 1929 to 1991.

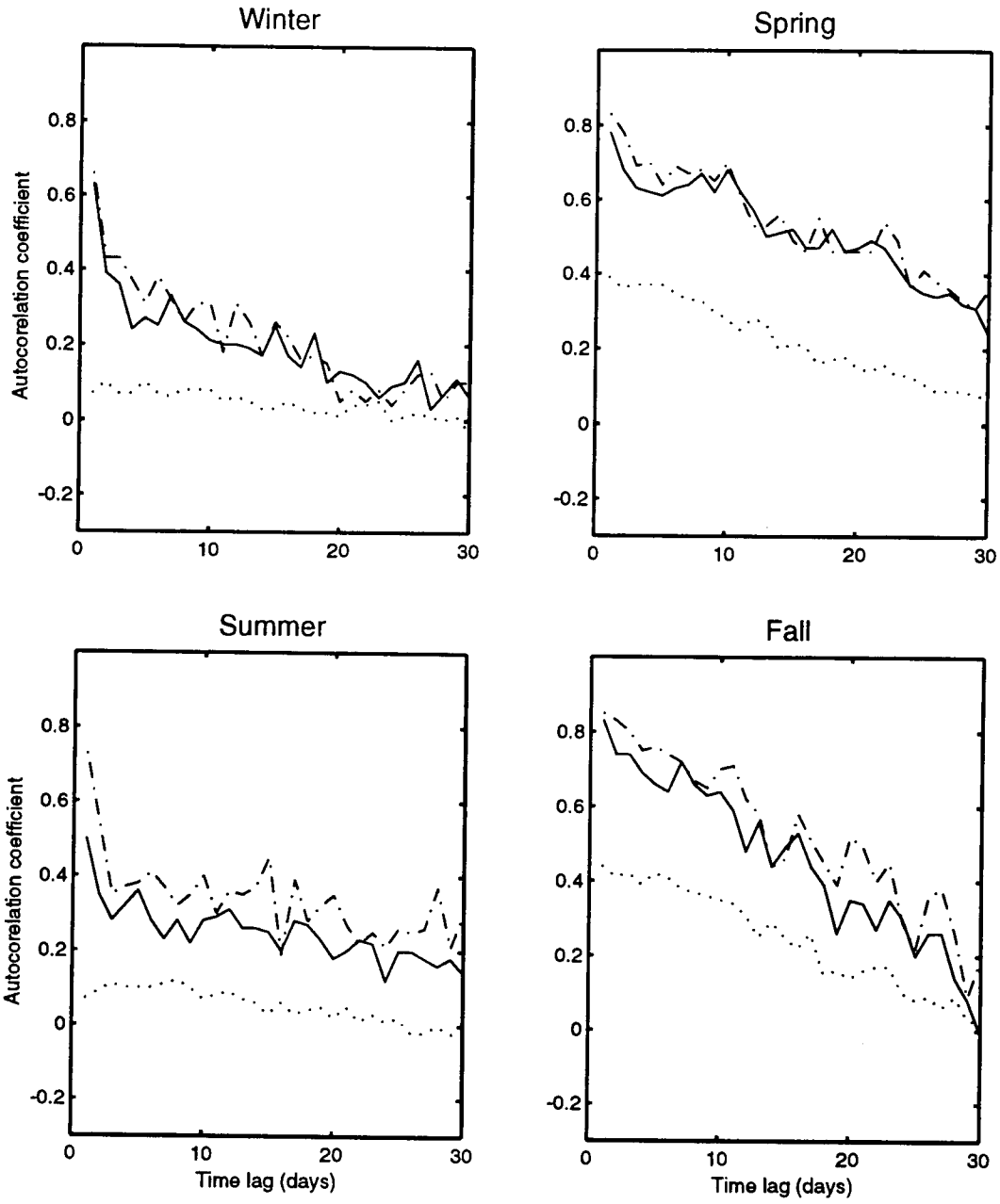

Figure D.2 Temporal Variations of Autocorrelation Function $\eta\,(m, n)$ for Type II Data at 50% Water Depth. The Three Curves on Each Graph are the Dependency of $\eta\,(m, n)$ on Time Lag $n\Delta t$ for $m = 0$ (no lag, dash-dot), $m = 1$ (10 km lag, solid), and $m = 15$ (150 km lag, dots). Data were Obtained from the MOODS Temperature Data Base for the Years 1929 to 1991.

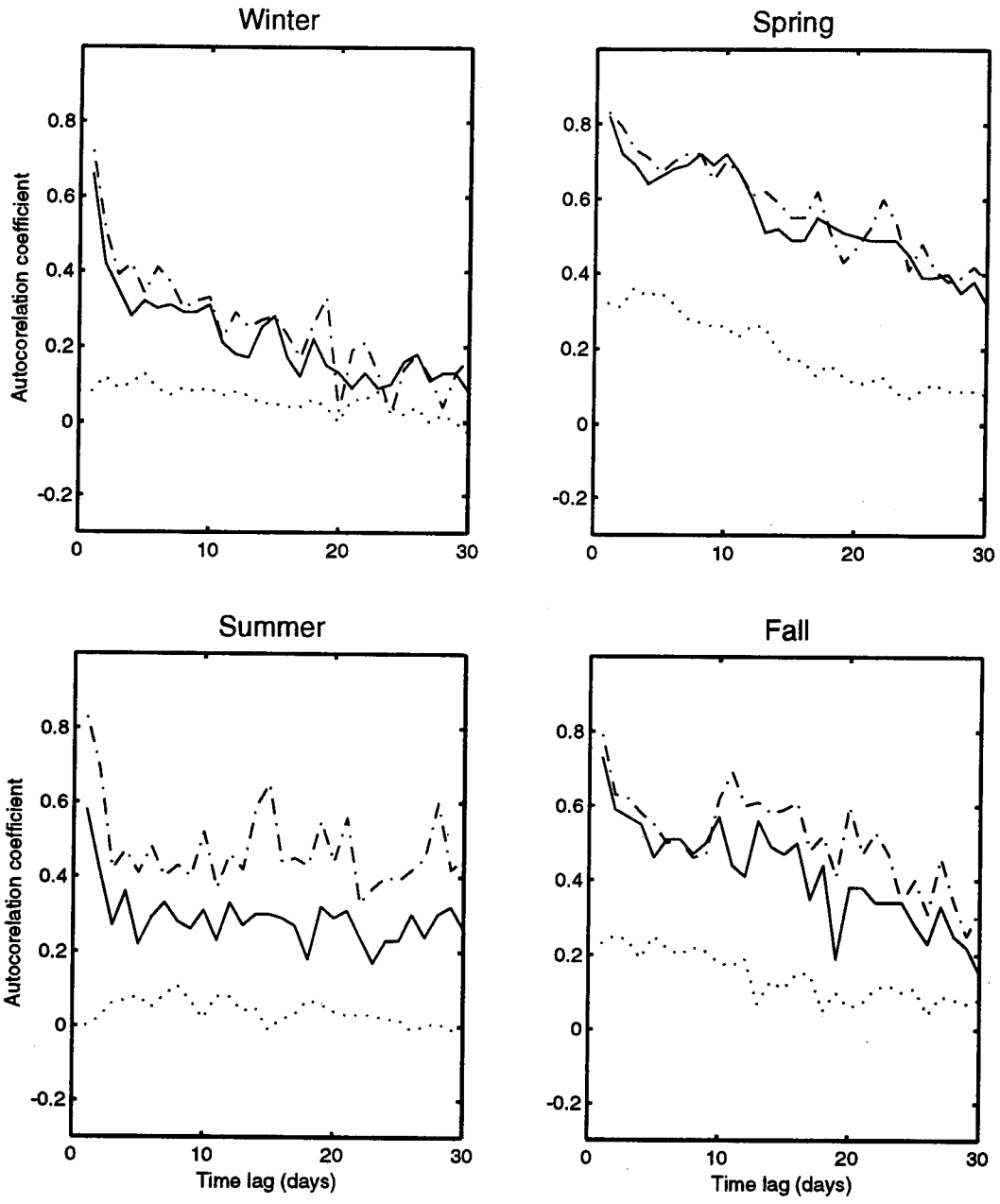

Figure D.3 Temporal Variations of Autocorrelation Function $\eta(m, n)$ for Type II Data at 80% Water Depth. The Three Curves on Each Graph are the Dependency of $\eta(m, n)$ on Time Lag $n\Delta t$ for $m = 0$ (no lag, dash-dot), $m = 1$ (10 km lag, solid), and $m = 15$ (150 km lag, dots). Data were Obtained from the MOODS Temperature Data Base for the Years 1929 to 1991.

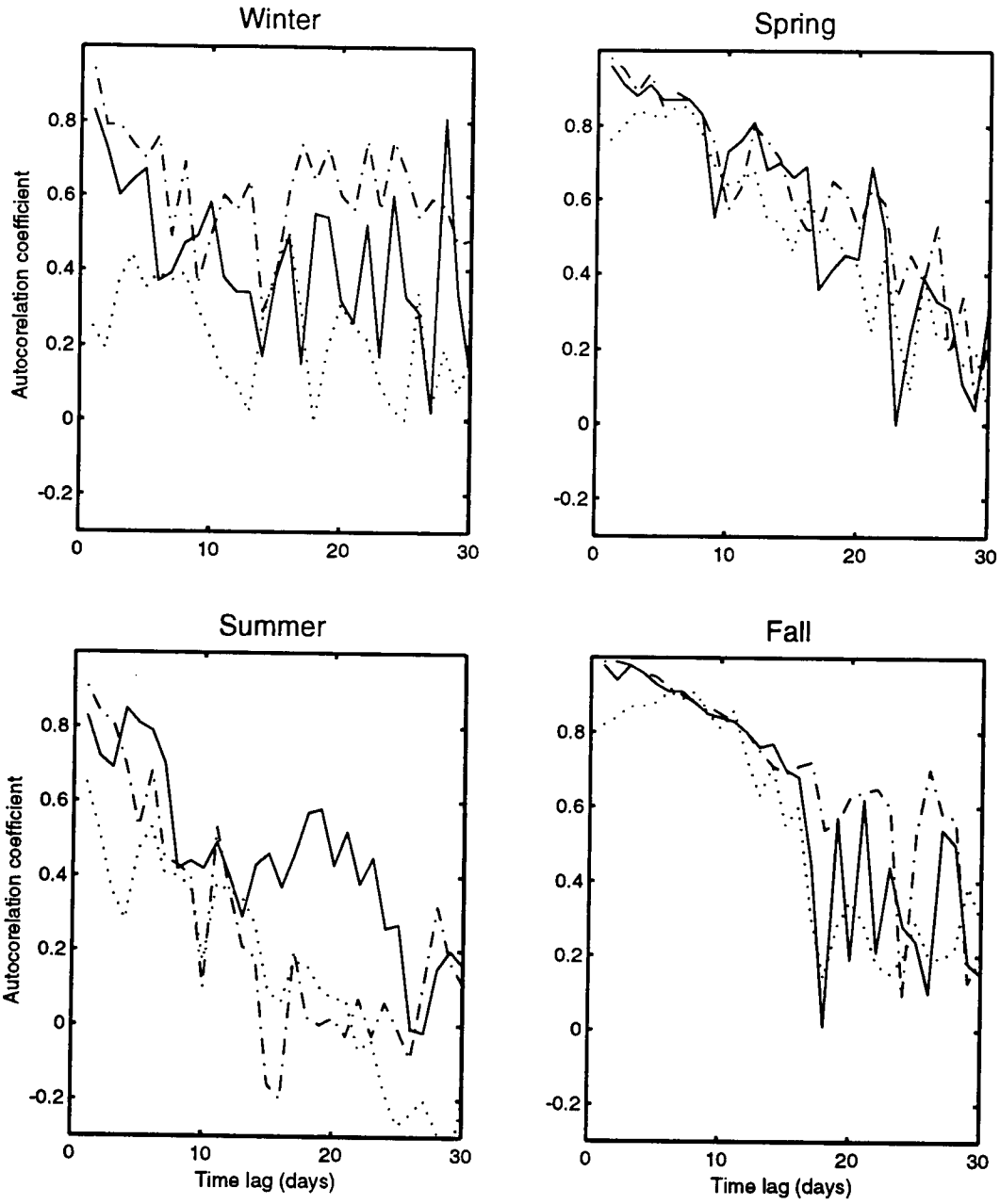

Figure D.4 Temporal Variations of Autocorrelation Function $\eta(m, n)$ for Type III Data at the Surface. The Three Curves on Each Graph are the Dependency of $\eta(m, n)$ on Time Lag $n\Delta t$ for $m = 0$ (no lag, dash-dot), $m = 1$ (10 km lag, solid), and $m = 15$ (150 km lag, dots). Data were Obtained from the MOODS Temperature Data Base for the Years 1929 to 1991.

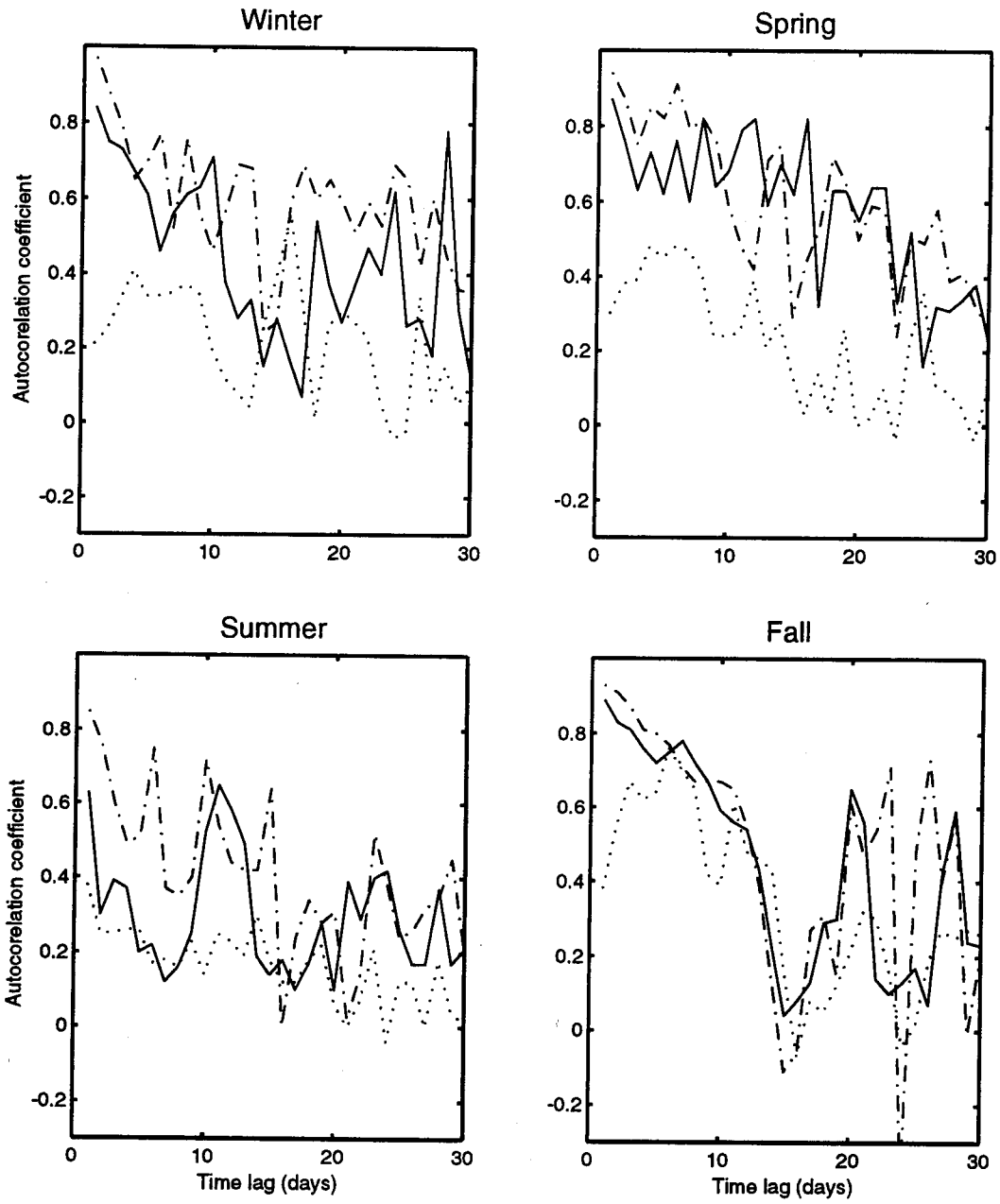

Figure D.5 Temporal Variations of Autocorrelation Function $\eta(m, n)$ for Type III Data at 50% Water Depth. The Three Curves on Each Graph are the Dependency of $\eta(m, n)$ on Time Lag $n\Delta t$ for $m = 0$ (no lag, dash-dot), $m = 1$ (10 km lag, solid), and $m = 15$ (150 km lag, dots). Data were Obtained from the MOODS Temperature Data Base for the Years 1929 to 1991.

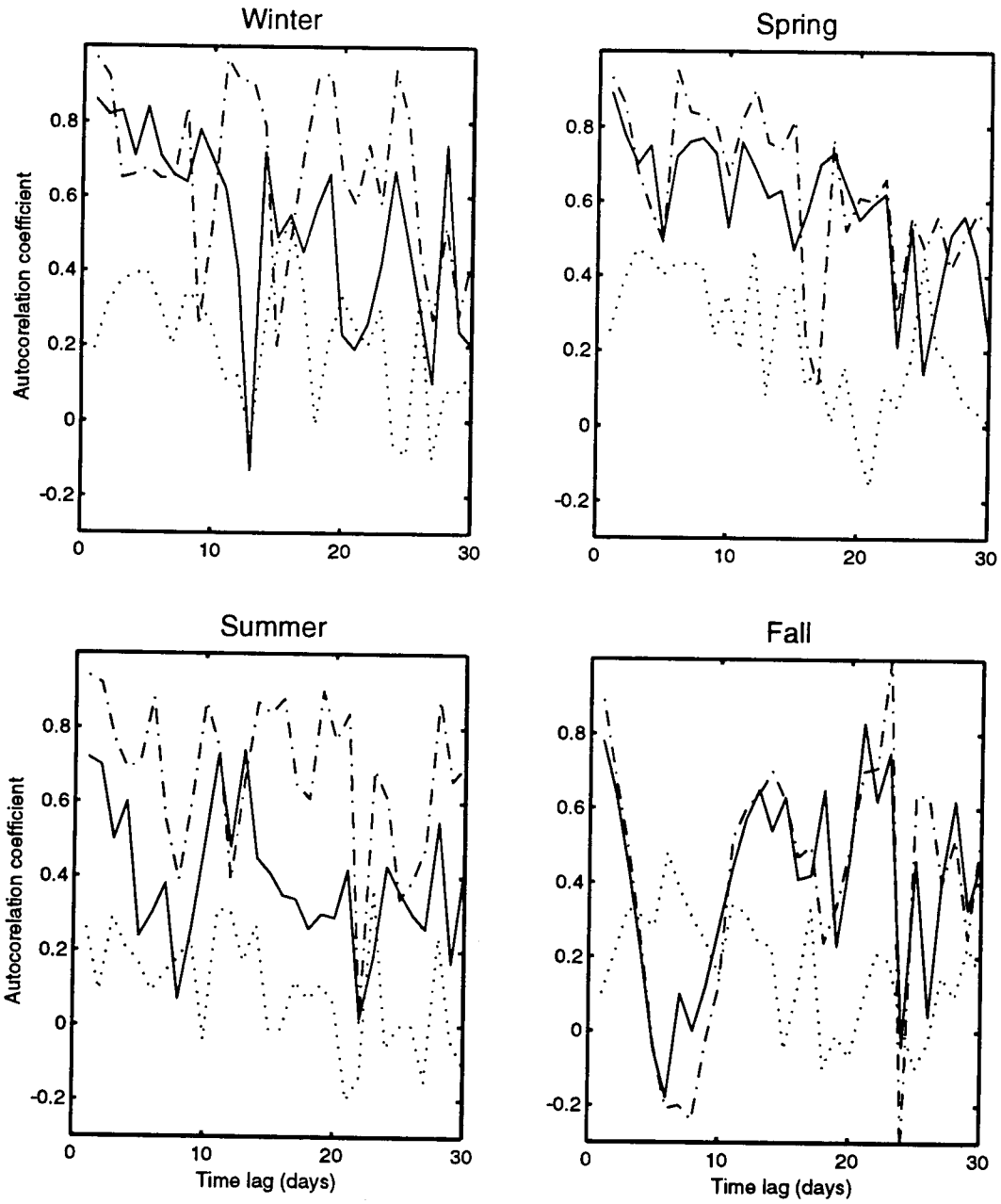

Figure D.6 Temporal Variations of Autocorrelation Function $\eta\,(m, n)$ for Type III Data at 80% Water Depth. The Three Curves on Each Graph are the Dependency of $\eta\,(m, n)$ on Time Lag $n\Delta t$ for $m = 0$ (no lag, dash-dot), $m = 1$ (10 km lag, solid), and $m = 15$ (150 km lag, dots). Data were Obtained from the MOODS Temperature Data Base for the Years 1929 to 1991.

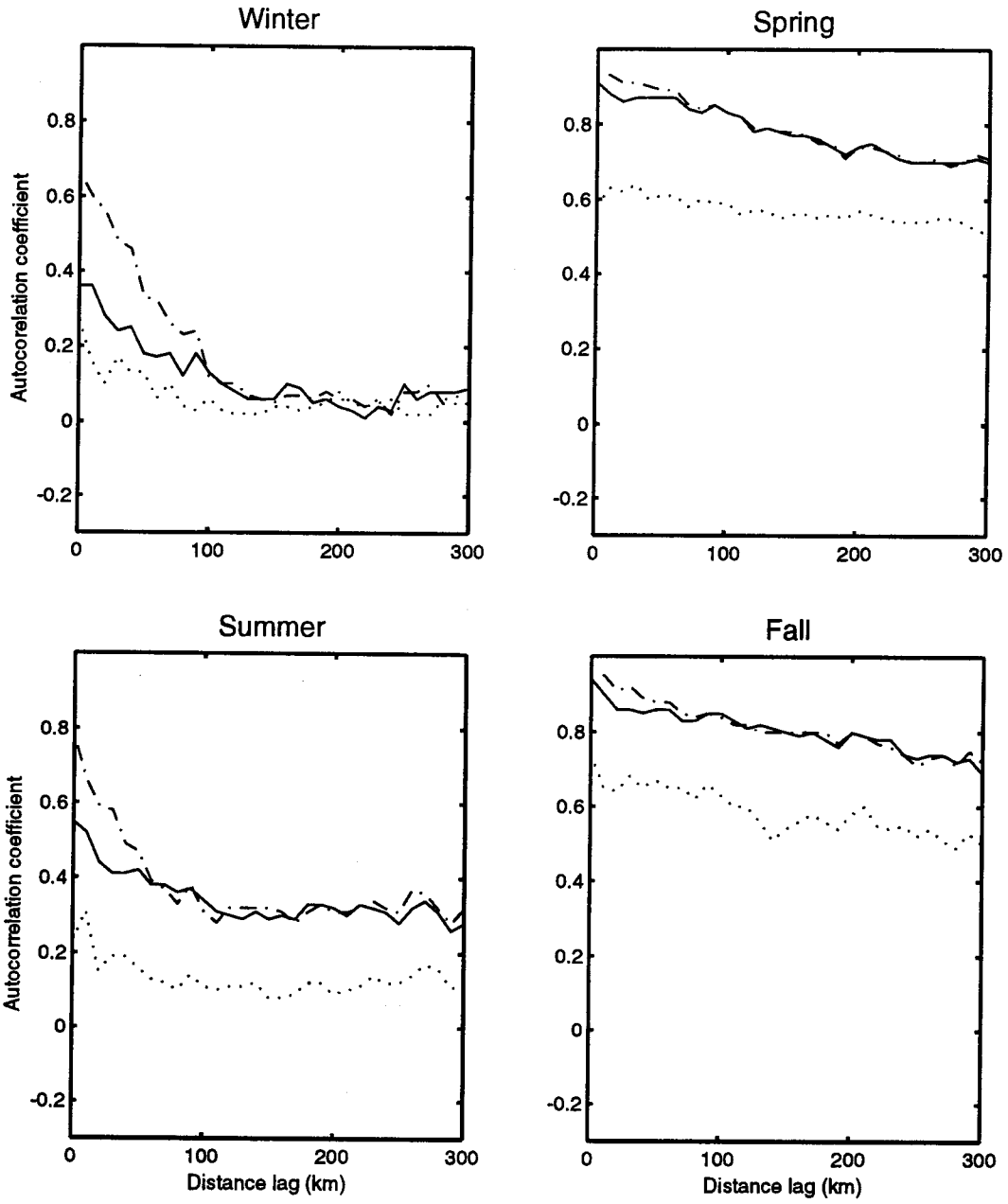

Figure D.7 Spatial Variations of Autocorrelation Function $\eta(m, n)$ for Type II at the Surface. The Three Curves on Each Graph are the Dependency of $\eta(m, n)$ on Spatial Lag $(m\Delta\gamma)$ for $n = 0$ (no temporal lag, dash-dot), $n = 1$ (1 day lag, solid), and $n = 15$ (15 day lag, dots). Data were Obtained from the MOODS Temperature Data Base for the Years 1929 to 1991.

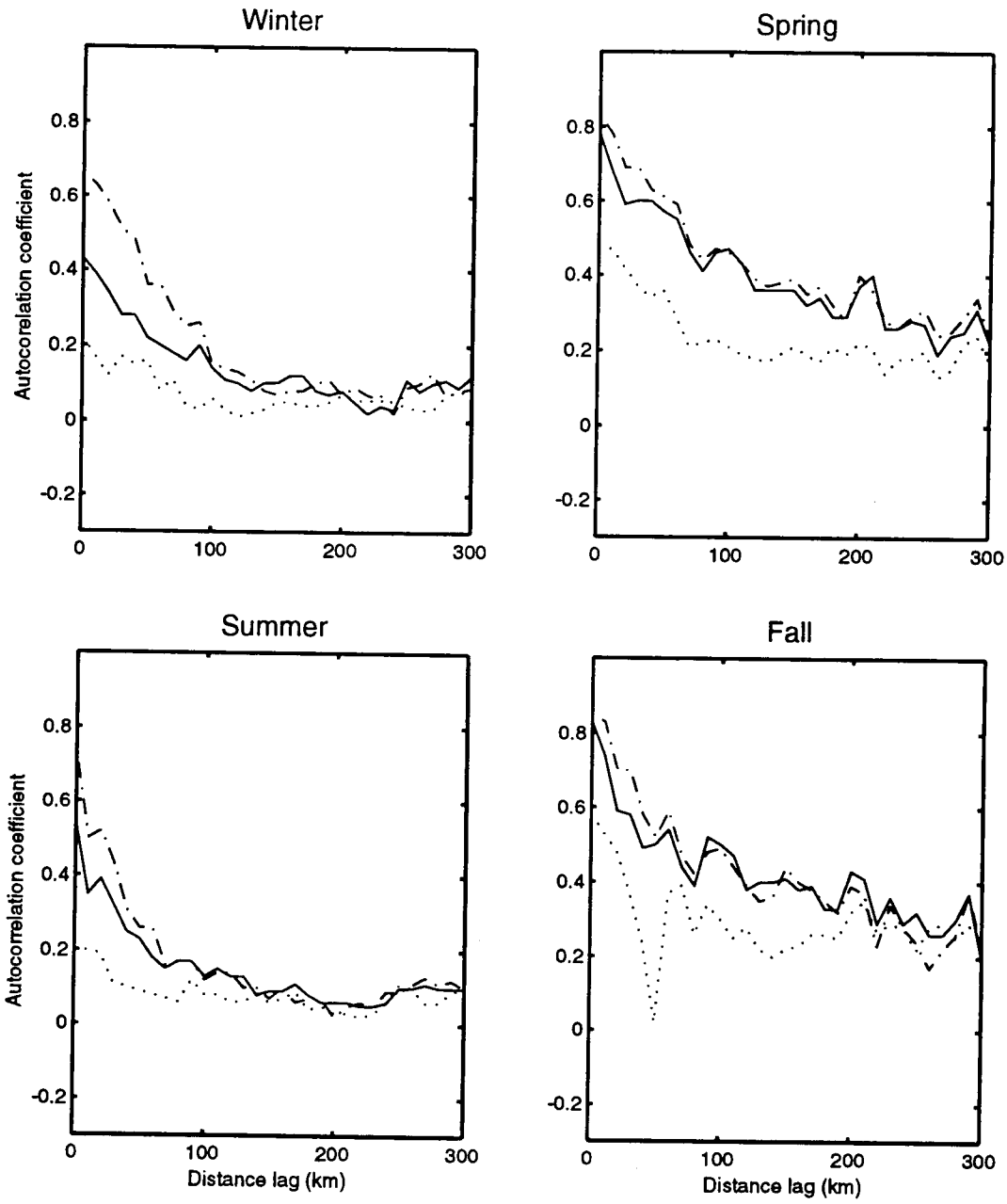

Figure D.8 Spatial Variations of Autocorrelation Function $\eta\,(m, n)$ for Type II at 50% Water Depth. The Three Curves on Each Graph are the Dependency of $\eta\,(m, n)$ on Spatial Lag $(m\Delta\gamma)$ for $n = 0$ (no temporal lag, dash-dot), $n = 1$ (1 day lag, solid), and $n = 15$ (15 day lag, dots). Data were Obtained from the MOODS Temperature Data Base for the Years 1929 to 1991.

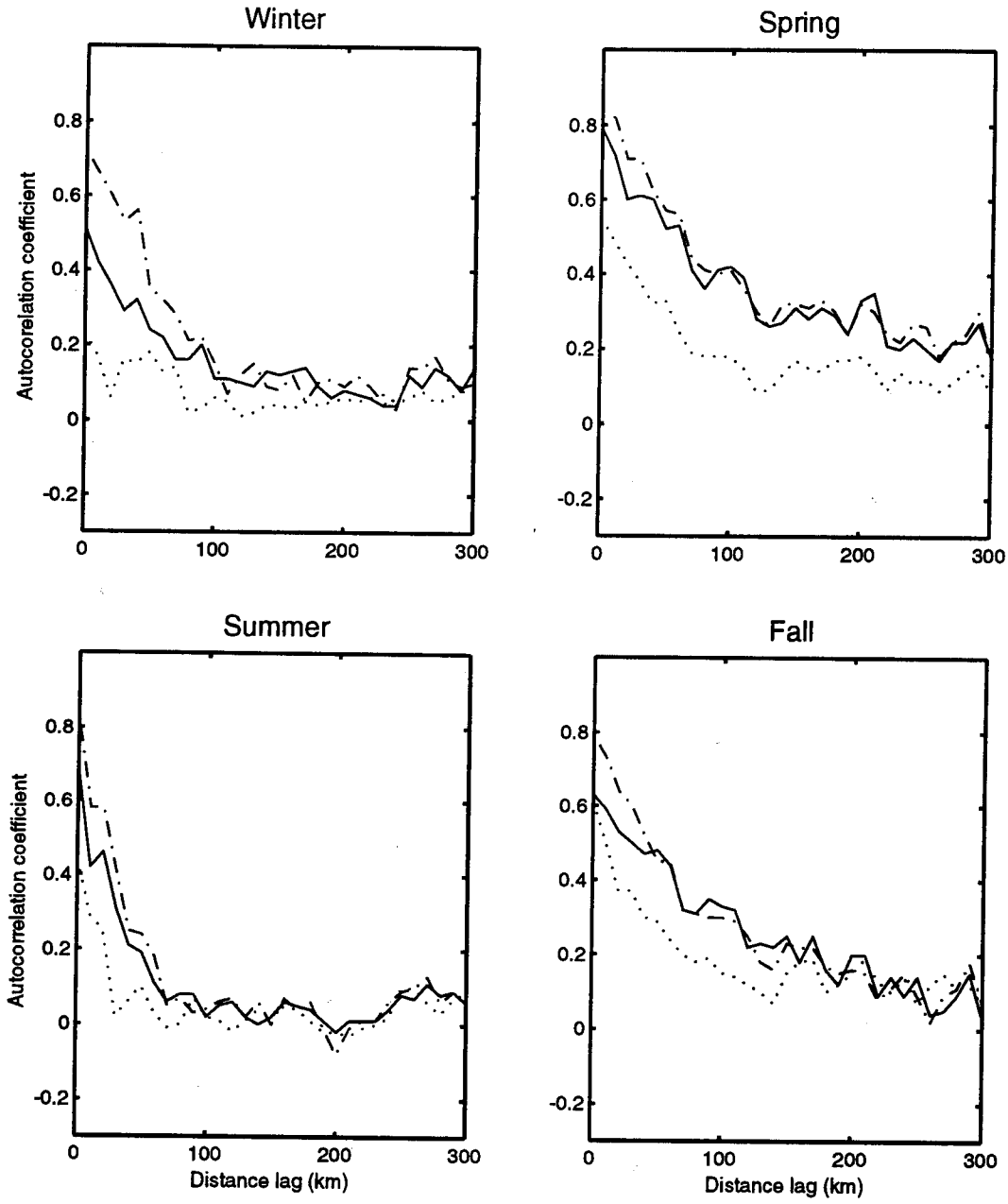

Figure D.9 Spatial Variations of Autocorrelation Function $\eta\,(m, n)$ for Type II at 80% Water Depth. The Three Curves on Each Graph are the Dependency of $\eta\,(m, n)$ on Spatial Lag $(m\Delta\gamma)$ for $n = 0$ (no temporal lag, dash-dot), $n = 1$ (1 day lag, solid), and $n = 15$ (15 day lag, dots). Data were Obtained from the MOODS Temperature Data Base for the Years 1929 to 1991.

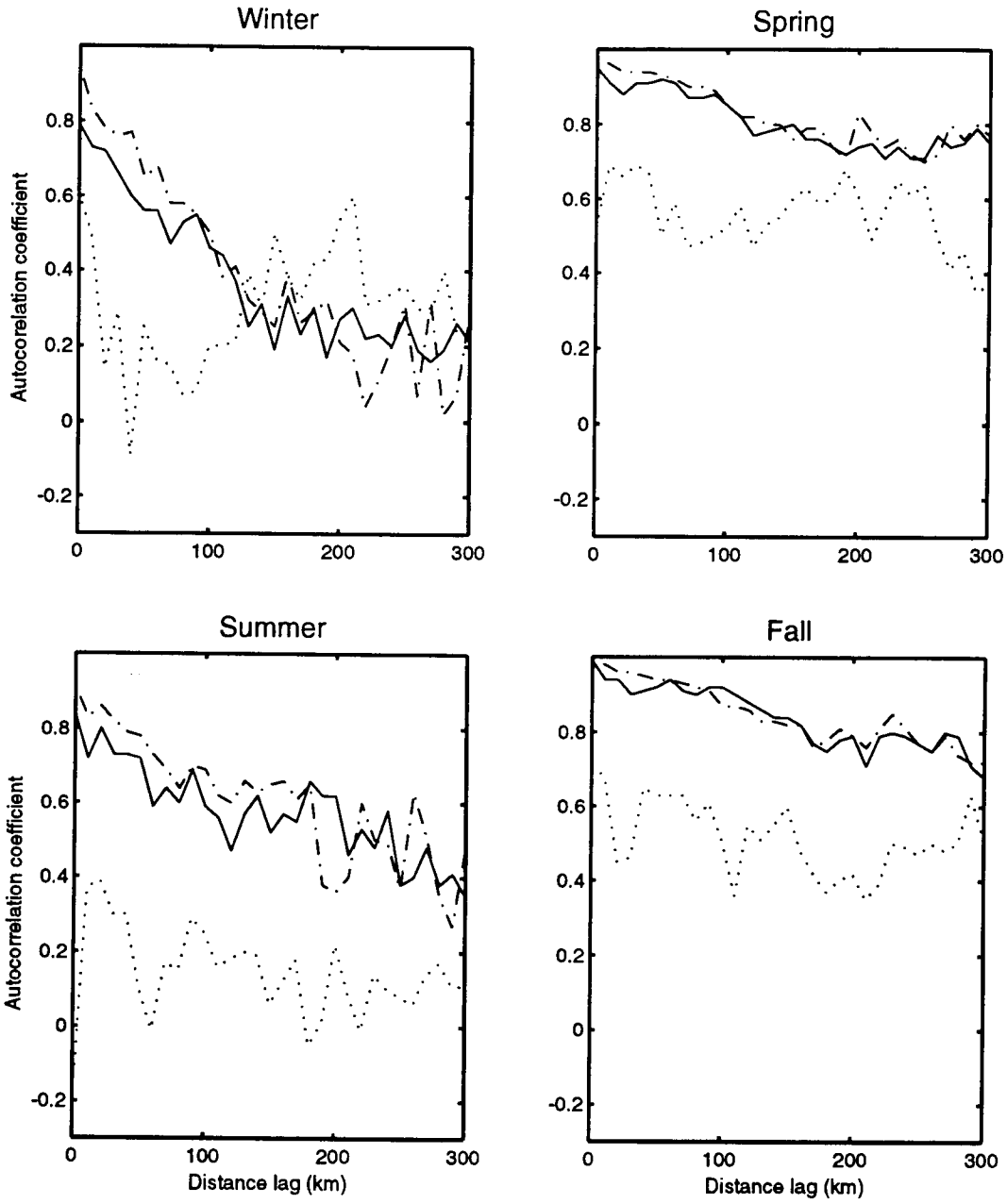

Figure D.10 Spatial Variations of Autocorrelation Function $\eta\,(m, n)$ for Type III at the Surface. The Three Curves on Each Graph are the Dependency of $\eta\,(m, n)$ on Spatial Lag $(m\Delta\gamma)$ for $n = 0$ (no temporal lag, dash-dot), $n = 1$ (1 day lag, solid), and $n = 15$ (15 day lag, dots). Data were Obtained from the MOODS Temperature Data Base for the Years 1929 to 1991.

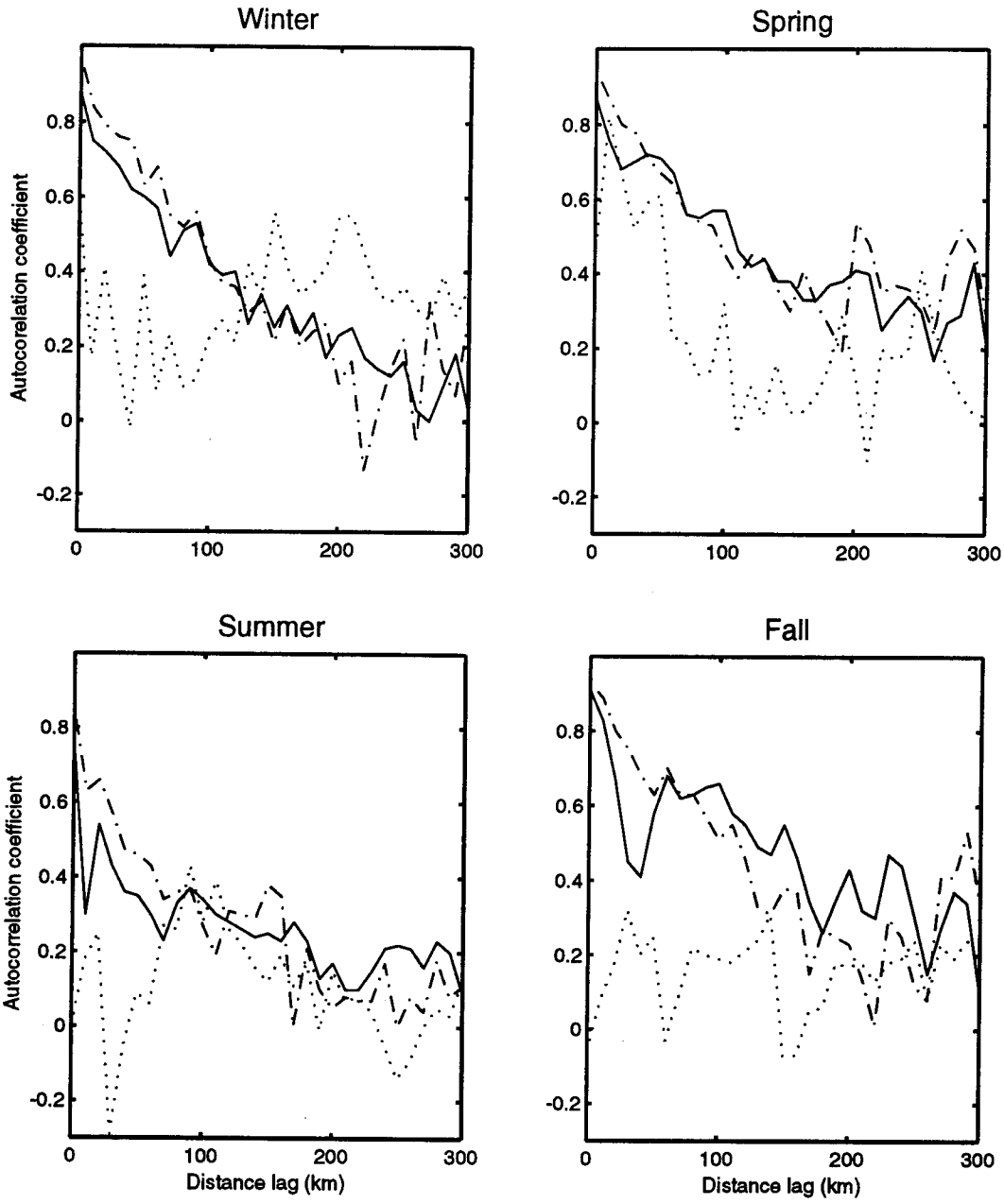

Figure D.11 Spatial Variations of Autocorrelation Function $\eta(m, n)$ for Type III at 50% Water Depth. The Three Curves on Each Graph are the Dependency of $\eta(m, n)$ on Spatial Lag $(m\Delta\gamma)$ for $n = 0$ (no temporal lag, dash-dot), $n = 1$ (1 day lag, solid), and $n = 15$ (15 day lag, dots). Data were Obtained from the MOODS Temperature Data Base for the Years 1929 to 1991.

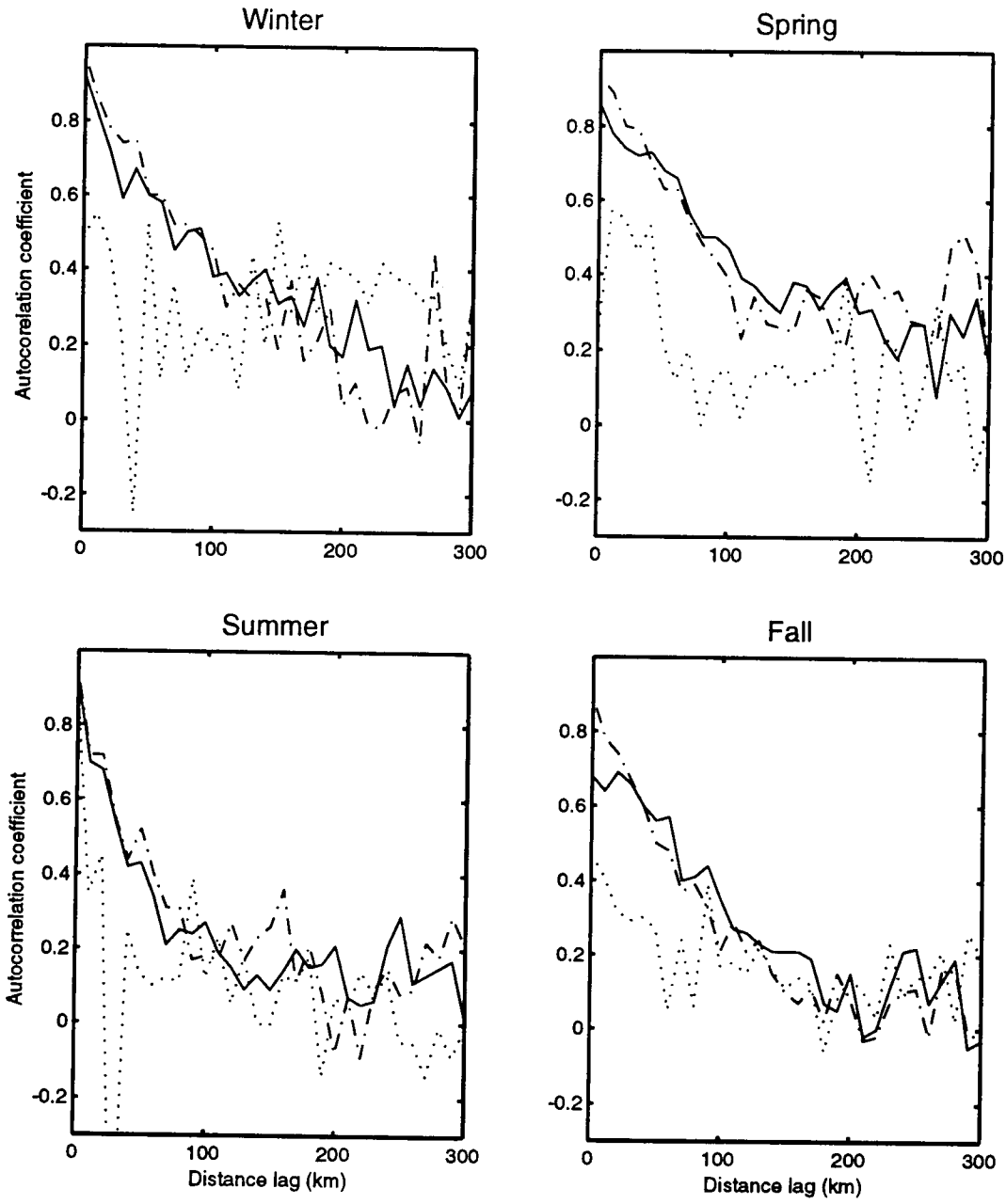

Figure D.12 Spatial Variations of Autocorrelation Function $\eta\,(m, n)$ for Type III at 80% Water Depth. The Three Curves on Each Graph are the Dependency of $\eta\,(m, n)$ on Spatial Lag $(m\Delta\gamma)$ for $n = 0$ (no temporal lag, dash-dot), $n = 1$ (1 day lag, solid), and $n = 15$ (15 day lag, dots). Data were Obtained from the MOODS Temperature Data Base for the Years 1929 to 1991.

INITIAL DISTRIBUTION LIST

1.	Defense Technical Information Center Camerson Station Alexandria, Virginia 22304-6145	2
2.	Library, Code 52 Naval Postgraduate School Monterey, California 93943-5002	2
3.	Department of Meteorology Code MR/HY Naval Postgraduate School 589 Dyer Rd. Rm 252 Monterey, California 93943	1
4.	Department of Oceanography Code OC/BF Naval Postgraduate School 833 Dyer Rd. Rm 331 Monterey, California 93943	1
5.	Superintendent Attn: Professor Peter C. Chu Naval Postgraduate School Monterey, California 93943-5000	3
6.	Lieutenant Susan K. Wells 1524 Yonkee Ave Sheridan, Wyoming 82801	2
7.	Superintendent Naval Research Laboratory 7 Grace Hopper Avenue Stop 2 Monterey, California 93943-5502	1
8.	Chairman Oceanography Department U.S. Naval Academy Annapolis, Maryland 21402	1

9. Office of Naval Research (Code 420) — 1
800 N. Quincy Street
Arlington, Virginia 22217

10. Library
Scripps Institution of Oceanography — 1
P.O. Box 2367
La Jolla, California 92037

11. Dr. Mike Carron — 1
Naval Oceanographic Office, Code N3T
Stennis Space Center, Mississippi 39522

12. Steven D. Haeger — 2
Naval Oceanographic Office, Code N3T
Stennis Space Center, Mississippi 39522

13. NOAA Library — 1
7600 Sand Point Way NE
Building 3
Seattle, Washington 98115

14. CDR David Martin — 1
Naval Oceanographic Office, Code N22
Stennis Space Center, Mississippi 39522